DEPARTAMENTO DE ASTROFÍSICA

Universidad de La Laguna

# *Shedding light on the darkest galaxies: Structure and substructures in Sextans and other Milky Way dwarf spheroidals*

Memoria que presenta
D. Luis Cicuéndez Salazar
para optar al grado de
Doctor por la Universidad de La Laguna

Directora: Dra. Giuseppina Battaglia
Tutora: Dra. Carme Gallart


INSTITUTO Đ ASTROFISICA Đ CANARIAS
septiembre de 2018

Examination date: October, 2018
Thesis supervisor: Dr. Giuseppina Battaglia
Thesis tutor: Dr. Carme Gallart


Part of the material included in this document has already been published in *Astronomy & Astrophysics* and *Monthly Notices of the Royal Astronomical Society*

*A mi familia,*
*a mi alcachofa*
*y a todos los que me han aguantado*

**Acknowledgements**

First of all, I would like to acknowledge the Instituto de Astrofísica de Canarias for its Resident Astrophysicist PhD program and Fundación la Caixa for the financial support.

I would like to thank my supervisor, Giuseppina Battaglia, for the opportunity she gave me to get into the field of Dwarf Galaxies. Without her, this thesis would have not been possible. Likewise I would like to thank Carme Gallart for being my thesis tutor. I also thank all the current and past members of the Local Group Group, for the relaxed weekly meetings and their useful discussions: Matteo, Chris, Arianna, Tomás, Antonio, Salvatore, Mike, Lara, Clara, Tobias and Ricardo. I am also grateful to P.A. Palicio for correcting the proper motion of Ursa Minor for the solar reflex motion (Chapter 4).

I acknowledge hospitality at the Institute of Astronomy, University of Cambridge, during part of my work and financial support by the University of la Laguna thanks to its international mention grant. I also acknowledge the financial support of G. Battaglia by the Spanish Ministry of Economy and Competitiveness (MINECO) under the Ramón y Cajal Programme (RYC-2012-11537) and the grant AYA2014-56795-P.

Based on observations at Cerro Tololo Inter-American Observatory, National Optical Astronomy Observatory (NOAO Prop. ID: 2015A/1013; PI: B. McMonigal), which is operated by the Association of Universities for Research in Astronomy (AURA) under a cooperative agreement with the National Science Foundation.

Based on observations obtained with MegaPrime/MegaCam, a joint project of CFHT and CEA/DAPNIA, at the Canada-France-Hawaii Telescope (CFHT) which is operated by the National Research Council (NRC) of Canada, the Institut National des Science de l'Univers of the Centre National de la Recherche Scientifique (CNRS) of France, and the University of Hawaii.

This project used data obtained with the Dark Energy Camera (DECam), which was constructed by the Dark Energy Survey (DES) collaboration. Funding for the DES Projects has been provided by the U.S. Department of Energy, the U.S. National Science Foundation, the Ministry of Science and Education of Spain, the Science and Technology Facilities Council of the United Kingdom, the Higher Education Funding Council for England, the National Center for Supercomputing Applications at the University of Illinois at Urbana-Champaign, the Kavli Institute of Cosmological Physics at the University of Chicago, the Center for Cosmology and Astro-Particle Physics at the Ohio State University, the Mitchell Institute for Fundamental Physics and Astronomy at Texas A&M University, Financiadora de Estudos e Projetos, Fundação Carlos Chagas Filho

de Amparo à Pesquisa do Estado do Rio de Janeiro, Conselho Nacional de Desenvolvimento Científico e Tecnológico and the Ministério da Ciência, Tecnologia e Inovacão, the Deutsche Forschungsgemeinschaft, and the Collaborating Institutions in the Dark Energy Survey. The Collaborating Institutions are Argonne National Laboratory, the University of California at Santa Cruz, the University of Cambridge, Centro de Investigaciones Enérgeticas, Medioambientales y Tecnológicas-Madrid, the University of Chicago, University College London, the DES-Brazil Consortium, the University of Edinburgh, the Eidgenössische Technische Hochschule (ETH) Zürich, Fermi National Accelerator Laboratory, the University of Illinois at Urbana-Champaign, the Institut de Ciències de l'Espai (IEEC/CSIC), the Institut de Física d'Altes Energies, Lawrence Berkeley National Laboratory, the Ludwig-Maximilians Universität München and the associated Excellence Cluster Universe, the University of Michigan, the National Optical Astronomy Observatory, the University of Nottingham, the Ohio State University, the University of Pennsylvania, the University of Portsmouth, SLAC National Accelerator Laboratory, Stanford University, the University of Sussex, and Texas A&M University.

This work has made use of the IAC-STAR Synthetic CMD computation code. IAC-STAR is suported and maintained by the computer division of the Instituto de Astrofísica de Canarias.

Luis Cicuéndez

**Summary**

This thesis is focused on studying the structure and substructures in dwarf spheroidal galaxies (dSphs) satellites of the Milky Way (MW), mainly on the spatial distribution, but also on the internal kinematic and metallicity properties of their stellar component, from the analysis of large samples of individual stars. Due to the proximity of these small galaxies to a much larger system such as the MW, we also searched for possible tidal tails caused by their mutual interaction, which was one of the main objectives of this thesis; the presence of tidal tails would indicate departure from dynamical equilibrium, invalidating one of the main assumptions on which determinations of the dark matter content and distribution of these galaxies rely on. The dSphs studied in this thesis are Sextans, Ursa Minor (UMi) and the recently discovered Eridanus II (Eri II).

Sextans was chosen because of its very low central surface brightness and much larger extent compared to other similarly luminous MW dSphs, which make it a good candidate for being tidally disturbed by the MW, but at the same time hard to study in detail, due to the difficulties of mapping the large angular extent of its stellar body and of separating its stars from the very numerous contaminants (e.g. foreground MW stars). Its study was the most extensive one. As such, it was split in two parts. In the first part we obtained in visitor mode (PI: B. McMonigal; Observer: L. Cicuéndez; 6 nights) very spatially extended CTIO/DECam $g$ and $r$ deep photometry (covering $\sim 20$ deg$^2$ and reaching out to $\sim 2$ magnitudes below the oldest main-sequence turn-off) of the galaxy and explored its structural properties, searching for possible tidal tails/debris as well. We obtained the structural parameters of both the overall stellar population and its different evolutionary phases by making use of a Bayesian Markov chain Monte Carlo (MCMC) method. By making some improvements to a literature matched filter analysis of the colour-magnitude diagram, we also decontaminated their corresponding surface density maps and looked for possible departures from axisymmetry. The outcome was that Sextans is significantly more concentrated and less extended than previous studies suggested, with no signs of tidal disturbance found down to a surface brightness of $\sim 31.8$ mag/arcsec$^2$ in V-band. In agreement with previous findings, the old and metal poor stellar components such as the Blue Horizontal Branch stars were found to be considerably more extended than the rest of evolutionary phases, while bright Blue Stragglers (BSs) are more concentrated than faint ones. Nonetheless, this different spatial distributions between bright and faint BSs is compatible with the general age and metallicity gradients found in the overall stellar population of the galaxy, and therefore BSs could have

formed just by evolution of binaries and not necessarily by the disruption of a globular cluster, as suggested in the literature. In addition, we updated the membership probabilities of two literature spectroscopic catalogues by making use of an improved form of a literature "expectation maximization" technique, making them publicly available together with the photometric catalogue of point-sources used in the rest of the study.

The second part of the study dealt with the subsequent discovery of clear observational signs of past accretion/merger events in Sextans. Using the same photometric catalogue and the high probable spectroscopic members from the first part of the study, we found that the spatial distribution of stars varies as a function of the colour/metallicity: while the blue (metal-poor) red giant branch and main-sequence turn-off stars have a rather round and regular distribution, the spatial distribution of the red ones (metal-rich) is much more elliptical and irregularly shaped, with the presence of a distinct 'shell-like" overdensity in the northeast side. We also detected a "ring-like" feature on the line-of-sight (LOS) velocities, also visible when using indicators sensitive to the metallicity, which displays a considerably larger systemic velocity and lower mean metallicity than the rest of stars. All these features make Sextans, with a stellar mass of just $\sim 5 \times 10^5 M_{\odot}$, the smallest galaxy with clear observational signs of accretion to date. This fact is particularly important as it lowers the faint end of the galaxy mass function at which some predictions of the hierarchical theory of galaxy formation have been qualitatively verified.

For the study of UMi we used archive CFHT/MegaCam $g$ and $r$ photometry instead, which were also recently published and analyzed in Muñoz et al. (2018). This photometric dataset is the most deep and spatially extended one available for this system so far (covering $\sim 4$ deg$^2$ and reaching out to $\sim 2.5$ magnitudes below the oldest main-sequence turn-off). UMi is another very interesting target because it has a much higher ellipticity than most of the other dSphs, lacks a radial metallicity gradient and, in addition, there have been reports of extra-tidal stars that suggest the possible presence of tidal tails, which would indicate departure from tidal equilibrium. Hence, we performed for UMi a similar analysis as in the first part of the study of Sextans. Besides, as in the case of Sextans, UMi is hard to study in detail, due to the difficulties of mapping its large angular extent and of separating its stars from the numerous contaminants (e.g. foreground MW stars). Thus, by taking advantage of the tools developed during the study of Sextans, we obtained the structural parameters of the overall stellar population of UMi and statistically decontaminated its surface density map through two different methods, searching for deviations from axisymmetry as well. In this way the obtained structural parameters were in overall agreement with previous determinations from the

literature, and apart from a foreground stellar cluster already discovered in this same dataset, we also detected other internal substructures. One of these was a previously reported cold secondary peak in the stellar density that could result from a disrupted stellar cluster as based on numerical simulations, as in principle the rest of stellar over-dense clumps here detected that make the inner regions of UMi highly structured; this might complicate the analysis of the internal properties of this galaxy. We further detect one stellar overdensity close to the galactic centre that could also result from a central black hole whose possible presence was often investigated in the literature, with reported detections in both X-rays and radio. Regarding signs of tidal disturbances, they were not found down to a surface brightness limit of $\sim 32$ mag/arcsec$^2$ in V-band. Finally, we also calculated the membership probabilities of a literature spectroscopic catalogue and analyzed the metallicity and LOS velocity distributions of the probable UMi's members, not finding any radial gradient either on the individual metallicities or in the velocity dispersion.

Finally, we studied the case of Eri II and its candidate star cluster recently reported in the literature, because the existence of such cluster would have important implications: it would favour a cored dark matter halo for the galaxy over a cusped one, it would constrain the existence of massive compact halo objects with masses larger than $\sim 5M_{\odot}$, it would extend the empirical relationship between the number of hosted clusters and the mass of the host galaxy about two orders of magnitude below the previous limit in galactic stellar mass, and it would imply that some MW star clusters could be hosted in undetected halos with extremely faint stellar counterparts. We studied this system by making use of Magellan Clay/MegaCam and very deep ACS/WFC photometry, in order to better characterize the structural parameters of the putative cluster. By fitting its structural parameters with the MCMC method used for UMi and Sextans, they turned out to be all compatible with the ones of Eri II, which led to the hypothesis that this feature could be just the central cusp of the galactic surface density profile. Besides, the available observational evidence and a fitted ellipticity of $\epsilon = 0.4$, which would make this cluster the most elliptical one known to date with all the rest having $\epsilon < 0.3$, suggest it would be a very unusual star cluster in case it would not be just the central cusp of the stellar density profile of Eri II.

The work carried out during this thesis contributed to the following publications:

- Tracing the stellar component of low surface brightness Milky Way dwarf galaxies to their outskirts I: Sextans
  L. Cicuéndez, et al. 2018, A&A, 609, A53
- Appearances can be deceiving: clear signs of accretion in the seemingly ordinary Sextans dSph
  L. Cicuéndez and G. Battaglia, 2018, MNRAS, 480, 251
- On the early evolution of Local Group dwarf galaxy types: star formation and supernova feedback
  J.R. Bermejo-Climent, G. Battaglia, C. Gallart, A. Di Cintio, C.B. Brook, L. Cicuéndez, et al. 2018, MNRAS, 479, 1514
- The extended star formation history of Eridanus II
  (incl. L. Cicuéndez) 2018, in prep.
- 280 one-opposition near-Earth asteroids recovered by the EURONEAR with the Isaac Newton Telescope
  O. Vaduvescu, et al. (incl. L. Cicuéndez for being observer) 2018, A&A, 609, A105
- Probing the low surface brightness outskirts of Milky Way dSphs: Sextans
  L. Cicuéndez, et al. 2016, Proceedings IAU Symposium, 321, 45

## Resumen

Esta tesis se ha enfocado en estudiar la estructura y subestructuras de una muestra de galaxias enanas esferoidales (dSph) satélites de la Vía Láctea (MW), principalmente en la distribución espacial, pero también en las propiedades cinemáticas y de metalicidad de su componente estelar, mediante el análisis de grandes muestras de estrellas individuales. Debido a la proximidad de estas pequeñas galaxias a un sistema mucho mayor tal como la MW, también hemos buscado posibles colas de marea causadas por su interación con ésta, lo cual era uno de los principales objetivos de la tesis; la presencia de estas colas de marea indicaría ausencia de equilibrio dinámico, lo que invalidaría una de las principales premisas en las que se basan las determinaciones del contenido y distribución de materia oscura en estas galaxias. Las dSphs estudiadas en esta tesis son Sextans, Ursa Minor (UMi) y la recién descubierta Eridanus II (Eri II).

Sextans fue elegida por su bajo brillo superficial central y mayor extensión respecto a otras dSphs de la MW de luminosidad similar, que le convierten en un buen candidato para estar perturbado marealmente por la MW, pero al mismo tiempo difícil de estudiar en detalle debido a las dificultades de mapear la gran extensión angular de su componente estelar y de separar sus estrellas de los numerosos contaminantes presentes, tales como las estrellas de la MW en su línea de visión. El estudio de esta dSph fue el más extenso. Como tal, se dividió en dos partes. En la primera obtuvimos en modo visitante (PI: B. McMonigal; Observador: L. Cicuéndez; 6 noches) fotometría espacialmente extensa y profunda en $g$ y $r$ con CTIO/DECam (cubriendo $\sim 20$ grad$^2$ y llegando hasta $\sim 2$ magnitudes por debajo del giro de la secuencia principal más viejo) y exploramos sus propiedades estructurales, buscando además posibles colas de marea. Obtuvimos los parámetros estructurales tanto de la población estelar global como de sus distintas fases evolutivas mediante un método Bayesiano de Monte Carlo de cadenas de Markov (MCMC). Además, mejorando un análisis de filtro adaptado del diagrama color-magnitud de la literatura descontaminamos sus mapas de densidad superficial y buscamos posibles desviaciones de axisimetría. El resultado fue que Sextans resultó estar significativamente más concentrada y menos extendida de lo que sugerían estudios previos, sin presencia de perturbaciones de marea hasta un brillo superficial de $\sim 31.8$ mag/arcseg$^2$ en banda V. De acuerdo con hallazgos anteriores, las componentes estelares viejas y pobres en metales tales como las estrellas de la rama horizontal azul resultaron estar considerablemente más extendidas que el resto de fases evolutivas, mientras que las estrellas rezagadas azules (BSs) más brillantes están más concentradas que las más débiles. No obstante, demostramos que estas diferentes distribuciones espaciales entre las BSs brillantes y débiles son compatibles con el gradiente

de edad y metalicidad general encontrado en la población estelar global de la galaxia, y por tanto las BSs podrían haberse formado solamente por evolución de estrellas binarias y no necesariamente por la destrucción de un cúmulo globular, como sugería la literatura. Además, mejorando un algoritmo ya publicado de "maximización de la expectativa", actualizamos las probabilidades de pertenencia de dos catálogos espectroscópicos de la literatura, publicándolas junto con el catálogo fotométrico usado en el resto de nuestro estudio.

La segunda parte del estudio se encargó del posterior descubrimiento de claros signos observacionales de pasados eventos de acreción en Sextans. Usando el mismo catálogo fotométrico y los miembros espectroscópicos más probables de la primera parte del estudio, encontramos que la distribución espacial de las estrellas varía en función de su color/metalicidad: mientras que la partes azules de la rama de gigantes rojas y del giro de la rama principal tienen una distribución bastante circular y regular, las rojas tienen una distribución mucho más elíptica e irregular, con la presencia de una sobredensidad en el lado noreste. Asimismo detectamos una subestructura con forma de anillo en las velocidades a lo largo de la línea de visión (LOS), también visible mediante el uso indicadores sensibles a la metalicidad, que presenta una velocidad sistémica considerablemente mayor y una metalicidad media menor que el resto de las estrellas. Todas estas peculiaridades hacen de Sextans, con una masa estelar de tan sólo $\sim 5 \times 10^5 M_{\odot}$, la galaxia más pequeña con claros signos observacionales de acreción descubierta hasta la fecha. Este hecho es especialmente importante ya que disminuye el límite inferior de la función de masa de las galaxias en el que se han comprobado cualitativamente algunas predicciones del modelo jerárquico de formación de galaxias.

Para el estudio de UMi usamos fotometría de archivo en $g$ y $r$ obtenida con CFHT/MegaCam, que también fue publicada y analizada recientemente en Muñoz et al. (2018). Este catálogo fotométrico es el más profundo y extenso de este sistema disponible hasta la fecha (cubriendo $\sim 4$ grad$^2$ y llegando hasta $\sim 2.5$ magnitudes por debajo del giro de la rama principal más viejo). UMi es otro sistema muy interesante ya que tiene una elipticidad mucho mayor que la mayoría de dSphs, no tiene gradiente radial de metalicidad y, además, existen varios reportes de estrellas más allá del radio de marea que indicarían ausencia de equilibrio dinámico. Por tanto, realizamos para UMi un análisis similar al de la primera parte del estudio de Sextans. Además, al igual que Sextans, UMi es difícil de estudiar en detalle por las dificultades en mapear su gran extensión angular y separar sus estrellas de los numerosos contaminantes, tales como las estrellas de la MW en su línea de visión. De este modo, aprovechando las herramientas desarrolladas durante el estudio de Sextans, obtuvimos los parámetros estructurales de la población estelar global de UMi y descontam-

inamos su mapa de densidad superficial mediante dos métodos estadísticos diferentes, buscando desviaciones de axisimetría. De esta forma los parámetros estructurales que obtuvimos están de acuerdo con determinaciones previas de la literatura, y aparte de un cúmulo globular situado delante de la galaxia que ya fue descubierto con anterioridad en este mismo catálogo, también detectamos otras subestructuras internas. Una de éstas es un frío pico secundario en la densidad estelar que ya fue reportado en la literatura y que, en base a simulaciones numéricas, podría resultar de la destrucción de un cúmulo estelar, como en principio el resto de sobredensidades estelares aquí detectadas que dan lugar a unas regiones internas de UMi altamente estructuradas; esto podría complicar el análisis de las propiedades internas de esta galaxia. También detectamos una sobredensidad estelar cercana al centro galáctico que podría resultar de un agujero negro central cuya posible presencia fue estudiada con frecuencia en el pasado, con detecciones reportadas tanto en radio como en rayos X. Respecto a las perturbaciones de marea, éstas no se encontraron hasta un brillo superficial de $\sim 32$ mag/arcseg$^2$ en banda V. Por último, también calculamos las probabilidades de pertenencia de un catálogo espectroscópico de la literatura y analizamos las distribuciones de metalicidad y velocidad LOS de los miembros más probables de UMi, sin encontrar ningún gradiente radial ni en las metalicidades individuales ni en la dipersión de velocidades.

Finalmente estudiamos el caso de Eri II y de su candidato a cúmulo estelar, recientemente reportado en la literatura, por las importantes implicaciones que tendría la existencia de tal cúmulo: favorecería un halo de materia oscura con núcleo para la galaxia frente a uno de pico central, restringiría la existencia de objetos de halo masivos y compactos de masas superiores a $\sim 5M_{\odot}$, extendería la relación empírica entre el número de cúmulos húespedes y la masa de la galaxia anfitriona cerca de dos órdenes de magnitud por debajo del anterior límite en masa estelar galáctica, e implicaría que algunos cúmulos estelares de la MW estuvieran alojados en halos indetectables con contrapartidas estelares extremadamente débiles. Nosotros estudiamos este sistema a través de fotometría obtenida con Magellan Clay/MegaCam, y muy profunda con ACS/WFC, para caracterizar mejor los parámetros estructurales del posible cúmulo. Ajustando sus parámetros estructurales con el método MCMC usado con UMi y Sextans, resultaron ser todos compatibles con los de Eri II, lo que dio lugar a la hipótesis de que esta sobredensidad podría ser simplemente en el pico central del perfil de densidad superficial galáctico. Además, la evidencia observacional disponible y una elipticidad ajustada de $\epsilon = 0.4$ que convertiría a este cúmulo en el más elíptico descubierto hasta la fecha, con todos los demás teniendo $\epsilon < 0.3$, sugieren que éste sería un cúmulo estelar muy inusual en caso de que no se tratase simplemente del pico central del perfil de densidad estelar de Eri II.

El trabajo llevado a cabo durante esta tesis contribuyó a las siguientes publicaciones:

- Tracing the stellar component of low surface brightness Milky Way dwarf galaxies to their outskirts I: Sextans
  L. Cicuéndez, et al. 2018, A&A, 609, A53
- Appearances can be deceiving: clear signs of accretion in the seemingly ordinary Sextans dSph
  L. Cicuéndez y G. Battaglia, 2018, MNRAS, 480, 251
- On the early evolution of Local Group dwarf galaxy types: star formation and supernova feedback
  J.R. Bermejo-Climent, G. Battaglia, C. Gallart, A. Di Cintio, C.B. Brook, L. Cicuéndez, et al. 2018, MNRAS, 479, 1514
- The extended star formation history of Eridanus II
  (incl. L. Cicuéndez) 2018, en prep.
- 280 one-opposition near-Earth asteroids recovered by the EURONEAR with the Isaac Newton Telescope
  O. Vaduvescu, et al. (incl. L. Cicuéndez por ser observador) 2018, A&A, 609, A105
- Probing the low surface brightness outskirts of Milky Way dSphs: Sextans
  L. Cicuéndez, et al. 2016, Proceedings IAU Symposium, 321, 45

# Contents

# 1

# Introduction

## 1.1 Dwarf Galaxies

THE classical definition of a *dwarf galaxy* is a galaxy fainter than $M_V \simeq -17$ but more spatially extended than globular clusters (GCs) (Tammann 1994, see Fig. 1.1), as they partly overlap in terms of luminosity.

While the internal dynamics of GCs are well described by Einstein's general theory of relativity only accounting for their observed baryonic matter, under this theory an unknown form of unobservable matter is needed to explain the internal kinematic properties of dwarf galaxies. Thus, unlike GCs, dwarf galaxies are believed to contain this so-called dark matter (DM), but they also present extended chemical enrichment and star formation histories. These two latter characteristics are interpreted as being due to their deeper gravitational potential well resulting from their larger dynamical mass, which allows them to retain the gas expelled through supernova explosions and stellar winds. In fact, dwarf galaxies can even host GCs (see e.g. the case of Fornax, hosting five GCs; Hodge 1961, and the possible cases of Ursa Minor and Eridanus II discussed in Chapters 4 and 5, respectively).

Assuming that in the early universe small systems were the first ones to collapse (White & Rees 1978), it was galaxies like these that formed first and, thus, would host the first stars. Besides, their extended distribution all over the early Universe also makes them good candidates to uniformly reionize it (Stark et al. 2007; Choudhury et al. 2008), although this is still highly debated. They are very low-metallicity systems which follow the well-known luminosity-metallicity relation, whereby the brighter a galaxy is, the more metal-rich it is (Fig. 1.2).

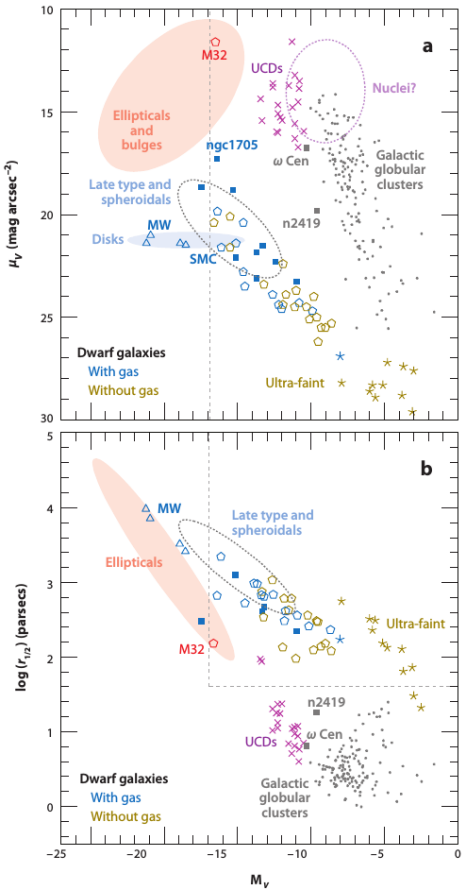


Figure 1.1: Relationships between the structural parameters for different types of stellar systems. Dotted lines show the classical limits of the dwarf galaxies as defined by Tammann (1994). Top: Central surface brightness $\mu_V$ versus absolute magnitude in V-band $M_V$. Bottom: Half-light radius $r_{1/2}$ versus $M_V$. Coloured ellipses show the typical regions of the different types of stellar systems. Blue compact dwarfs are plotted with blue solid squares. Local Group dwarf galaxies are marked as open pentagons, blue for those with gas and yellow for those without gas. The ultrafaint dwarfs follow the same colour code but with star symbols instead. Figure taken from Tolstoy et al. (2009).

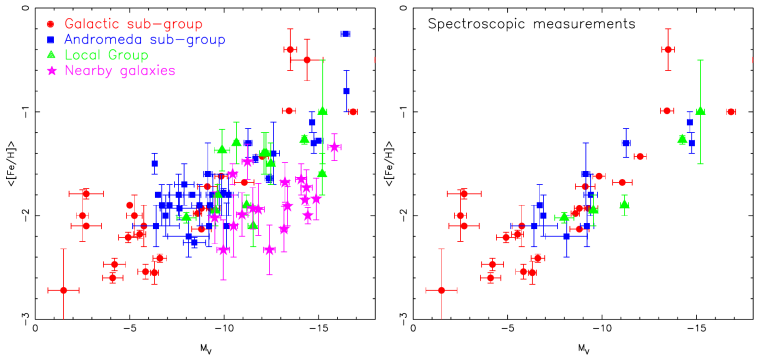


Figure 1.2: Mean stellar metallicity vs. absolute magnitude in V-band for Galactic, M31, Local Group and nearby dwarf galaxies. Left: All measurements regardless of the techniques used to derive the metallicity. Right: Measurements derived from stellar spectroscopy. Figure taken from McConnachie (2012).

As the hierarchical theory of galaxy formation predicts that small systems continuously merge to form larger ones, the characteristics of the smaller systems are also expected to be somehow reflected in the larger ones. Two particular cases would be the Milky Way (MW) and Andromeda (M31) with their respective satellite dwarf galaxies. In this way, the analysis of the structural properties and chemical compositions of the different stellar populations of these dwarfs provide clues about the formation of the larger galaxies M31 and MW, as well as about the stellar formation in the early ages of the universe. Indeed, tidal streams from existing and destroyed satellite galaxies have already been discovered in the inner halo of M31, including the Giant Stellar Stream (Ferguson & Mackey 2016), and around MW's halo, such as the tidal stream from the Sagittarius dwarf (see e.g. Ibata et al. 1994, 2001; Newby et al. 2013 and references therein) and many more.

## 1.2 Types of Dwarf Galaxies in the Local Group

The MW belongs to the Local Group (LG). This galaxy group comprises about one hundred galaxies, most of them dwarfs. Its largest galaxies are Andromeda (M31), the MW, M32 and the Triangulum Galaxy (M33). Due to their proximity, we can study the dwarf galaxies of the LG star by star (i.e. their stellar populations are resolved) in great detail, which makes them the best studied

dwarf galaxies (see e.g. the review from Tolstoy et al. 2009 or their observed properties summarized in McConnachie 2012).

Dwarf galaxies of the LG are classically divided in spheroidals (dSph), irregulars (dIrr) and transition types (dT). dSphs are the most common dwarf galaxies in the LG, have no gas and therefore no ongoing star formation; thereby they are also known as early-type galaxies and their internal kinematic properties can only be derived from their stars. They are typically located within $\sim 300$ kpc of large galaxies like the MW or M31 (Fig. 1.3). The ultrafaint dwarf galaxies (uFds) seem to be the natural extension of dSphs down to much lower luminosities ($M_V \gtrsim -8$) and metallicities ([Fe/H] $\lesssim -2$), following smooth scaling relationships like the ones plotted in Fig. 1.1, and thus the distinct terms dSph and uFd are meaningless except for historical reasons and sequence of discovery (the first uFds were discovered in 2005). Nonetheless, it is also important to note that the fainter uFds fall in the same region where both the extensions of dSphs and GCs seem to be. dIrrs, however, have gas and are usually located in the field of the LG. They are also known as late-types as they are typically transforming their gas into stars at the present day as they have been probably doing during their entire lifetime with variable star formation rates. With regard to the dTs, they have intermediate properties between dSphs and dIrrs.

The existence of this latter type suggests the idea of an evolutionary path from dIrrs to dSphs by loosing their gas and therefore stopping their star formation, especially when getting close to a large galaxy such as the MW. This could explain the fact that dSphs are typically close to large galaxies like our own or M31, while dIrrs are usually located in the field (Fig. 1.3). This observation is fundamental for dSph formation models, which are usually based on their proximity to large galaxies to protect them from accretion of external material that could otherwise start new episodes of star formation. In addition to cutting off the accretion of external material, tidal interactions with the larger galaxy can sculpt dIrrs into dSphs, as the models developed by Mayer et al. (2007) showed. Their simulations show how ram pressure and tidal shocks remove all the gas of dIrrs and transport outward the initial angular momentum of their stars, transforming these rotationally supported systems into pressure supported ones with quite flat stellar velocity dispersion profiles typical of dSphs. Further, no exclusively young dwarf galaxy of any type has been found yet, always hosting stars at the oldest look-back times observed (Tolstoy et al. 2009). Nonetheless, there are still some remaining issues about the relationships between the different types of dwarf galaxies.

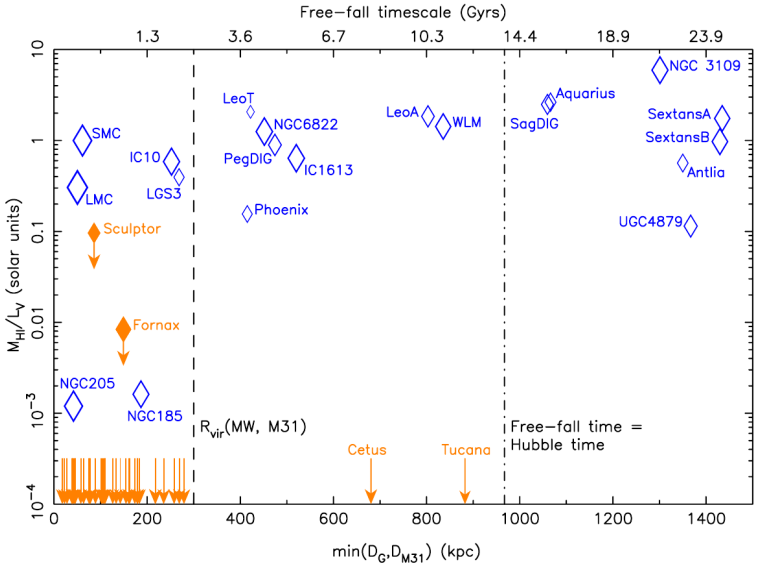


Figure 1.3: HI fraction of dwarf galaxies in and around the LG, as a function of their distance to the MW or M31. Blue diamonds correspond to dwarfs with confirmed HI content, while orange arrows mark the distances of gas-deficient dwarfs to the MW or M31. The orange diamonds for Fornax and Sculptor indicate that the presence of HI in this dwarfs is ambiguous. The size of the diamonds is proportional to the absolute visual magnitude of the galaxy. On the top axis it is indicated the time that a dwarf would require to accelerate from rest and reach the closest giant galaxy. The vertical dashed line corresponds to the approximate virial radius of the MW/M31, while the dot-dashed line marks the distance at which this time equals a Hubble time. Figure taken from McConnachie (2012).

## 1.3 Dwarf Spheroidal Galaxies (dSphs)

In this thesis we focus on the dSphs. These are the most DM dominated galaxies we know of (for recent reviews see Battaglia et al. 2013 and Walker 2013), and as such they are the focus of a large body of works to investigate the nature of DM. The estimated dynamical mass and mass-to-light ratio within the half-light radius of most dSphs in and around the LG are shown in Fig. 1.4. They are inferred within the half-light radius because a wide range of DM models estimate approximately the same enclosed mass within their half-light radius (Walker et al. 2010), showing that this quantity is well constrained by the available data.

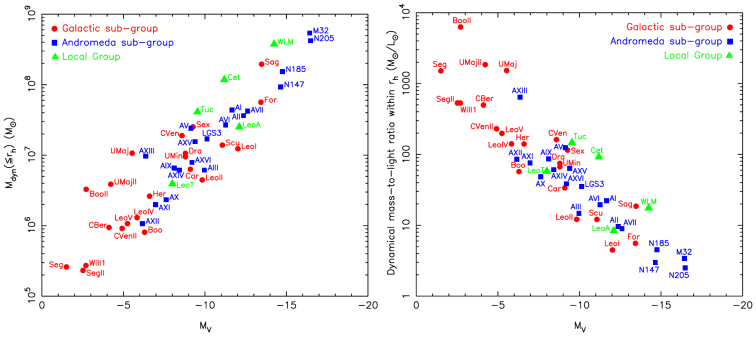


Figure 1.4: Left: Estimated dynamical mass enclosed by the half-light radius as a function of absolute magnitude in V-band, for Galactic, M31 and LG dwarfs for which half-light radius and stellar velocity dispersion are available. They were derived with the relation from Walker et al. (2009c). Right: Mass-to-light ratio within their half-light radius vs. absolute magnitude in V-band. Panels taken from McConnachie (2012).

This figure shows a clear correlation of the luminosity of dSphs with both their dynamical mass and mass-to-light ratio, implying that despite fainter dSphs have less DM content, the fainter a dSph is, the larger dynamical mass-to-light ratio it has. For them, being non-rotating spheroidal systems, devoid of neutral gas, their DM content and distribution is derived from the study of the velocity dispersion of their individual stars along the line-of-sight (LOS) to the observer, as noted in Fig. 1.4. This is because the amplitude of the velocity dispersion in a pressure supported dSph depends largely on its gravitational potential, and thus we can estimate its mass distribution applying for example the Jeans formalism (Binney & Tremaine 2008) to its LOS velocity dispersion profile. One applies it to the LOS velocities of its individual stars because, on the one hand, by definition DM is not observable, and on the other, because with the current instrumentation at such distances we can only get accurate stellar velocities along the LOS, not in the other two orthogonal axes. Nonetheless, if the velocity dispersion is different when measured along different axes, the system is said to be anisotropic (otherwise it would be called isotropic), and for such a system the real shape of its velocity dispersion profile can be dramatically different from the one inferred from just its LOS velocities, as it would occur with the derived DM profile too. Fortunately, from now on the relatively accurate proper motions provided by the Gaia space mission will help us to estimate the DM content

and distribution adding the information from the stellar kinematics in the other two orthogonal axes. A clear example in this direction is the work from Massari et al. (2018), in which they determine for the first time the anisotropy in an external galaxy, the Sculptor dSph, by measuring its radial and tangential velocity dispersions. Additionally, one should also account for the fact that, as the dynamical mass can only be estimated within the region spectroscopically sampled (Binney & Tremaine 2008), the most spatially extended sample is preferable. Lastly, although it has been proposed that the velocity dispersions derived could be inflated by the presence of binary stars, different studies that made use of observations over multiple epochs found that their effect is minimal for systems such as the bright dSphs (e.g. Olszewski et al. 1995).

On the other hand, for some faint dSphs their large DM content is better evidenced by their metallicity dispersions instead of the velocity ones. They generally have values large enough ($\sigma_{[Fe/H]} \gtrsim 0.4$ dex, Geha et al. 2009; Norris et al. 2010; Willman et al. 2011) to imply extended and even multiple star formation episodes, which are possible thanks to the deep gravitational potential wells resulting from their large dynamical masses that allow to retain the gas expelled through stellar winds and supernova explosions.

Even though they have small physical sizes, the proximity of many dSphs to the MW results in large angular extents, of approximately a few degrees. Hence the study of these systems has particularly flourished since the advent of wide-area imagers and multi-object spectrographs on 4m-10m telescopes, which allow to determine the properties of their resolved stellar component in great detail out to their very low surface brightness outskirts. This applies in particular to the 'brightest' of the MW dSphs[1], those with luminosities $-15 \lesssim M_V \lesssim -8$, for which one can gather wide-area photometric datasets with large number statistics reaching well below the oldest main-sequence turn-off and spectroscopic datasets providing velocities and metallicities of several hundreds stars per galaxy.

## 1.4 Structure and substructures in dSphs

The stellar structure of a dSph is supposed to carry information about its formation history and evolution. While the de Vaucouleurs (de Vaucouleurs 1948) and Hubble (Hubble 1930) models cannot reproduce their observed surface density profiles, Sérsic (Eq. 1.1), exponential (Eq. 1.2), King (Eq. 1.3) and Plummer (Eq. 1.4) models do provide good fits to the data. As such, these are

[1]For convenience, we will also refer to them as to the 'classical dSphs', i.e. those known before SDSS (Carina, Fornax, Draco, Leo I, Leo II, Ursa Minor, Sculptor, Sextans).

the models that we will use to fit the observed surface number density profiles of the dSphs studied in this thesis.

The Sérsic model (Sersic 1968) was originally introduced as a generalization of the de Vaucouleurs model in the form:

$$f_S = Ke^{b\left(\left(-\frac{R}{r_e}\right)^{\left(\frac{1}{n}\right)}-1\right)}, \tag{1.1}$$

where $K$ is a scaling parameter, $R$ is the radius from the galactic centre, $r_e$ the effective radius, $n$ is a positive real number and $b$ a dimensionless constant. In general, bright ellipticals are found to be well fitted by this model when $n \sim 4$ (de Vaucouleurs law), bulges and intermediate luminosity ellipticals with $1 \lesssim n \lesssim 4$, and galaxy disks and dwarf ellipticals when $n \sim 1$, which corresponds to the exponential function. Indeed, Faber & Lin (1983) used the exponential function to model the surface density profiles of dSphs:

$$f_e = Ke^{-\frac{R}{r_e}}, \tag{1.2}$$

where in this case $K$ is the central density. Although this model has less parameters than the Sérsic model, it still provides a good fit. Read & Gilmore (2005) later proved that exponential profiles are a generic phase which results when dSphs experience rapid mass loss at early times.

The empirical form of the King model (King 1962) is given by

$$f_K = K\left(\frac{1}{\sqrt{1+\left(\frac{R}{r_c}\right)^2}} - \frac{1}{\sqrt{1+\left(\frac{r_t}{r_c}\right)^2}}\right)^2, \tag{1.3}$$

where $r_c$ is the core radius, at which the King model drops to $\sim$ half its central value, and $r_t$ is the tidal radius, at which it reaches a null density. As these intuitive structural parameters have been frequently fitted to dwarf galaxies (e.g. Hodge 1966; Irwin & Hatzidimitriou 1995), we adopt the King profile as one of the models to compare with the observed surface density profiles of the dSphs studied in this thesis, although we note that there is not necessarily a physical reason to assume that this model is a realistic form of the stellar density profile of dSphs, and interpretations based on this assumption should be carefully treated. For example, the presence of stars beyond the King tidal radius does not necessarily imply that they are being tidally stripped from the galaxy itself. We also note that for the concentration parameters in this thesis ($c = log_{10}(r_t/r_c) < 1$), this profile is quite similar to the physically motivated

form for GCs later presented in King (1966), based on a lowered Gaussian distribution function.

Lastly, the functional form of the Plummer model (Plummer 1911) is

$$f_P = \frac{K}{\left(1 + \left(\frac{R}{r_p}\right)^2\right)^2} , \tag{1.4}$$

where in this case $K$ is also the central density and $r_p$ is the Plummer half-light radius. This model is commonly used in N-body simulations of dwarfs disruption embedded in tidal fields (e.g. Law et al. 2005). As such, we will also use this profile to model the observed stellar density profiles of the dSphs studied in this thesis.

It is especially important to derive the correct values of the structural parameters from these profiles due to their relevant implications. For example, as mentioned before for the half-light radius, a wide range of DM models have approximately the same value for the enclosed mass within it (Wolf et al. 2010), indicating that this quantity is well determined if the value of the half-light radius is correctly estimated. Likewise, McConnachie & Irwin (2006) suggested that the scale radii of the M31 dSphs are at least two times larger than those of MW dSphs at all luminosities. However, the considerable number of new discoveries since then allowed Brasseur et al. (2011) and later Tollerud et al. (2012) to prove that the mean relations between scale radii and luminosities of the MW and M31 dwarf populations are statistically compatible with each other. Another example of the importance of correctly determining the value of a structural parameter could be found in the ellipticity, as dSphs can exhibit projected ellipticities up to $\sim 0.8$ (McConnachie 2012), while all GCs discovered till now have $\epsilon < 0.3$ (see the most complete catalogs with ellipticities of GCs in the MW, Harris 2010; M31, Staneva et al. 1996 and LMC, Goodwin 1997). Thus, this parameter could also aid in distinguishing dSphs from GCs in uncertain cases if $\epsilon > 0.3$, as such ellipticities would be extremely unusual for a GC, while not for a dSph. As we will see, this fact will be particularly important in Chapter 5.

On the other hand, the stellar populations of several classical MW dSphs are also known to exhibit spatial variations both in their age and metallicity properties (Harbeck et al. 2001; Tolstoy et al. 2004; Battaglia et al. 2006, 2011, 2012a; Faria et al. 2007; de Boer et al. 2012, to mention only a few), which point to the central regions having experienced a more prolonged star formation and chemical enrichment history than the outer parts.

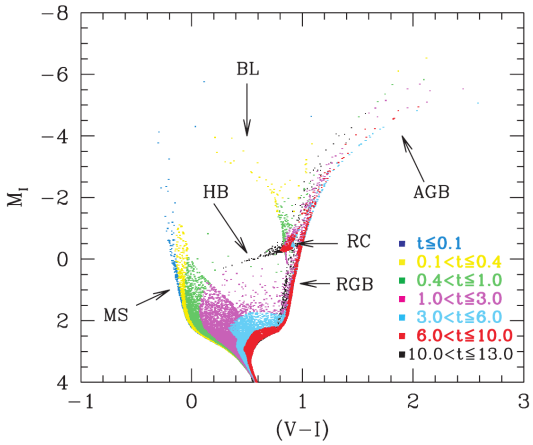


Figure 1.5: Synthetic CMD computed with a constant star formation rate from 13 Gyr ago to the present and with metallicity linearly increasing from $Z_0 = 0.0001$ to $Z_f = 0.02$. Stars are plotted with different colours according to their age. Evolutionary phases are indicated through the following labels: BL - Blue Loop; HB - Horizontal Branch; RC - Red Clump; RGB - Red Giant Branch; AGB - Asymptotic Giant Branch. Figure taken from Aparicio & Gallart (2004a).

The Colour-Magnitude Diagram (CMD) of their resolved stars (see an example in Fig. 1.5) is a useful tool to check these variations, as it can be used to select features corresponding to different evolutionary phases in which the stars have characteristic ages or metallicities, to then plot their spatial distributions. This technique was indeed frequently used in this thesis. For example, horizontal branch stars are older than $\sim$ 10 Gyr, as supported by stellar evolutionary models, and the depth of a main-sequence turn-off depends exclusively on the age of its stars (Fig. 1.5). Likewise, for a roughly uniform age, the stars in the blue portion of the red giant branch (RGB) have lower metallicities than in its red portion (Chapter 3; Rey et al. 2004). Another way to search for spatial variations in the metallicity of a dSph is to directly measure the Fe content ([Fe/H]) of its individual stars, as it is considered to be representative of the metallicity and relatively accessible due to the numerous Fe lines present in the spectra of the stars. It is usually measured for RGB stars because this is the brightest CMD feature in dSphs, thus more easy to observe when they are distant, and because it spans almost the whole age range of the galaxy (from its oldest ages until 1 Gyr ago). Further, in RGB stars [Fe/H] can be estimated

from the equivalent width of the IR CaII Triplet (CaT) lines even from low and intermediate resolution spectra ($R \sim 2000$) (Rutledge et al. 1997; Pont et al. 2004; Battaglia et al. 2008b; Carrera et al. 2013). In this way, much less observing time is required as CaT lines are much stronger than Fe ones. In Chapter 4 for example, we use the CaT equivalent widths to derive the [Fe/H] of the individual stars of Ursa Minor and analyse its metallicity properties. In dSphs, these metallicity measurements often reveal a radial gradient with lower metallicities in the outskirts (see e.g. Battaglia et al. 2011).

Besides, substructures have been found in the density maps, kinematics and metallicities of some of these systems (e.g. Irwin & Hatzidimitriou 1995; Bellazzini et al. 2002; Palma et al. 2003; Wilkinson et al. 2004; Tolstoy et al. 2004; Battaglia et al. 2006; Walker et al. 2006), possibly due to the disruption of stellar clusters or even smaller accreted dwarf galaxies, where this informs us on stellar cluster formation in small systems and accretion/merging between low mass haloes (Pace et al. 2014, see also Amorisco et al. 2014 for the M31 satellite And II). In this thesis we will deal with several of these substructures in dSphs hitherto unknown and resulting from past accretion/merger events. Indeed, similar observed events have already been modeled with dedicated simulations (Ebrová & Łokas 2015; Fouquet et al. 2017), taking into account the wealth of observational information available for the affected dSphs. But these substructures are also important for other reasons. For example, some substructures detected in the spatial distributions of dSphs due to hosted stellar clusters or their disrupted remnants would have been easily dissolved in less time than their measured ages if the DM halo of their host galaxy was cuspy, while they could survive within a cored one (see e.g. the cases of UMi; Kleyna et al. 2003; Lora et al. 2012, Eri II; Contenta et al. 2018, and And XXV; Amorisco 2017). Thus, these substructures also have important implications for the ΛCDM cosmological model of structure formation, as it predicts galactic DM haloes with characteristic central cusps whose density diverges as $\rho \propto r^{-1}$ (e.g. Dubinski & Carlberg 1991; Navarro et al. 1996).

Also separate chemo-dynamical stellar components have been detected (Tolstoy et al. 2004; Battaglia et al. 2006, 2011), and their simultaneous mass modelling has been proposed as a way to relieve known degeneracies in the Jeans analysis of spherical systems (Battaglia et al. 2008a) and place further constraints on their DM density profile (e.g. Walker & Peñarrubia 2011; Amorisco & Evans 2012). The large number statistics and accurate radial velocities provided by available spectroscopic datasets of individual stars in MW dSphs has also allowed the use of sophisticated mass modelling techniques (e.g. Breddels & Helmi 2013; Zhu et al. 2016). The dynamical modelling of MW dSphs relies on the assumption that these systems are in dynamical equilibrium at all radii.

However, elongations and/or distortions in the outer parts of the stellar body have been found in a handful of MW dSphs, suggesting that the present-day properties of the stellar component of these specific galaxies might be affected by tidal forces exerted by the MW (e.g. Bellazzini et al. 2002; Battaglia et al. 2012a; McMonigal et al. 2014; Roderick et al. 2015, 2016b). Depending on the degree of tidal stripping, this might have implications for estimates of the DM halo properties (e.g. Muñoz et al. 2008). Its effect on the DM halos of satellite dSphs is to decrease the intrinsic $\sigma_v$ (Peñarrubia et al. 2008; Kazantzidis et al. 2017), although tidal tails tend to increase it in the outer regions. Strong tidal disturbances have also been shown to attenuate initial differences in the spatial and kinematic properties of stellar populations, offering a possible explanation as to why in some dSphs the presence of chemo-dynamical stellar components is not as evident as in other ones, such as in Carina (e.g. Sales et al. 2010).

In the same way, the spectroscopic samples from which we measure these LOS velocities and metallicities can also be highly contaminated by MW stars (see e.g. the cases of Sextans and Ursa Minor in this thesis). If not identified with appropriate methods, these contaminants can have a huge impact on the inferred kinematic, DM and chemical properties of MW dSphs, specially in those with low surface brightness. For example, they can increase the velocity dispersion from which to infer the DM content of the galaxy. Therefore, it is of particular interest to first realize a careful decontamination of the spectroscopic samples to be used (Walker et al. 2009b).

## 1.5 Outline of this thesis

Within the dSph satellites of the MW, in this thesis we study three of them: Sextans, Ursa Minor (UMi) and lastly, Eridanus II (Eri II) and a candidate star cluster hosted in this system. We focus on extracting as much information as possible from their resolved stellar populations by analysing the global structure and internal substructures of these dwarfs, mainly from the spatial distributions of their stars, but also from their LOS velocities and metallicity properties. Among the aims of this analysis is to better characterize the structural, chemical and kinematic parameters of these systems, explore spatial variations in age and metallicity, search for tidal interactions with the MW that could place them out of dynamical equilibrium and seek observational signs of accretion.

Sextans was originally chosen for being a good candidate to be tidally disturbed by the MW, while at the same time hard to study owing to the difficulties in mapping its large angular extent, and in separating its stars from the very numerous foreground MW contaminants due to its very low surface brightness. As we have just discussed, the possible presence of tidal tails would

indicate departure from dynamical equilibrium, which is required for the correct estimates of its dark matter halo properties. In this sense, we obtained very deep and spatially extended CTIO/DECam photometry in $g$ and $r$ bands of the galaxy. As its study was the most extensive one, it was separated in two chapters. In Chapter 2 we study the spatial structure of its overall resolved stellar population and separated in different evolutionary phases, searching for possible tidal tails/debris as well. We also update the membership probabilities of the targets from two literature spectroscopic catalogues because, as we have noted before, spectroscopic samples of low surface brightness MW dSphs such as Sextans can be highly contaminated by MW stars, and the presence of these contaminants can impact on the inferred kinematic, DM and chemical properties if not identified with appropriate methods.

In Chapter 3 we use the aforementioned photometric and spectroscopic catalogues to reveal and study clear signs of accretion in the Sextans dSph, detected both in the spatial, LOS velocity and metallicity distributions. As it is the smallest galaxy with clear observational signs of accretion up to date, this discovery is particularly important as it lowers the faint end of the galaxy mass function at which some predictions of the hierarchical theory of galaxy formation have been qualitatively verified.

Chapter 4 is dedicated to the study of UMi because in addition to also being a good candidate for being tidally disturbed by the MW, literature studies showed that its inner regions appear to be highly structured. Thus, due to its large extent and presence of numerous MW contaminants, we tried to reproduce on UMi the study performed in Chapter 2 with Sextans by applying many of the tools developed during its study to another wide-area and deep photometric dataset, this time obtained from archive CFHT/MegaCam data. On this occasion we also perform a deeper analysis of the kinematics and metallicities basing on a spectroscopic catalogue from the literature, as it was not studied in detail yet, obtaining inter alia the velocity dispersion and mean metallicity profiles.

Chapter 5 was devoted to Eri II and in particular, its recently reported candidate star cluster. We chose this system mainly because of the important implications that we have seen for this kind of substructures in the spatial distributions of dSphs, because it would be the faintest galaxy hosting a star cluster observed to date and because its characteristics would make it a very unusual star cluster. Specifically, we aimed to better characterize the structural parameters of the candidate cluster from very deep photometry of Eri II's central regions obtained with ACS/WFC, as well as to re-analyze the Magellan Clay/MegaCam data where it was discovered.

Finally, we summarize the conclusions of the work carried out during this thesis and the consequent future prospects in Chapter 6.

# 2

# Tracing the stellar component of low surface brightness Milky Way Dwarf Galaxies to their outskirts I: Sextans

**L. Cicuéndez, G. Battaglia, M. Irwin, J. R. Bermejo-Climent, B. McMonigal, N. F. Bate, G. F. Lewis, A. R. Conn, T. J. L. de Boer, C. Gallart, M. Guglielmo, R. Ibata, A. McConnachie, E. Tolstoy and N. Fernando**

Published as A&A, 2018, 609, A53

**ABSTRACT**

**Aims.** We present results from deep and very spatially extended CTIO/DECam $g$ and $r$ photometry (reaching out to $\sim 2$ magnitudes below the oldest main-sequence turn-off and covering $\sim 20$ deg$^2$) around the Sextans dwarf spheroidal galaxy. We aim to use this dataset to study the structural properties of Sextans overall stellar population and its member stars in different evolutionary phases, as well as to search for possible signs of tidal disturbance from the Milky Way, which would indicate departure from dynamical equilibrium.

**Methods.** We performed the most accurate and quantitative structural analysis to-date of Sextans' stellar components by applying Bayesian Markov chain Monte Carlo methods to the individual stars' positions. Surface density maps are built by statistically decontaminating the sample through a matched filter analysis of the colour-magnitude diagram, and then analysed for departures from axisymmetry.

**Results.** Sextans is found to be significantly less spatially extended and more centrally concentrated than early studies suggested. No statistically significant distortions or signs of tidal disturbances were found down to a surface brightness limit of $\sim 31.8$ mag/arcsec$^2$ in V-band. We identify an overdensity in the central regions that may correspond to previously reported kinematic substructure(s). In agreement with previous findings, old and metal-poor stars such as Blue Horizonal Branch stars cover a much larger area than stars in other evolutionary phases, and bright Blue Stragglers (BSs) are less spatially extended than faint ones. However, the different spatial distribution of bright and faint BSs appears consistent with the general age and metallicity gradients found in Sextans' stellar

component. This is compatible with Sextans BSs having formed by evolution of binaries and not necessarily due to the presence of a central disrupted globular cluster, as suggested in the literature. We provide structural parameters for the various populations analysed and make publicly available the photometric catalogue of point-sources as well as a catalogue of literature spectroscopic measurements with updated membership probabilities.[1]

## 2.1 Introduction

In this chapter, we studied in detail the properties of the stellar component of the MW satellite Sextans, in search for the possible presence of signs of tidal disturbance, to quantify the structural properties of the overall stellar population and to constrain spatial variations in the properties of the stellar population mix as traced by stars found in different evolutionary phases.

Discovered in the UKST sky survey by Irwin et al. (1990), Sextans is a particularly intriguing object because it was found to have a very low central surface brightness ($\mu_V = 27.1$ mag/arcsec$^2$) and a much larger extent than other similarly luminous MW classical dSphs (a King tidal radius of 160 arcmin, corresponding to $r_t = 4.0$ kpc, assuming an heliocentric distance of $D_\odot = 86$ kpc by Lee et al. (2009); to be compared for example to King tidal radii of 1-2 kpc for Ursa Minor and Sculptor). These characteristics make Sextans a candidate for having experienced strong tidal disturbance from the MW, but at the same time hard to study in detail, due to the difficulties of mapping its properties over a large portion of its stellar body and of separating stars belonging to Sextans from the very numerous contaminants (e.g. foreground MW stars).

Its structural parameters were carefully derived for the first time in Irwin & Hatzidimitriou (1995) (hereafter IH95) from photographic plates, but it has been only very recently that this type of analysis has been carried out on deep photometry fully mapping the galaxy out to its outskirts (Roderick et al. 2016a, hereafter R16) or along portions of its major and minor axis (Okamoto et al. 2017). The surface density map by R16 exhibit significant distortions in the outer parts, although the main conclusion of the authors was that Sextans is not undergoing strong tidal disruption. R16 revised Sextans nominal King tidal radius down to a much smaller value of 83 arcmin, while Okamoto et al. (2017) obtained a value of 120 arcmin, although the limited spatial coverage of their dataset makes the determination uncertain.

The properties of Sextans' stellar population mix are known to vary spatially. By analysing the colour-magnitude diagram (CMD) of the central

[1]Full Tables 2.2 and 2.6 are only available at the CDS via anonymous ftp to `cdsarc.u-strasbg.fr` (`130.79.128.5`) or via `http://cdsarc.u-strasbg.fr/viz-bin/qcat?J/A+A/609/A53`

$\sim 33 \times 34$ arcmin$^2$ of Sextans, Bellazzini et al. (2001) found evidence for the presence of at least two components in the old stellar population of this galaxy, with the main one having [Fe/H] $\sim -1.8$ and a minor component around [Fe/H] $\sim -2.3$, and hints that the blue horizontal branch (BHB) stars are less spatially concentrated than the stars in the other evolutionary phases analysed. Later, Lee et al. (2003), R16 and Okamoto et al. (2017) confirmed the larger extent of BHB stars, although they do not provide a quantification of the different spatial distribution of the stellar populations in terms of structural parameters.

Using metallicities ([Fe/H]) from Ca II triplet nIR lines for a sample of $\sim 150$ RGB stars that are probable members of Sextans, Battaglia et al. (2011) found a negative metallicity gradient, with the metallicity distribution function (MDF) having an average of [Fe/H] $= -2.73$ with 0.24 dex of dispersion in the outer parts ($R > 0.8°$) while in the inner parts ($R < 0.8°$) the MDF is well represented by a sum of two gaussians, one with the same average and dispersion as in the outer parts and the other with [Fe/H] $= -2.04$ and 0.25 dex of dispersion. Even though the mean values of the MDF components differ, this finding is in agreement with the presence of two populations suggested by Bellazzini et al. (2001), the radial variation of the star formation history derived by Lee et al. (2009) and the age gradient later found by Okamoto et al. (2017), where RHB and BHB stars seem to be associated to the metal rich/younger (more centrally concentrated) and metal poor/old (more spatially extended) populations respectively.

Also the properties of Sextans BSs exhibit spatial variations, with the bright (more massive) blue stragglers being more centrally concentrated than the fainter (less massive) ones (Lee et al. 2003). Kleyna et al. (2004) found a cold kinematic substructure close to the centre of the Sextans dSph (see also Battaglia et al. 2011 and Walker et al. 2006, the latter for a substructure close to Sextans core radius) and suggested that the central cold substructure, the spatial distribution of bright and faint BSs and the sharp central rise in the light distribution of Sextans (e.g. IH95), could be explained by the dissolution of a stellar cluster in Sextans' centre.

In this chapter we present an extensive wide-field study of Sextans' stellar population using deep $g-$ and $r-$ band photometry (reaching down to $\sim 2$ magnitudes below the oldest MSTO) from a mosaic of CTIO/DECam pointings over $\sim 20$ deg$^2$ along the line-of-sight to the Sextans dSph. This reaches well beyond the nominal IH95 King tidal radius. We performed a detailed and quantitative analysis of the structural properties of this galaxy, using statistically sophisticated tools. This chapter is organized as follows. Section 2.2 presents the details of our observations, the data reduction process and the resulting photometric catalogue, which we make publicly available. In Sect. 2.3 we ex-

tract the structural parameters of the overall stellar population of the galaxy, evaluate the goodness-of-fit of different functional forms for the surface density profile and measure the integrated magnitude and central surface brightness. In Sect. 2.4 we derive Sextans decontaminated surface density map, its deviations from axisymmetry and the two-dimensional classical likelihood ratios between the best-fitting density profiles. The analyses carried out over the whole population of Sextans are applied to the stars in different evolutionary phases in Sect. 2.5. In Sect. 2.6, we use our results to update membership probabilities of stars from the Walker et al. (2009b) and Battaglia et al. (2011) spectroscopic samples and make the resulting catalogue publicly available. Finally, Sect. 2.7 is dedicated to the summary and conclusions of this work.

## 2.2 Observations and data reduction

The observations were carried out between March 18 and 23 2015 by L. Cicuéndez in visitor mode with the instrument DECam on the 4m Blanco telescope at the CTIO, Chile (PI: B. McMonigal). DECam is a wide-field CCD imager containing 62 2048×4096 pixel CCDs, producing images with a field of view (FoV) of 2.2 degrees at 0.263 arcsecond/pixel resolution.

The initial plan for the observations consisted of a mosaic composed of 14 pointings centered on the Sextans dSph and probing out to twice its nominal King tidal radius (adopting the structural parameters derived by IH95), plus two displaced ones in order to measure the contamination density (Fig. 2.1). However, because of bad weather conditions, only six pointings from the mosaic could be observed (#1−#6 in Fig. 2.1), plus one displaced pointing (#8). In order to enlarge the area covered along the projected minor axis, we added one pointing (#7) from the public data at the NOAO Science Archive, forming part of the proposal 2013A-0611 (PI: A.D. Mackey). The complete map covers approximately 20 $\deg^2$, reaching out to slightly beyond the IH95 estimate of Sextans' nominal King tidal radius.

All the pointings but #7 were observed with multiple exposures of 300s $g-$ and 500s in $r-$ band, dithering with spatial offsets between the individual exposures chosen to fill the gaps between CCDs. On the other hand, pointing 7 had been observed with 3x300s exposures in $g-$ and $i-$ bands, without dithering. The log of the observed fields is shown in Table 2.1.

The data were processed by the Cambridge Astronomical Survey Unit (CASU), using the pipeline described in Irwin & Lewis (2001) in an optimized form for working with DECam data. This pipeline performs standard reductions (debiasing, flat-fielding, astrometry and internal photometric calibration between pointings), classifies the detected objects morphologically and gener-

| Pointing | $\alpha_{2000}$ (hh:mm:ss) | $\delta_{2000}$ (dd:mm:ss) | UT date (dd:mm:yyyy) | Filter | Average sec z | Average seeing ($''$) |
|---|---|---|---|---|---|---|
| 1 | 10:15:44.17 | -01:09:42.39 | 19/03/2015 | g | 1.53 | 1.22 |
| | | | | r | 1.36 | 0.98 |
| 2 | 10:10:21.84 | -02:04:03.61 | 19/03/2015 | g | 1.22 | 0.98 |
| | | | | r | 1.16 | 0.97 |
| 3 | 10:09:54.72 | -00:30:58.14 | 19/03/2015 | g | 1.19 | 1.19 |
| | | | | r | 1.35 | 1.38 |
| 4 | 10:15:34.80 | +00:23:24.00 | 22/03/2015 | g | 1.17 | 1.25 |
| | | | | r | 1.16 | 1.17 |
| 5 | 10:21:33.60 | -01:48:36.80 | 23/03/2015 | g | 1.49 | 1.01 |
| | | | | r | 1.33 | 0.92 |
| 6 | 10:04:59.52 | -02:58:24.60 | 23/03/2015 | g | 1.17 | 0.98 |
| | | | | r | 1.14 | 0.88 |
| 7 | 10:17:03.30 | -02:31:53.00 | 16/02/2013 | g | 1.22[1] | 1.43 |
| | | | | i | 1.27[1] | 1.33 |
| 8 | 10:34:00.00 | -01:30:00.00 | 19/03/2015 | g | 1.15 | 1.08 |
| | | | | r | 1.14 | 0.94 |

Table 2.1: Log of the observed fields combined into the analysed map.
[1]Via `www.eso.org/sci/observing/tools/calendar/airmass`

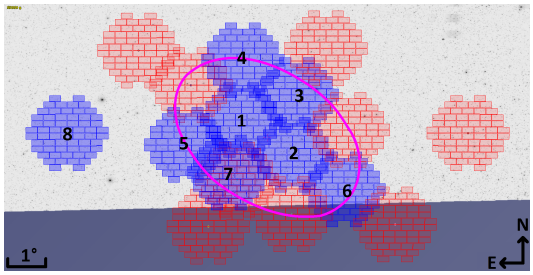


Figure 2.1: Location of the observed (numbered) and planned (not numbered) DECam pointings around the Sextans dSph, overlaid to SDSS DR9 $g$ band imaging, which covers almost entirely the surveyed area (the blue band is the region lacking SDSS DR9 coverage). Pink ellipse: Contour of the previously estimated King surface density profile of Sextans at its tidal radius. Pointing 7 is from archive DECam observations. The DECam FoV used to prepare this image in Aladin Sky Atlas (Bonnarel et al. 2000) was designed by L. Cicuéndez.

ates their corresponding photometric catalogue. The morphological classification was done by allowing the point spread function (PSF) to be determined independently per CCD and filter.

Even though we did not perform artificial star tests, we are confident that our data do not suffer from crowding: datasets suffering from crowding will show a shallower limiting magnitude in the densest regions, as well as an increase of sources classified as extended/blends. We have verified that in the innermost regions the spatial distributions of extended and noise-like objects does not show any such feature, as well as that the limiting magnitude of the data in the central region compares well to the rest of the dataset.

Hereafter, unless otherwise stated, we will only refer to objects classified as point-like in both photometric bands to exclude background galaxies, blends or noise detections. Given the comparable depth of the $g-$ and $r-$ photometry, information from both bands should provide a more reliable morphological classification. For each point-like object the pipeline assigned a morphological classification flag per photometric band whose possible values are $-1$, $-2$ or $-3$, which correspond to an identification as an almost certain star, a probable star or a star/compact galaxy respectively.

The photometry of the mosaic was first calibrated internally (in instrumental magnitudes) using the overlapping regions between pointings; obviously this step could not be applied to the displaced pointing. As pointing 7 was originally observed in $g$ and $i$ bands, for its initial internal calibration with the rest of the mosaic we inferred the $r_{instr.}$ band magnitudes by applying the linear equation

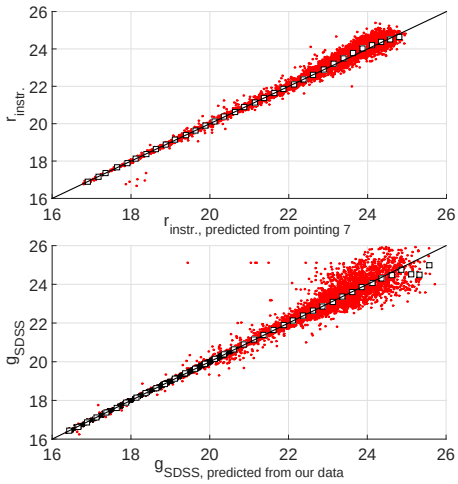


Figure 2.2: Top: Linearity check of the photometric conversion to $r_{instr.}$ of pointing 7 through its overlapping regions with the rest of the mosaic. Bottom: Linearity check of the photometric calibration with SDSS, in this case for pointings from the mosaic in g band. The stars used for the linear fitting are shown as black dots, and are the majority of those having $g_{\rm SDSS} \lesssim 20.5$, while the stars not used are shown as red dots (outliers or those with errors larger than 0.03 mag). In both panels the white squares give the median values in 0.25 mag-wide bins and the black line shows the one-to-one relation.

$r_{instr.} - g_{instr.} = c_r\,(g_{instr.} - i_{instr.}) + ZP_r$ (Fig. 2.2) to the objects overlapping between our mosaic and the one from the original proposal of pointing 7; in this case, we find a colour term $c_r = -0.7101$, with a scatter of $\sigma_r = 0.0229$ mag around the relation. The agreement between the measured $r_{instr.}$ band magnitudes and those predicted by the relation is very good, with only a slight deviation for the faintest sources (see top panel Fig. 2.2).

The photometric calibration was performed by cross-correlating our DECam catalogue with the SDSS DR12 point-like catalogue (Alam et al. 2015) in $g_{SDSS}$ and $r_{SDSS}$ bands, for the mosaic area at once and for the displaced pointing independently. A linear fitting was sufficient for the purpose (Fig. 2.2):

$$\begin{aligned} g_{instr.} - g_{SDSS} &= c_g\,(g_{instr.} - r_{instr.}) + ZP_g\,, \\ r_{instr.} - r_{SDSS} &= c_r\,(g_{instr.} - r_{instr.}) + ZP_r\,. \end{aligned} \tag{2.1}$$

In order to reject outliers, we applied the bisquare weights method inside a loop to recursively discard objects beyond $3\sigma$ from the linear fitting in each iteration, until convergence. The standard deviation was calculated from the median absolute deviation (MAD) through the expression: $\sigma = \frac{MAD}{\phi^{-1}(3/4)} \simeq 1.4826 \cdot \mathrm{MAD}$, where $\phi^{-1}$ is the quantile function for the standard normal distribution. The resulting colour terms are $c_g = -0.0974$ and $c_r = -0.102$, with a scatter of $\sigma_g = 0.030$ mag and $\sigma_r = 0.024$ mag. The bottom panel of Fig. 2.2

shows that the transformation holds well down to the faintest magnitudes. The positions of the stars retained by the linear fitting after rejecting all the outliers through this cleaning method agree with the SDSS astrometry within $\sim 0.3''$. The depth of the dataset is $M_{g,\,AB} \simeq 25.1$ and $M_{r,\,AB} \simeq 24.9$ at S/N $\simeq 5$, $M_{g,\,AB} \simeq 25.8$ and $M_{r,\,AB} \simeq 25.4$ at S/N $\simeq 3$.

We corrected the photometrically calibrated $g-$ and $r-$ magnitudes for Galactic extinction using the Schlegel et al. (1998) dust map together with its 14% reddening recalibration and extinction coefficients derived by Schlafly & Finkbeiner (2011). Due to variations of the extinction across the large observed area, we corrected it star by star, limited by the spatial resolution of the dust map. For our observed fields the median values of the extinction were $A_g = 0.144$ mag and $A_r = 0.100$ mag, the maximum were $A_g = 0.247$ mag and $A_r = 0.171$ mag and the minimum $A_g = 0.080$ mag and $A_r = 0.056$ mag. Hereafter, we only show the extinction and reddening corrected photometry. The catalogue of point-like sources is given in Table 2.2.

The corrected CMDs of the individual pointings are shown in Fig. 2.3. The features of Sextans stellar population (main sequence, main sequence turn-off, sub- and red giant branch, blue stragglers, red and blue horizontal branch) are clearly recognizable in field 1 and 2, becoming less evident in 3&7, while the rest of the fields appear to contain only Milky Way stars and unresolved background galaxies.

Among the aims of our study was to explore the 2D structural properties of the Sextans stellar population, both by determining Sextans structural parameters and surface density profile, and by investigating the possible presence of signs of tidal disturbance, such as for example low surface density tidal debris or structural irregularities. However, on instruments with such a large field of view as DECam it is common that some regions are out of focus, in particular in the outer parts. The locations of these regions depend on the optical aberrations of the telescope, but also on factors that change from pointing to pointing, like the focus carried out at the beginning of each night or the inclination of the telescope, affecting the tilt of the focal plane or the tension on the mirrors. These distortions in the focal plane can lead to a morphological misclassification (see e.g. McMonigal et al. 2014) whose importance depends on such variables as the depth, the seeing, etc. which once again change from pointing to pointing. As a result, in the most out-of-focus regions extended objects tend to be detected as point-like ones due to our treatment of the point-spread-function across the field-of-view, resulting in artificial overdensities of point-like sources. In our case, these features become noticeable when including objects fainter than $(g, r) = (23.0, 23.0)$ mag, which is approximately the region where the locus of unresolved galaxies starts appearing on the CMD. This is clearly

| ID | $\alpha_{2000}$ (hh:mm:ss) | $\delta_{2000}$ (dd:mm:ss) | g (mag) | g class | r (mag) | r class | E(B-V) (mag) |
|---|---|---|---|---|---|---|---|
| 1 | 10:13:29.2581 | -01:11:4.808 | 24.736±0.199 | -1 | 24.870±0.160 | -1 | 0.03966 |
| 2 | 10:14:02.1465 | -01:11:5.040 | 21.318±0.047 | -1 | 19.874±0.025 | -1 | 0.04122 |
| 3 | 10:13:37.9707 | -01:11:5.391 | 24.285±0.141 | -1 | 24.400±0.109 | -3 | 0.03982 |
| 4 | 10:13:57.1101 | -01:11:7.043 | 24.411±0.145 | -2 | 24.325±0.097 | -3 | 0.04205 |
| 5 | 10:13:55.6720 | -01:11:7.195 | 24.427±0.145 | -2 | 24.124±0.081 | -1 | 0.04205 |
| 6 | 10:14:32.6120 | -01:11:8.072 | 24.693±0.171 | -1 | 23.898±0.067 | -3 | 0.04309 |
| 7 | 10:14:29.1699 | -01:11:8.671 | 25.059±0.241 | -1 | 25.054±0.176 | -1 | 0.04361 |
| 8 | 10:14:34.0414 | -01:11:8.968 | 22.127±0.050 | -1 | 21.948±0.028 | -1 | 0.04309 |
| 9 | 10:13:37.0119 | -01:11:8.972 | 24.576±0.167 | -3 | 24.003±0.077 | -1 | 0.03982 |
| 10 | 10:14:17.7718 | -01:11:9.697 | 23.896±0.091 | -1 | 22.242±0.029 | -1 | 0.04281 |
| ... | ... | ... | ... | ... | ... | ... | ... |

Table 2.2: Sample of the Sextans point-like catalogue in SDSS photometric system. The classification flags in each band are described in Sect. 2.2. The reddening E(B-V) was derived from Schlegel et al. (1998) dust map. The full photometric catalogue is available online together with the electronic version of the corresponding article.

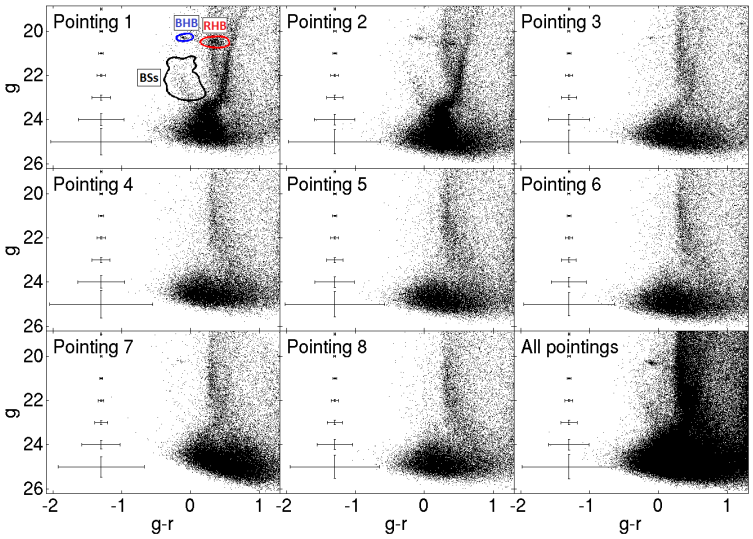


Figure 2.3: CMDs of the different DECam pointings, together with the representative $3\sigma$ errors in mag and colour (error bars on the left). MS, MSTO, BSs candidates, RGB, RHB and BHB features from Sextans stellar population are clearly visible in pointings 1 and 2, while in 3, 7 are less evident and in the rest they are indistinguishable from the contamination (remember that #8 is assumed to contain just contamination). In pointing #1 we also show the selection windows used to isolate RHB, BHB and BS stars later on. Pointing #4 is the shallowest pointing and #6 the deepest; #8 is displaced from the main mosaic area for foreground and background determination.

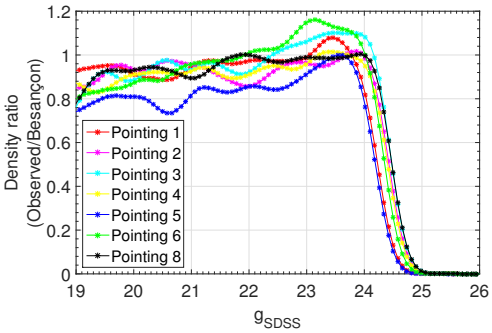


Figure 2.4: Ratios of the measured luminosity functions of Milky Way dwarf stars at $1.1 < g - r < 1.6$ for each pointing with the predictions from the Besançon model, after smoothing them with a gaussian of $\sigma_g \sim 0.2$ mag.

something that stands in the way of detecting low surface brightness features in surface density maps, hence in the following, unless specified otherwise, we perform our analysis on objects brighter than $(g, r) = (23.0, 23.0)$ mag. In Appendix A.1 we discuss the various attempts we made to overcome this issue. The chosen magnitude cut also ensures that all the pointings are at the $\sim 100\%$ completeness level; we have verified this statement by examining the ratio of the luminosity function of Milky Way dwarf stars at $1.1 < g - r < 1.6$ with the predictions from the Besançon model[2] (Robin et al. 2003): in the magnitude range considered, the ratio is constant around unity and then shows a clear, sharp drop-off at fainter magnitudes, around $\sim 24$ mag, when the completeness starts decaying (Fig. 2.4).

## 2.3 Structural parameters

In order to derive the structural parameters of the Sextans dSph whilst avoiding the loss of information due to spatial binning of the data, we used the method defined in the appendix of Richardson et al. (2011). This method works by evaluating likelihoods at each star's location given the expression of the galaxy surface density profile, which are also a function of the galaxy structural parameters (e.g. centre, ellipticity, position angle, etc.), and contamination density.

The likelihood of observing the $N$ data points at positions $\mathbf{r_i}$, with $i = 1, 2, ..., N$, for a given surface density profile $f(\mathbf{r})$ (dSph + contamination) is then:

$$\ln L = \int_S f(\mathbf{r})\, \mathrm{d}S + \sum_{i=1}^{N} ln\, f(\mathbf{r_i})\,, \tag{2.2}$$

[2] `http://model.obs-besancon.fr`

with the integral evaluated over the observed area $S$; $\mathbf{r_i}$ is the star's elliptical radius (the semi-major axis of the ellipse passing at the location of the star $i$) projected onto the tangent plane of the sky at the galaxy centre (in standard coordinates: $\xi, \eta$):

$$\mathbf{r_i}^2 = (\Delta\xi_i \sin\theta + \Delta\eta_i \cos\theta)^2 + (-\Delta\xi_i \cos\theta + \Delta\eta_i \sin\theta)^2/(1-\epsilon)^2\,, \qquad (2.3)$$

with $(\Delta\xi_i, \Delta\eta_i)$ being the star's displacement with respect to the galaxy centre, $\theta$ the position angle (measured north through east) of the ellipse and $\epsilon$ its ellipticity.

It is worth mentioning that one term is missing on the right-hand side of Eq. 2.2 from Richardson et al. (2011), that is $+\sum_{i=1}^{N} \ln dS$, evaluated over the stars' locations. This term makes the value of the likelihood $L$ essentially zero, as the surface density models give no probability of detecting stars in a zero surface area $dS$. Nonetheless, this zero-term is just a constant scale factor of $L$, so ignoring this term does not affect either the Markov chain Monte Carlo (MCMC) analysis or the evaluation of classical likelihood ratios and posterior Bayes factors (PBFs) explained later on in the section, given that this constant term cancels out because it only depends on the number of stars used for the fitting, which is the same for all profiles.

For the dSph surface number density profile, we explored the performance of an empirical King profile (King 1962), an exponential profile, a Sérsic profile (Sersic 1968) and a Plummer model (Plummer 1911). The surface density of foreground and background contaminants was instead modelled as a bilinear distribution, $f_{\rm cont} = \overline{\rho}\,(1 + a\xi + b\eta)$, in order to account for the expected spatial gradient in the density of MW contaminants, due to the relatively large area of the DECam dataset and its location on the sky. We remind the reader that the classical expression of the King profile is only defined until the tidal radius. Hence, the positive values given by its expression beyond it have to be replaced by zero independently of the fitting process carried out (see an example with nonzero values beyond the tidal radius in Fig. 5 from Okamoto et al. 2017).

The likelihood of each structural parameter can then be evaluated through the expression of $\ln L$ (Eq. 2.2) using a Bayesian MCMC analysis. In this case we used a Bayesian MCMC ensemble sampler with affine invariance of the form from Goodman & Weare (2010): 'The MCMC Hammer' (Foreman-Mackey et al. 2013); the code we are using[3] was developed at Centre for Ice and Climate (Niels Bohr Institute). This code allows us to sample the entire parameter space without fixing any value and thanks to its affine invariance the performance does not depend on the aspect ratio in probability distributions

[3] https://github.com/grinsted/gwmcmc

strongly affected by anisotropy. In the MCMC Hammer we defined 80 walkers, each of them doing approximately $10^4$ steps. The priors for the structural parameters were chosen according to the values given by IH95 and by restricting the domain of each parameter to the region physically possible.

Due to Sextans' relatively low Galactic latitude, a large number of (mainly foreground) Milky Way stars are expected to contaminate the photometric catalogue, in addition to unresolved background galaxies. We exploited the information contained in the CMD so as to limit the amount of such contaminants. Figure 2.5 shows high resolution Hess diagrams, built over a very fine grid in colour and magnitude, which we obtained by first applying a gaussian smoothing dependent on each object's location in accordance to its photometric errors in both bands and then a global gaussian smoothing to fill in the remaining holes caused by the low density of point-like objects on the CMD, with $\sigma_{g-r} \simeq 0.06$ mag and $\sigma_g \simeq 0.1$ mag. The left panel shows the Hess diagram corresponding to the central part of Sextans (i.e. within the central $\sim$10 arcmin), while on the righthand side we show the one corresponding to the displaced pointing (#8). From now on, unless otherwise stated, we will only consider point-like sources inside the region of the CMD where most of Sextans stellar population is contained, defined as the region within a contour at approximately 10% the maximum value of the Hess diagram from the central part of the galaxy and excluding objects with $g - r > 1$, as they correspond mainly to MW dwarf stars. On the other hand, in order to gain statistics, the $a$ and $b$ parameters in the expression of $f_{\rm cont}$ were derived without using the window in the Hess diagram (Fig. 2.5).

For the contaminants, we obtain $\overline{\rho} = 0.274^{+0.003}_{-0.003}$ stars/arcmin$^2$, $a = -1.27^{+0.19}_{-0.17}$ %/deg and $b = -4.37^{+0.45}_{-0.45}$ %/deg, which produces a trend of increased contamination in the same direction as in the Besançon model of the Milky Way stellar populations (Robin et al. 2003), as expected, and yields a difference of $\sim$30% contamination between the edges of our DECam dataset (Fig. 2.6), supporting the appropriateness of allowing for a spatially variable contamination density.

As an example, Fig. 2.7 shows the Bayesian posterior distributions of the parameters obtained when modelling the dSph surface number density as an empirical King profile: we can see that the distributions are nearly Gaussian, hence well behaved, and the parameters well-constrained, with most of them being uncorrelated to each other. The good performance of the best-fitting King model is also evidenced by the agreement with the observed surface number density profile as a function of major axis radius in Fig. 2.8. The comparison between data and model also shows no significant overdensities of stars with respect to an empirical King profile which could have been interpreted as extratidal stars.

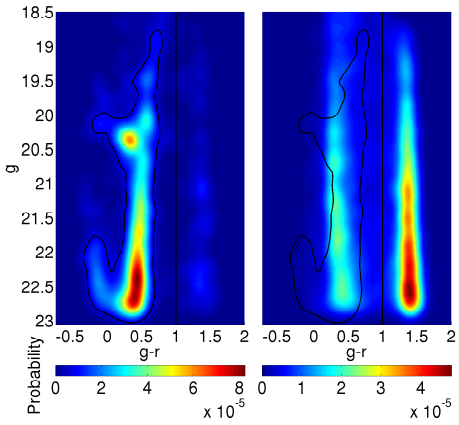


Figure 2.5: High resolution Hess diagrams from two different spatial regions. Left: central parts of Sextans (MFM signal filter). Right: pointing #8 (MFM contamination filter). Stars redder than $g - r = 1$ (black vertical line) were excluded from the analysis. Black contours: window defined to exclude most contaminants. Hess diagrams are colour-coded according to the probability of finding a star with a given mag and colour.

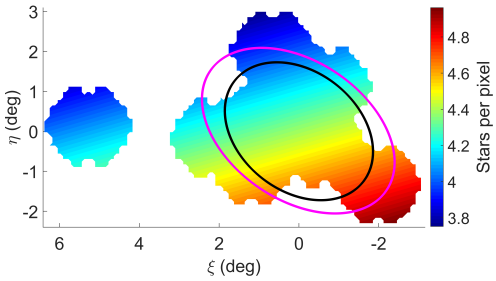


Figure 2.6: Modelled bilinear contamination map fitted with the MCMC Hammer. The pink and black ellipses show the nominal King tidal radius with parameters from IH95 and this work, respectively.

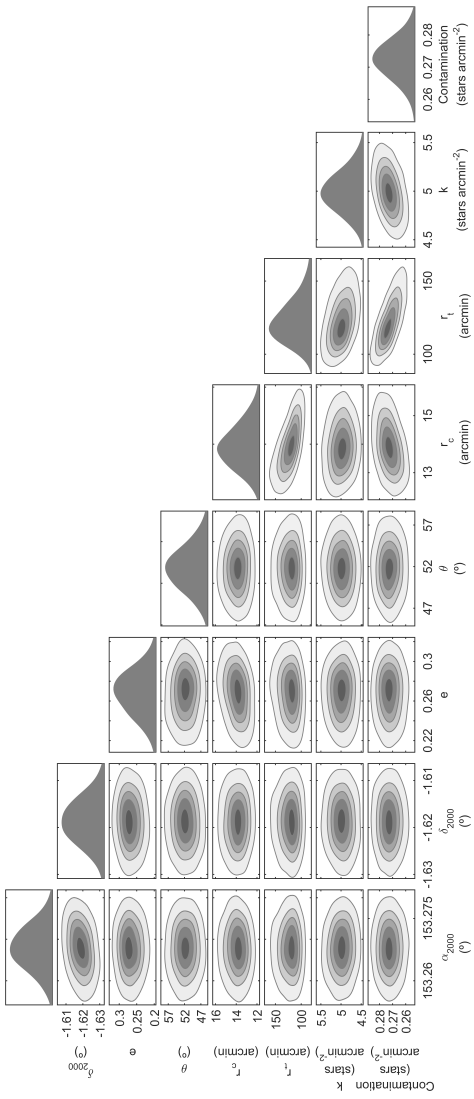


Figure 2.7: Bayesian posterior distributions of the structural parameters obtained with the MCMC Hammer when modelling the dSph surface number density as an empirical King profile. Contours contain 10%, 30%, 50%, 70% and 90% of the points sampled by the MCMC Hammer. From left to right: RA ($\alpha_{2000}$), DEC ($\delta_{2000}$), ellipticity ($e = 1 - b/a$), position angle ($\theta$), core radius ($r_c$), tidal radius ($r_t$), scale factor (k) and contamination density. Two-dimensional normal distributions aligned with $x$- and $y$-axes are indicative of uncorrelated parameters.

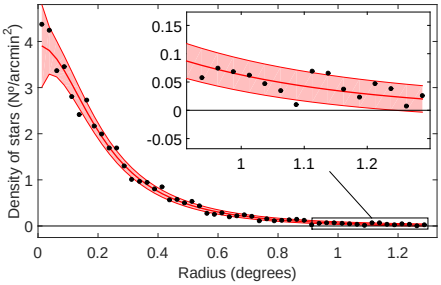


Figure 2.8: Contamination subtracted surface number density profile of Sextans stars as a function of the major axis radius (with the external parts zoomed in), overlaid onto the $1\sigma$ confidence interval (red band) of the best-fitting King profile obtained with the MCMC Hammer. The $1\sigma$ confidence interval is computed from the best-fitting model assuming Poisson variances in each elliptical annulus. We do not use a logarithmic scale so as to be able to show the density fluctuations below the estimated background (negative values); otherwise plots mimic the presence of extra-tidal stars.

Table 2.3 summarizes the results of the procedure. The 2D half-light radius $r_h$ corresponding to the various functional forms were derived using the formulas in Wolf et al. (2010). The values and errors quoted are derived from the median and percentiles 15.87-84.13 (corresponding to $\pm1\sigma$ in case of normal distributions) of the marginalized Bayesian posterior distributions. In Appendix A.2 we tested the performance of our fitting method by applying it to a set of mock galaxies created under different conditions, such as number of stars, galaxy's ellipticity and spatial coverage of the dataset with respect to the galaxy's extent. We find that, for conditions similar to the ones of the photometric sample we are using here, the input parameters for all the generated mock galaxies are within the $1\sigma$ confidence level; it should however be kept in mind that this approach has implicit the assumption that the models are a good representation of the data. Nonetheless, we can see that the values of the centre, ellipticity, position angle and 2D half-light radius we obtain from our DECam catalogue (Tab. 2.3) are stable against the different functional forms for the surface number density profile, within the formal $1\sigma$ uncertainties.

Table 2.3 lists several indicators of the goodness-of-fit, such as the reduced chi-squared $\chi^2_{red}$, the classical ratio of maximum likelihoods, as well as the PBF, in the alternative way described by Aitkin (1991). The evidence is classified using the scheme in Table A.2. We refer the reader to Appendix A.3 for an extensive explanation on the definition of these goodness-of-fit indicators and their advantages and disadvantages. Here it suffices to say that we consider

| Parameter | Exponential | Sérsic | Plummer | King | IH95 | R16 |
|---|---|---|---|---|---|---|
| $\alpha_{2000}$ (º) | $153.268^{+0.006}_{-0.006}$ | $153.269^{+0.006}_{-0.006}$ | $153.268^{+0.006}_{-0.006}$ | $153.268^{+0.006}_{-0.006}$ | $153.2625^{+0.0005}_{-0.0005}$ | $153.277^{+0.003}_{-0.003}$ |
| $\delta_{2000}$ (º) | $-1.618^{+0.006}_{-0.006}$ | $-1.618^{+0.006}_{-0.005}$ | $-1.620^{+0.006}_{-0.006}$ | $-1.619^{+0.006}_{-0.005}$ | $-1.6147^{+0.0003}_{-0.0003}$ | $-1.617^{+0.008}_{-0.008}$ |
| Ellipticity | $0.27^{+0.03}_{-0.03}$ | $0.27^{+0.03}_{-0.03}$ | $0.27^{+0.03}_{-0.03}$ | $0.27^{+0.03}_{-0.03}$ | $0.35^{+0.05}_{-0.05}$ | $0.29^{+0.03}_{-0.03}$ |
| Position angle (º) | $52^{+3}_{-3}$ | $52^{+3}_{-3}$ | $52^{+3}_{-3}$ | $52^{+3}_{-3}$ | $56^{+5}_{-5}$ | $58^{+6}_{-6}$ |
| Sérsic index n | - | $1.03^{+0.07}_{-0.07}$ | - | - | - | - |
| Sérsic factor b(n) | - | $1.6^{+0.7}_{-0.6}$ | - | - | - | - |
| Exponential $r_e$ (′) | $12.7^{+0.4}_{-0.4}$ | - | - | - | $15.5^{+0.1}_{-0.1}$ | - |
| Plummer $r_p$ (′) | - | - | $22.8^{+0.7}_{-0.7}$ | - | - | $35.7^{+0.7}_{-0.7}$ |
| Sérsic $r_s$ | - | $20^{+8}_{-8}$ | - | - | - | - |
| King $r_c$ (′) | - | - | - | $13.8^{+0.9}_{-0.9}$ | $17^{+2}_{-2}$ | $27^{+2}_{-2}$ |
| King $r_t$ (′) | - | - | - | $120^{+20}_{-20}$ | $160^{+50}_{-50}$ | $83^{+8}_{-8}$ |
| 2D half-light $r_h$ (′) | $21.4^{+0.7}_{-0.6}$ | $20^{+8}_{-8}$ | $22.8^{+0.7}_{-0.7}$ | $22^{+2}_{-2}$ | $26^{+0.2}_{-0.2}$ (Exp.)<br>$28^{+5}_{-5}$ (King) | $35.7^{+0.7}_{-0.7}$ (Plummer)<br>$24^{+2}_{-2}$ (King) |
| $\chi^2_{red}$ | 0.92 | 1.03 | 0.88 | 1.06 | 1.22 (Exp.)<br>1.57 (King) | 5.53 (Plummer)<br>3.15 (King) |
| $2\ln\left(\frac{\text{likelihood}_1}{\text{likelihood}_2}\right)$ | 0.3 $\left(\frac{\text{Exp.}}{\text{Sérsic}}\right)$ | 2.2 $\left(\frac{\text{Sérsic}}{\text{Plummer}}\right)$ | - | 2.7 $\left(\frac{\text{King}}{\text{Exp.}}\right)$ | -63.1 $\left(\frac{\text{Exp. IH95}}{\text{Plummer}}\right)$<br>-48.2 $\left(\frac{\text{King IH95}}{\text{Plummer}}\right)$ | -336.9 $\left(\frac{\text{Plummer R16}}{\text{Plummer}}\right)$<br>-160.7 $\left(\frac{\text{King R16}}{\text{Plummer}}\right)$ |
| $2\ln$(PBF) | 0.8 $\left(\frac{\text{Exp.}}{\text{Sérsic}}\right)$ | 1.8 $\left(\frac{\text{Sérsic}}{\text{Plummer}}\right)$ | - | 1.6 $\left(\frac{\text{King}}{\text{Exp.}}\right)$ | -58.2 $\left(\frac{\text{Exp. IH95}}{\text{Plummer}}\right)$<br>-32.7 $\left(\frac{\text{King IH95}}{\text{Plummer}}\right)$ | -331.9 $\left(\frac{\text{Plummer R16}}{\text{Plummer}}\right)$<br>-157.7 $\left(\frac{\text{King R16}}{\text{Plummer}}\right)$ |

Table 2.3: Sextans structural parameters (median values of the marginalized posterior distributions) derived with the MCMC Hammer, plus $\chi^2_{red}$, classical likelihood ratios and posterior Bayes factors of the different surface density profiles. Classical likelihood ratios and PFBs are colour-coded according to Table A.2, with blue, magenta and red fonts associated to evidences classified as not worth more than a bare mention, positive evidence and very strong evidence, respectively. The last two columns refer to the best-fitting profiles for which the structural parameters and scale radii were fixed to the values derived by IH95 and R16.

the PBF as the most reliable discriminant between different profiles, since it does not require any assumption on the data distribution around the model nor spatial binning, and it takes into account the full posterior distribution of parameters values. In order to allow for a fair comparison with the best-fitting models derived in the literature, we also re-performed the MCMC Hammer analysis on our dataset by fitting only the scale factors and contamination densities corresponding to our catalogue, while keeping the rest of the structural parameters fixed to the values published by IH95 and R16, and computing the corresponding values of the goodness-of-fit indicators.

Our determinations of the centre, ellipticity and position angle are in good agreement with those by IH95 and R16. On the other hand, our 2D half-light radius is smaller than previous determinations and in very strong disagreement with the half-light radius derived from the Plummer profile of R16. The classical likelihood ratio and PBF favour the King profile and show a very strong evidence (overwhelming in the scale of Aitkin 1991) in favour of the set of structural parameters derived in this work over previous determinations. Our photometric catalogue covers a very wide area and reaches deeper than the data from photographic plates on which IH95 work was based on, hence it is reasonable to expect the structural parameters to be better constrained here. On the other hand, the disagreement with the R16 work is unclear (but see Appendix A.1 for some considerations). Here we note that the 2D half-light radius derived from the best-fitting parameters of the R16 King and Plummer model are incompatible with each other, which is not seen either between our four models or in the IH95 best-fitting King vs. exponential. Further, we also note that using the structural parameters provided by R16, we could not reproduce the Plummer profile in their Fig. 8.

In summary, the overall stellar population of Sextans is likely to be more spatially concentrated than previously considered, with a 2D half-light radius of ∼22 arcmin, and with a shorter tidal radius, of ∼120 arcmin. This approach confirms the King profile as the best representation of the surface number density of Sextans given the DECam catalogue used here, as well as the corresponding values of the centre, ellipticity, position angle (and half-light radius).

In Appendix A.4 we repeat the analysis using the photometric catalogue cut at S/N=5 of the shallowest pointing, that is $(g, r) = (24.9, 24.9)$, in order to have larger statistics ($\sim$ 440,000 objects vs. $\sim$ 75,000 previously). We relegated this analysis to an appendix because, although some of the fitted structural parameters were significantly different from those in Table 2.3 (e.g. $r_h = 17^{+1}_{-1}$ arcmin for the King model), we could not exclude that the values obtained could be affected by small differences in depth between some pointings and the features corresponding to the out-of-focus regions.

We note that Sextans's dynamical mass within the half-light radius would become 80% and 60% of the values given in Walker et al. (2010) when adopting the 2D half-light radius from the King model $r_h$ we determined from our baseline 'bright' and S/N=5 catalogues respectively. This would increase the scatter in Walker et al. (2010) Fig. 5 in the regime of large $r_h$, but would not deviate considerably from the overall relation.

### 2.3.1 Integrated magnitude and central surface brightness

Here we use our data to revisit Sextans' integrated magnitude and central surface brightness values. Since our dataset does not reach down to several magnitudes below the oldest main sequence turn-off, we supplemented it with a synthetic colour magnitude diagram, in order to calculate the flux we are missing from the regions of the CMD we are not sampling.

The synthetic CMD was computed through the algorithm IAC-STAR[4] (Aparicio & Gallart 2004b). We used a star formation history and metallicity law broadly consistent with the observed properties for Sextans stars found by Lee et al. (2009) and Battaglia et al. (2011) respectively: the star formation rate was assumed constant for 13.7 to 10 Gyr ago, and null from 10 Gyr ago to the present day, while the metallicity was assumed to range between Z=0.0002 & 0.0008. We adopted the Teramo stellar evolutionary library (Pietrinferni et al. 2004) with the Lejeune et al. (1997) bolometric correction library, and adopted the default values for the other fields. The synthetic CMD was then shifted to Sextans' distance, adopting a distance modulus $(m\text{-}M)_0 = 19.67$ (Lee et al. 2009), and cut to match the range in magnitude and colour of our photometric catalogue; the Johnson-Cousin magnitudes were transformed into the SDSS system using the (B-V) → (g-B) and (V-R) → (r-R) equations by Jordi et al. (2006):

$$\begin{aligned} g &= 0.63B + 0.37V - 0.124\,, \\ r &= 0.733R + 0.267V + 0.088\,. \end{aligned} \tag{2.4}$$

The surface density profiles fitted to the photometric catalogue were used to obtain the enclosed total number of Sextans stars; from this we calculated a correction ratio, $K$, between the number of stars within $\sim 100\%$ completeness in our photometric catalogue and in the same magnitude range in the synthetic CMD. Assuming that the synthetic CMD is a fair representation of Sextans' CMD at all magnitudes, the integrated magnitude is:

$$V = -2.5 \log \left( K \sum_{i=1}^{n} 10^{-0.4 m_{V,i}} \right), \tag{2.5}$$

[4] http://iac-star.iac.es

where $m_{V,i}$ is the apparent V-mag of the stars in the synthetic CMD. The error in the integrated magnitude was calculated from the standard deviation of the total number of stars enclosed by the different surface density profiles and the error $\pm 0.1$ mag in the distance modulus (derived following Dolphin 2002).

With regard to the central surface brightness we inferred it from the Plummer profile, as it was the most likely in the central pixel of the decontaminated map. We calculated it through Eq. 2.5 as well, but replacing the scale factor $K$ by the ratio between the Plummer central density and the number of synthetic stars in the cut range of the CMD. The error on the central surface brightness was derived from the error in the central density of the best-fitting Plummer profile, obtained via the MCMC, and the error in the distance modulus.

This results in an apparent, absolute magnitude and central surface brightness in V-band: $V = 10.73^{+0.06}_{-0.05}$ mag, $M_V = -8.94^{+0.11}_{-0.09}$ mag and $\mu_V = 27.25^{+0.06}_{-0.05}$ mag/arcsec$^2$, respectively (these values are already corrected for Galactic extinction). We checked that the adoption of a different stellar library, for example the Bertelli et al. (1994) one, produces values within the derived errors (although we note that the Teramo stellar library reproduces better the observed CMD). These values are compatible with those by IH95, $M_V = -9.2 \pm 0.5$ mag and $\mu_V = 27.1 \pm 0.5$ mag/arcsec$^2$, but with considerably smaller errors.

## 2.4 Surface density maps

If present, tidal features are likely to have a very low surface density, hence efficient decontamination techniques are needed to enhance their signal over the numerous contaminants, such as 'matched-filtering' methods (MFM). These essentially exploit the different distributions of the source population and the contaminant population in some combination of observables (e.g. Kepner et al. 1999 and Rockosi et al. 2002). In the specific case, the Hess diagram of the densest regions of the dwarf galaxy, where the ratio contamination/source densities is the lowest, was used to build a 'source' filter, defining the shape of the dSph stellar population in the colour-magnitude plane; while a 'contamination filter' is obtained from a region far enough to be free of galaxy members, that is the displaced pointing #8 (see Fig. 2.5).

Next, we calculated a two-dimensional spatial histogram of the point-like objects in the catalogue. To this histogram we applied the MFM, in the improved form by McMonigal et al. (2014), which assumes Poisson rather than Gaussian statistics. The observed number of stars $n_i$ per four dimensional bin $i$ (spatial: $\xi, \eta$; Hess: magnitude and colour) follows a Poisson distribution of mean $\lambda_i = C_i + \alpha \cdot S_i$, with $\alpha$ being the expected number of dwarf galaxy members in the analysed spatial bin, $C_i$ the contamination filter scaled by the

expected number of contaminants in the same bin and $S_i$ the normalized source filter. The probability of the observed number of stars in the 4-dimensional $n_i$ for a given $\alpha$ is:

$$p(n_i \,|\, \alpha) = e^{-\lambda_i} \frac{\lambda_i^{n_i}}{n_i!} \,, \tag{2.6}$$

with the probability of $\alpha$ for a given spatial pixel given by the product of the individual probabilities $p(n_i \,|\, \alpha)$.

We performed a couple of improvements with respect to the MFM from McMonigal et al. (2014):

- We substituted the factorial in the Poisson distribution with its continuous version from the gamma function: $n! = \Gamma(n+1)$. Therefore, we do not need to have discrete counts in the bins of the Hess diagrams, allowing us to smooth them to fill in the holes due to the low density of galaxy members and to increment their resolution as much as we wish.
- We used a spatially varying contamination model instead of assuming it uniform. In practice, the contamination filter is normalized in the same manner as the source filter but multiplied by the expected number of stars from the contamination in the analysed spatial bin. The derivation of the contamination model was explained in Sect. 2.3.

The only restriction for the size of the spatial bins is to expect at least one contaminant per bin. Otherwise, for smaller bins, in those occupied even by only one contaminant star, $\alpha$ would be always greater than zero, in order to compensate for the fact that the expected number from the contamination filter of the MFM would be always less than one. Furthermore, in the limit of bin size equal to zero, the contamination filter would be null, hence we would not be applying the MFM at all. There is not an upper limit for the spatial bin size, but clearly the wider the bins the larger the number statistics, at the cost of degrading the spatial resolution of the maps. Taking all this into account we settled for a bin size of 4 arcmin per side.

The density map of Sextans' overall stellar population is displayed in the first panel of Fig. 2.9, in the form of iso-density contours, after smoothing it with a two-dimensional Gaussian of dispersion $\sigma_\xi = \sigma_\eta \sim 6$ arcmin. We used the results from Sect. 2.3 to determine down to which surface density levels we can confidently trace Sextans's stellar component by using the whole mosaic at once, rather than only pointing #8: we derived a two-dimensional map of residuals between the MFM decontaminated surface density map of Sextans's stars and the mean surface density predicted by the best-fitting Sersic, King, Plummer and exponential models, as well as a map of the scatter amongst the

models. These are visible in the second and third panels of Fig. 2.9, respectively, and except for a few over- and under-densities that we will discuss below, show a good agreement between the decontaminated map of Sextans stars and the models, independent on the adopted profile. Based on those maps, we made the assumption that the residuals are mostly artificial fluctuations without any evident spatial trend; we then analysed the frequency distribution of the residuals (inset in second panel of Fig. 2.9) and adopted the $1\sigma$ confidence interval as the $1\sigma$ precision of our method; this corresponds to $\sim 0.8$ stars/pixel ($\sim 31.8$ mag/arcsec$^2$ in V-band), equal to the 1% of the mean central density from the fitted models. We remind that the requirement of expecting at least one contaminant per cell (and thus the need to have pixels with 4 arcmin per side) plus the two-dimensional Gaussian smoothing of dispersion $\sigma_\xi = \sigma_\eta \sim 6$ arcmin, might hide some small-scale faint substructures whose surface brightness no longer reaches the $\sim 31.8$ mag/arcsec$^2$ detection limit in V-band after smoothing them with a kernel of $\sim \sqrt{6^2 + (4/2)^2} \simeq 6.3$ arcmin.

As a nice way of visualizing where, spatially, the various models are favoured or disfavoured, we show in Fig. 2.10 maps of the classical likelihood ratios between the best-fitting profiles, in increasing order of PFB, evaluating the likelihoods over the decontaminated surface density map (traced by the contours in Fig. 2.9). Thus we can see the regions where the less probable profile of the two best reproduces the decontaminated density map, even better than the (overall) more probable profile.

At the $2\sigma$ level, Sextans' density map appears regular, with no significant distortions in the outer parts, except for some overdensities beyond an elliptical radius of $\sim 1$ deg. As in R16, there is no detection of large scale tidal structures with a well defined spatial trend (e.g. tidal tails). The over-densities appearing in the displaced pointing might in principle be due to a slightly different photometric zero-point.

Besides the overdensities visible beyond $\sim 1$ deg radius, the two-dimensional map of residuals reveals also other over-dense small clumps as well as under-dense regions, which could not otherwise be appreciated in the surface density map. However, the statistical significance of these features is relatively low, $2\sigma$ and $3\sigma$ away from the background; hence we cannot exclude they are statistical fluctuations. The lack of underdensities beyond the central 1 deg is mainly due to the fact that when we apply the MFM in the form of McMonigal et al. (2014) we discard the possibility of having negative numbers of Sextans stars in any spatial pixel and beyond 1 deg the surface density profiles have low enough values to limit the resulted negative residuals below their $2\sigma$ detection.

While we do not detect any feature at the location where Walker et al. (2006) reported the presence of a kinematically cold substructure, the one/s

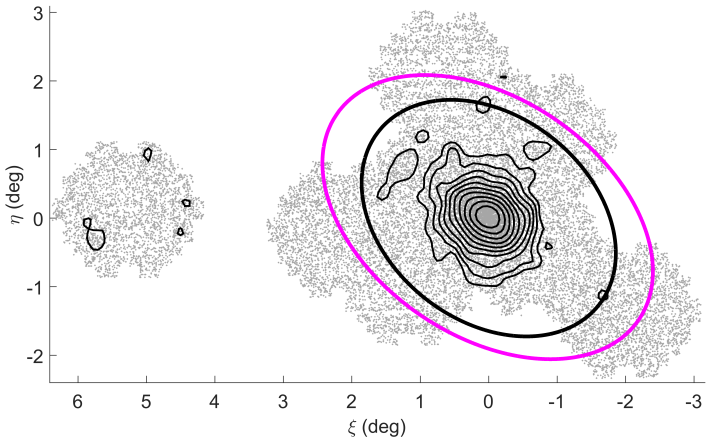


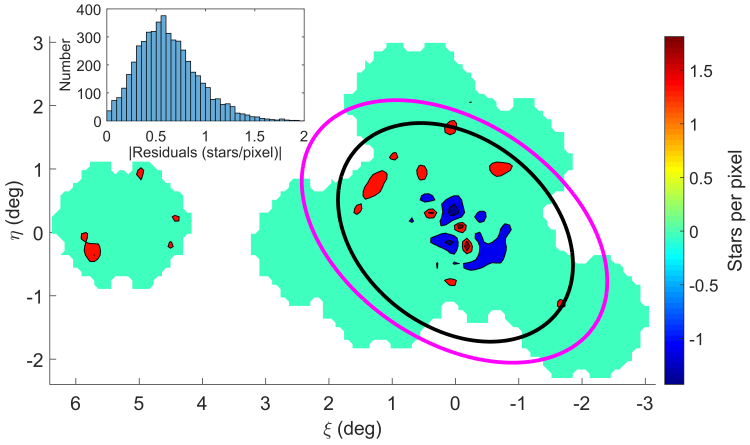

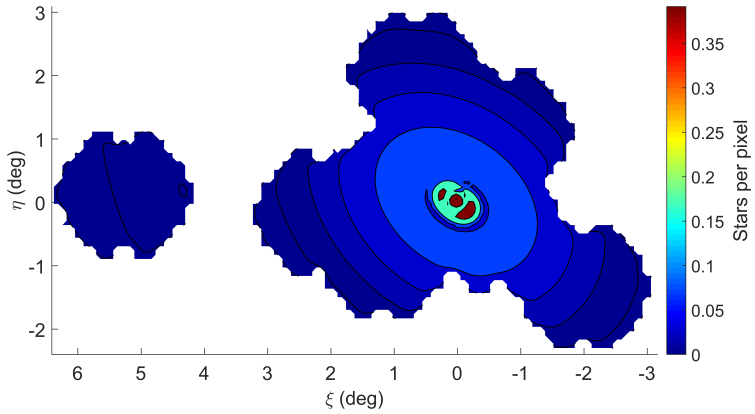


Figure 2.9: First: Spatial distribution of stars along the line-of-sight to the Sextans dSph, with overlaid iso-density contours from the MFM surface number density map. The pink and black ellipses show the nominal King tidal radius with parameters from IH95 and this work, respectively. The contours denote exponentially increasing values of surface number density, with the lowest one indicating a $2\sigma$ detection; the $3\sigma$ level is approximately the second contour. Second: Map of residuals between Sextans surface number density map from the MFM analysis and the mean surface density given by the best-fitting King, Sersic, Plummer and exponential profiles (for the parameters see Table 2.3), at $2\sigma$ and $3\sigma$ detections above and below the mean. The inset shows the frequency distribution of the residuals. Third: Standard deviation of residuals between the different fitted profiles; this shows the regions where the residuals depend on a given profile to a greater extent. It can be seen that the over- and underdensities hardly depend on the fitted profile, since their surface densities are considerably larger than the scatter between the different profiles.

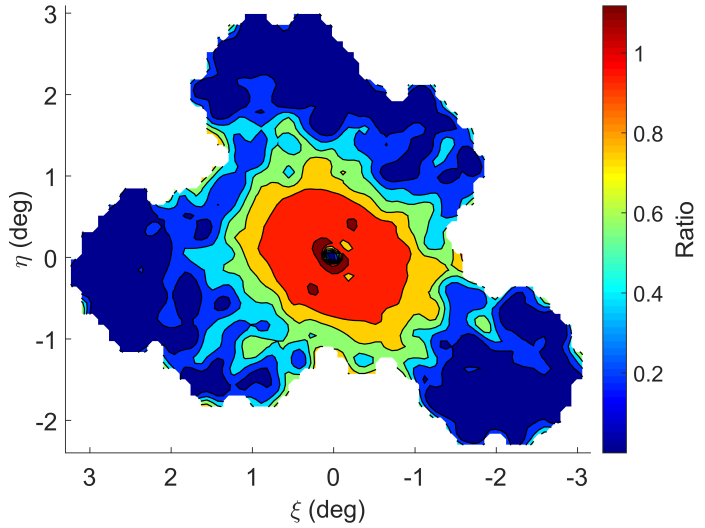


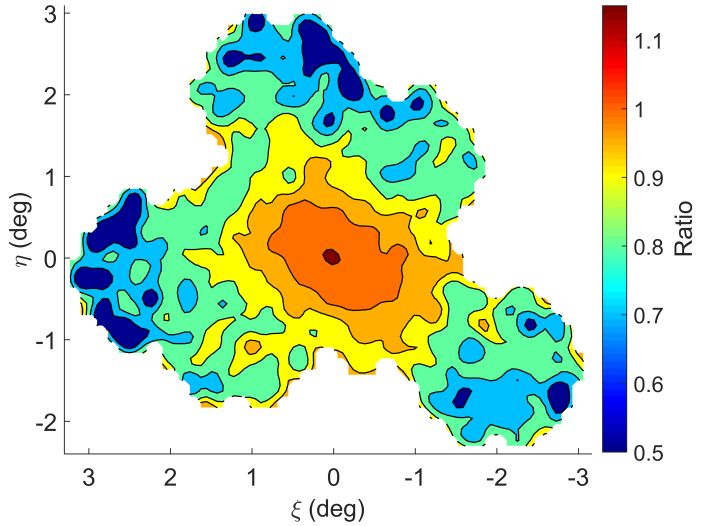

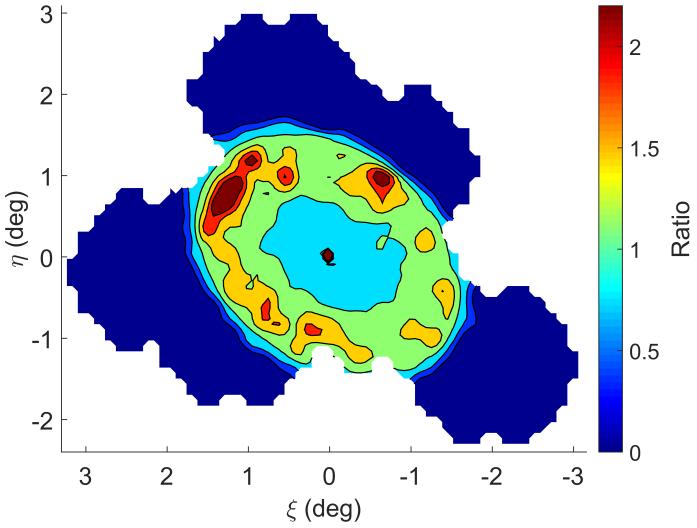


Figure 2.10: Maps showing classical likelihoods ratios between couples of best-fitting surface density profiles, calculated pixel by pixel, in increasing order of PBF. First: Sérsic/Plummer. Second: Exponential/Sérsic. Third: King/Exponential. Likelihoods were calculated based on the MFM decontaminated surface density map of Sextans' overall stellar population (First panel Fig. 2.9), assuming Poisson statistics at each spatial pixel. These maps allow us to detect the spatial regions where the less probable profiles fit better than the immediately more probable ones.

reported by Kleyna et al. (2004) and Battaglia et al. (2011) are found over a similar spatial region as the central overdensity and could therefore be related to it. The origin of the other detected over- and underdensities is unclear; in particular, to the best of our knowledge, so far there had not been reports of underdensities in the structure of classical dwarf spheroidal galaxies. In all cases the over- and underdensities we mapped are more than eight times away from the scatter amongst the different surface density profiles; this could indicate that most of these detections are real deviations from axisymmetry of Sextans stellar surface density, independent of the fitted profile. We also checked the map of objects classified as extended and found no correspondence between the detected overdensities and background galaxy clusters.

## 2.5 Spatial distribution of stars in different evolutionary phases

The analysis of the spatial distribution of stars in different evolutionary phases is a useful tool to study spatial variations of the stellar population mix as a function of age and/or metallicity, also when using relatively shallow photometry. Thereby one can infer information on the evolution of the galaxy stellar component as a function of time and space by analysing the spatial distributions of evolutionary phases indicative of different age ranges. There are multiple examples in the literature of this type of analysis, through which age gradients in Local Group dwarf galaxies have been quantified (e.g. Tolstoy et al. 2004, Battaglia et al. 2006; 2012a; 2012b, Bate et al. 2015). In the Carina dSph (McMonigal et al. 2014), the spatial distribution of main-sequence turn-off stars has revealed an angular offset between young, intermediate and old populations, as well as the presence of stars from the halo of the Large Magellanic Cloud along the line-of-sight to the Carina dSph.

Other possible applications are investigations on the origin of BSs in dSphs, via comparison of their spatial distribution with stars in other evolutionary phases: for example, the significantly more concentrated spatial distribution of BS candidates in Fornax with respect to the overall stellar population likely indicates these are genuine MS stars of young/intermediate age (Mapelli et al. 2009), while in Sculptor, Draco and Ursa Minor they are more likely to be actual blue stragglers produced by binaries mass transfer (Mapelli et al. 2007, 2009).

In this section, for the first time we performed a full MFM & statistical structural analysis of the spatial distribution of Sextans stars in different evolutionary phases, by applying the techniques explained in Sects. 2.3, 2.4 to Sextans RHB, BHB stars and BSs. The different stellar populations were isolated through selection windows in the CMD analogous to the one of Fig. 2.5 but

| Parameter | RHB | BHB | Bright BSs | Faint BSs |
|---|---|---|---|---|
| $\alpha_{2000}$ ($^o$) | $153.29^{+0.02}_{-0.02}$ | $153.21^{+0.05}_{-0.05}$ | $153.28^{+0.02}_{-0.02}$ | $153.25^{+0.03}_{-0.03}$ |
| $\delta_{2000}$ ($^o$) | $-1.60^{+0.02}_{-0.02}$ | $-1.60^{+0.05}_{-0.05}$ | $-1.63^{+0.02}_{-0.02}$ | $-1.64^{+0.02}_{-0.02}$ |
| Ellipticity | $0.29^{+0.08}_{-0.09}$ | $0.2^{+0.2}_{-0.2}$ | $0.2^{+0.2}_{-0.2}$ | $0.25^{+0.08}_{-0.1}$ |
| Position angle ($^o$) | $60^{+10}_{-10}$ | $60^{+20}_{-40}$ | $40^{+30}_{-20}$ | $50^{+20}_{-20}$ |
| 2D half-light $r_h$ ($'$) | $17^{+2}_{-2}$ | $42^{+7}_{-7}$ | $16^{+3}_{-3}$ | $22^{+3}_{-3}$ |
| $\chi^2_{red}$ | 1.12 | 1.27 | 0.96 | 1.20 |
| N stars analysed | 2022 | 212 | 820 | 569 |

Table 2.4: Structural parameters (median values of the marginalized posterior distributions) for Sextans stars in the RHB, BHB and BSs evolutionary phases, derived with the MCMC Hammer when modelling the surface number density of Sextans stellar populations as a Plummer profile; for completeness, we list also the $\chi^2_{red}$ of the best-fitting model and the number of stars analysed.

encompassing the RHB, BHB and BS sequence (see pointing #1 in Fig. 2.3). BSs were also separated into 'bright' ($g < 22.3$) and 'faint' ($g > 22.3$), as in R16. Due to the lower number statistics when dealing with the sub-sample of stars in different evolutionary phases, we did not calculate the statistical significance of iso-density contours from the distribution of the residuals between the data and the best-fitting model, as it does not reflect the precision of our decontamination method. Instead, we calculated it from the displaced pointing, making the reasonable assumption that it does not contain stars from Sextans. Since our aim here was not to determine which functional form best represents the surface relative density of the various populations, but to quantify relative differences in their spatial distribution, we fitted only a Plummer profile, in order to restrict the number of free parameters. As explained in Appendix A.2, even in the regime of low number statistics of Sextans BHB stars, the MCMC Hammer method provides relatively well-constrained position angle, ellipticity and half-light radii estimates.

Figure 2.11 shows that the best-fitting Plummer models give a satisfactory representation of the observed surface density profiles of the various subsamples. The spatial distributions of the RHB, BHB and bright and faint BSs is shown in Fig. 2.12, while the best-fitting structural parameters are summarized in Table 2.4. Keeping in mind the lower number statistics when analysing the different evolutionary phases separately, neither the surface density maps or the density profiles show evidence of tidal disturbances for any stellar evolutionary phase.

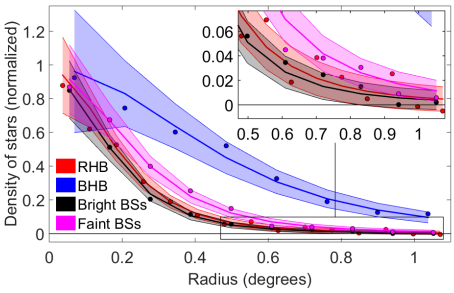


Figure 2.11: Observed surface density profiles (normalized and contamination subtracted) of RHB, BHB and BSs evolutionary phases as a function of the major axis radius (with the external parts zoomed in). The colour bands show the $1\sigma$ confidence intervals of the best-fitting Plummer profiles obtained with the MCMC Hammer. $1\sigma$ confidence intervals are computed from the fitted models assuming Poisson variances in each elliptical annulus. We do not use a logarithmic scale so as to be able to show the density fluctuations below the estimated background (negative values); otherwise plots mimic the presence of extra-tidal stars.

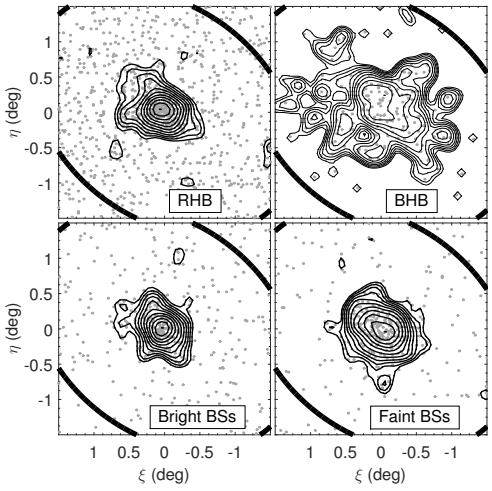


Figure 2.12: Surface density maps of Sextans RHB, BHB, bright and faint BSs, using the same decontamination techniques from Fig. 2.9, with overlaid iso-density contours with exponentially increasing values until the maximum of the measured map (lowest contour at $2\sigma$ detection from the displaced pointing, with the second one at approximately $3\sigma$ detection). The ellipse shows the contour of the King profile at its tidal radius derived in this work.

### 2.5.1 Compatibility between the spatial distributions

In order to statistically analyse the compatibility between the spatial distributions of stars in the different evolutionary phases, we obtained their radial cumulative distribution functions (CDFs). This was done using the elliptical radius derived adopting the centre, $\epsilon$ and $\theta$ obtained when fitting a King profile (see Table 2.3) and performing Kolmogorov-Smirnov (K-S) tests between all the possible pairs. This kind of analysis was already done by Lee et al. (2003) out to a major axis radius of $\sim 25$ arcmin - that is approximately the half-light radius. Our dataset covers the galaxy out to its nominal King tidal radius (120 arcmin in this work) and beyond, which can lead to different results due to possible changes in the spatial distributions beyond the half-light radius. Furthermore, the effect of contamination on the radial CDFs has been neglected until now (Lee et al. 2003, R16), while it can have a significant impact on the CDFs' shapes and therefore on the results from the K-S tests. Hence, we decided to decontaminate all radial CDFs before performing any analysis.

We used a decontamination method that removes the need for having empirical CDFs evaluated at the same radii or the loss of spatial resolution when using elliptical annuli to deal with this issue, at the same time that allows the evaluation of the K-S tests over the proper radial samples instead of their inferred CDFs. The total unnormalized CDF ($F_{tot}(r)$) of each evolutionary phase is a sum of the unnormalized CDFs of both galaxy members ($F_{gal}(r)$) and contaminants ($F_{cont}(r)$). The decontaminated CDF we are looking for is thus: $F_{gal}(r) = F_{tot}(r) - F_{cont}(r)$, in absolute counts. $F_{tot}(r)$ is directly measurable for each evolutionary phase. As for $F_{cont}(r)$, we first derive its shape - that is $F_{cont}(r)$ normalized. Assuming that the CMD of the contamination is constant across the whole field-of-view, the shape of $F_{cont}(r)$ is the same for the contaminants in all evolutionary phases and we infer it by measuring the empirical CDF of objects redder than $g-r=1$ (black vertical line in Fig. 2.5). We then calculate the number of contaminants expected in each evolutionary phase, by fitting the bilinear distribution $f_{\rm cont} = \overline{\rho}\,(1 + a\xi + b\eta)$ to the spatial distribution of these red contaminants through the MCMC Hammer. We can then calculate the ratios between our newly fitted central density ($\overline{\rho}$) and the ones previously obtained for the contamination in each evolutionary phase when we fitted their structural parameters. These ratios reflect the proportion of contaminants expected in each evolutionary phase with respect to the number of contaminants with $g-r>1$. Thus, to obtain the expected radial distribution of contaminants in an evolutionary phase, we uniformly resample the radii of the objects redder than $g-r=1$ according to its corresponding ratio, to later decontaminate the original sample by removing the stars with the closest radius to that expected for the contaminants.

| Evolutionary phase | K-S $p$-value (%) Cont. ($r < 25$') | Cont. ($r < 120$') | Decont. ($r < 120$') |
|---|---|---|---|
| RHB - Whole pop. | 1.2 | 26.4 | $6.8 \cdot 10^{-3}$ |
| BHB - Whole pop. | 21.1 | $7.4 \cdot 10^{-8}$ | $1.5 \cdot 10^{-15}$ |
| Bright BSs - Whole pop. | 1.5 | 0.019 | 1.2 |
| Faint BSs - Whole pop. | 73.4 | $1.8 \cdot 10^{-19}$ | 31.8 |
| RHB - BHB | 1.1 | $8.5 \cdot 10^{-9}$ | $8.9 \cdot 10^{-16}$ |
| Bright BSs - Faint BSs | 4.0 | $1.3 \cdot 10^{-3}$ | 2.2 |
| RHB - Bright BSs | 93.7 | 2.6 | 31.6 |
| BHB - Faint BSs | 54.0 | 0.042 | $2.6 \cdot 10^{-11}$ |
| RHB - Faint BSs | 2.5 | $3.0 \cdot 10^{-14}$ | 0.088 |
| BHB - Bright BSs | 0.81 | $8.8 \cdot 10^{-3}$ | $3.9 \cdot 10^{-11}$ |

Table 2.5: Results from the K-S tests between the radial distributions of the different evolutionary phases (all possible combinations). Column #2 is just for comparison with results from Lee et al. (2003), where contamination is included and the coverage is limited to a major axis radius of $\sim 25$ arcmin. Columns #3 and #4 show the different $p$-values obtained when contamination is included or subtracted, respectively.

The decontaminated CDFs are shown in Fig. 2.13 per evolutionary phase and for the whole Sextans population; Tab. 2.5 presents the $p$-values resulting from the K-S tests carried out over all the possible combinations of the CDFs analysed. The $p$-values are reasonably accurate for sample sizes $n_1$, $n_2$ such that $(n_1 \cdot n_2)/(n_1 + n_2) > 4$ (Smirnov 1939), with our samples satisfying by far this requirement.

When we reproduce the limitations in Lee et al. (2003) by restricting the coverage until a major axis radius of $\sim 25$ arcmin and without decontaminating the samples (left panel Fig. 2.13 and left column in Tab. 2.5), our results agree very well with theirs: with a significance level $\alpha = 0.05$, the populations that remain spatially compatible are the RHB with the bright BSs, the BHB with the faint BSs and the last two with the whole population. The results hold also when decontaminating the samples; hence the impact of the contamination is not an issue over these spatial scales.

The other panels of Fig. 2.13 (and columns in Tab. 2.5) use CDFs derived out to 120 arcmin, and illustrate the effect of neglecting contamination when comparing the CDFs over this much larger radial extent: except for the BHB,

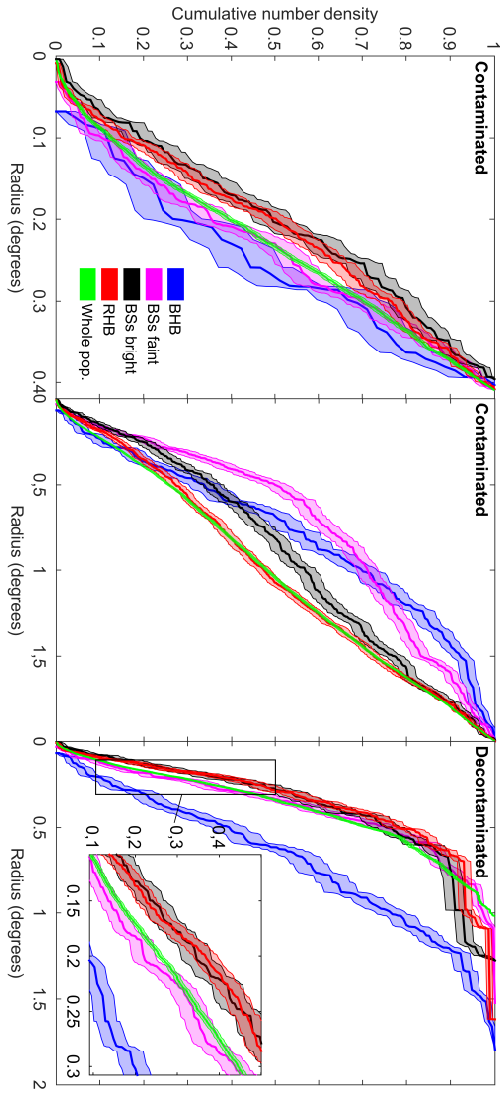


Figure 2.13: Radial CDFs of the evolutionary phases studied in Sect. 2.5 and the whole population of Sextans. The colour bands show the $1\sigma$ confidence intervals. Left: Within the major axis radius reached by Lee et al. (2003). Although this plot is contaminated, the decontaminated version is rather similar, as it does not reach the external regions of Sextans where the impact of contaminants is higher. Middle: Within the tidal radius derived in this work, with contaminants included. Right: Within the tidal radius derived in this work, with contaminants extracted and an inset magnifying the internal region where all evolutionary phases are better separated.

all CDFs are strongly affected, leading to unrealistic shapes and wrong $p$-values derived with K-S tests. When neglecting contamination, the only populations spatially compatible are the RHB stars and the overall stellar population. This is very different from the results obtained when decontaminating the CDFs: the spatial distribution of RHB stars is incompatible with the one of the overall Sextans stellar population; on the other hand, the RHB stars and bright BSs have compatible spatial distributions, and so do the faint BSs with Sextans overall stellar population. By extending the coverage from 25 to 120 arcmin, we have also discarded the possibility that BHB and faint BSs have the same spatial distribution. These results are consistent both numerically (Table 2.5) and graphically (confidence intervals in Figs. 2.11 and 2.13).

K-S tests from R16 yielded a $p$-value of 38% for BHB with BSs, and 99.8% for bright BSs with faint BSs, both incompatible with our results. It is not clear if R16 performed the K-S tests with the CDFs evaluated with different structural parameters for each evolutionary path or not. This point would invalidate the results from their K-S tests, as these evaluate the compatibility of the different spatial distributions by reducing their comparison to the radial dimension, assuming that this is the only variable reflecting the differences between the distributions. For example, two populations with very different centres or position angles that have clearly distinct spatial distributions can share the same radial CDF if this is separately evaluated for each population using their individual structural parameters. Nevertheless, even in the case that R16 used the same structural parameters for all evolutionary paths, we have proven that the effect of the contamination is not negligible at all with these large spatial coverages, therefore having an undeniable contribution to the discrepancy between our results and those in R16.

### 2.5.2 RHB and BHB

Our analysis shows that the BHB stars cover a considerably larger area than the other analysed stellar populations, with a statistically significant measurement of a half-light radius more than twice that of the RHB and much larger than the overall Sextans stellar population.

The finding of RHB stars being more centrally concentrated than BHB stars is in agreement with the early results by Bellazzini et al. (2001) based on the variation of the relative number of RHB and BHB stars in two spatial bins, as well as with Lee et al. (2003) and Okamoto et al. (2017), based on the CDFs of RHB and BHB stars and the colour distribution of HB stars as a function of major axis radius. By application of the K-S test, we find an almost zero probability of RHB stars being extracted from the same spatial distribution

as BHB stars. It appears highly likely that the differences between the RHB and BHB spatial distributions are the consequence of the age (Okamoto et al. 2017) and metallicity (Battaglia et al. 2011) gradient detected in the overall old stellar component of Sextans, similar to the case of the Sculptor dSph (Tolstoy et al. 2004, Martínez-Vázquez et al. 2015). This was previously observed by Bellazzini et al. (2001) and Lee et al. (2009), who already associated RHB and BHB stars to the more metal-rich/younger (more centrally concentrated) and more metal-poor/older (more spatially extended) populations respectively.

While the BHB spatial distribution shows much irregularities (Fig. 2.12), we have verified that this is likely due to small number statistics; indeed by extracting sub-samples of $N_{BHB}$ stars from the more populated BSs and RHB populations, their regular spatial distribution would artificially appear very distorted.

### 2.5.3 Candidate blue straggler stars

From their analysis of Sextans's central regions, Lee et al. (2003) noticed that, when separating candidate BSs into a bright and faint sample through a magnitude cut, the former had a more centrally concentrated spatial distribution than the latter. The probability of being extracted from a similar spatial distribution was low, however this latter point was questioned by R16.

In our analysis we confirm the early findings by Lee et al. (2003) that bright BSs and faint BSs have a low probability of being extracted from a similar spatial distribution ($p$-value = 2.2% from the K-S test), and we derive a half-light radius of $16^{+3}_{-3}$ and $22^{+3}_{-3}$ arcmin for bright and faint BSs, respectively.

In the case of globular clusters a possible interpretation for this feature would be that BSs created via stellar collisions (Hills & Day 1976) mainly correspond to the bright ones, and those evolving from primordial binaries to the faint ones (McCrea 1964). One reason for this is that collisions are more probable where the stellar density is large, such as in the inner regions of dense clusters, where mass segregation is a dominant process; hence collisions of more massive stars would produce bluer and brighter BSs (Bailyn & Pinsonneault 1995; Bailyn 1995). However, as argued by Lee et al. (2003), in dSph galaxies the central densities are so low that BSs created via stellar collisions are highly unlikely (Mapelli et al. 2007; Momany et al. 2007). An intriguing hypothesis was proposed by Kleyna et al. (2004), who argued that "if a significant fraction of Sextans BSs were formed in a star cluster which subsequently disrupted near the centre of the galaxy, mass segregation within the cluster would ensure that the most massive (brighter) BSs would be the last to be tidally removed from the cluster and hence would have a more concentrated spatial distribution".

Does the different spatial distribution of bright and faint Sextans BSs need to be explained by invoking the disruption of a globular cluster that spiralled in the central regions? Or can they be explained as the result of mass transfer from primordial binaries?

In our analysis, the comparison of the cumulative CDFs shows that the bright BSs have a spatial distribution compatible with being extracted from a similar one than Sextans' RHB stars, whilst the faint ones are compatible with the overall Sextans stellar population. If Sextans BSs are the result of mass transfer from primordial binaries, one would expect them to show a similar spatial distribution as the overall stellar population, and to possibly reflect the age and metallicity gradient traced by other stellar populations if one is able to associate parts of the BS sequence to stellar populations in other evolutionary phases.

Lee et al. (2003) (see their Fig. 19) showed that 2-6 Gyr old isochrones encompass the range of magnitudes and colours of Sextans BS sequence, with the bluer and brighter BSs being reproduced by the youngest isochrones, without much contamination from the older ones; on the other hand, over the CMD selection of faint BSs, the isochrones overlap significantly in magnitude and colour. While in the case of BSs the age range of the isochrones is not representative of the stars actual age, this shows that the bluer and brighter BSs (corresponding to the bright BS selection) can be thought of as slightly more massive on average than the fainter and redder ones (i.e. the faint BS selection); and that the faint selection hosts of a mix of the stellar population that gave rise to the BSs, rather than only the less massive end. This could explain why the spatial distribution of the bright BSs is compatible with the RHB distribution, while the faint BSs appear to trace Sextans overall stellar population.

Overall, while we cannot discard the possibility that some of Sextans BSs come from a disrupted stellar cluster, the above results do not make this hypothesis compelling to explain the bulk of Sextans BSs.

Another possibility concerning the nature of Sextans BSs is that they are actual main-sequence stars of intermediate-age ($\sim$ 2-6 Gyr old). If this were the case, as a consequence of the age gradient detected in Sextans, one would expect these stars to be the most spatially concentrated ones, as they would be the youngest ones of the stellar populations analysed. Our analysis shows that this is not the case, hence we deem it unlikely that Sextans BSs are genuine intermediate-age ($\sim$ 2-6 Gyr old) main-sequence stars.

## 2.6 Spectroscopic analysis

We used our revised structural parameters of the Sextans dSph to update the membership probabilities of the spectroscopic samples by Walker et al. (2009b) and Battaglia et al. (2011) (hereafter W09 and B11), obtained with the Michigan-MIKE Fiber System (MMFS) and the Fibre Large Array Multi Element Spectrograph (FLAMES) respectively.

To calculate those probabilities, we followed the "expectation maximization" (EM) technique outlined in W09. If $P_i$ denotes the membership of an object, with 1 for members and 0 for nonmembers, the likelihood of observing the $N$ objects whose measurements $X_i$ follow the given probability distribution functions $p_{mem}(x)$ and $p_{non}(x)$, of members and nonmembers respectively, is then:

$$L(\zeta_{mem}, \zeta_{non}) = \prod_{i=1}^{N} [p_{mem}(X_i)p(a_i)]^{P_i} \, [p_{non}(X_i)[1 - p(a_i)]]^{1-P_i}, \tag{2.7}$$

where $(\zeta_{mem}, \zeta_{non})$ are the parameter sets that characterize the distributions of member and nonmember populations respectively, and $p(a)$ is an optional independent prior which could model the probability of membership according to, for example, the projected distance from the galactic centre. Although we do not know the real membership (0 or 1) of an object, we can make use of the membership probability:

$$P_i = \frac{p_{mem}(X_i)p(a_i)}{p_{mem}(X_i)p(a_i) + p_{non}(X_i)[1 - p(a_i)]} \tag{2.8}$$

Finding the parameter sets $(\zeta_{mem}, \zeta_{non})$ which maximize the likelihood in Eq. 2.7, we can obtain the membership probabilities of the spectroscopic samples through Eq. 2.8. These parameter sets are, for example, the mean and variance in the case of a Gaussian distribution.

For the catalogue of W09 the measurements $X_i$ we used are the heliocentric velocity and the pseudoequivalent width of the Mg-triplet absorption feature, while for that of B11 we used the heliocentric velocity, the equivalent width of the Mg I line at 8806.8Å and the metallicity ([Fe/H]). Regarding the measurements $a_i$ we used the projected distance from the galactic centre for both catalogues. The expressions of $p_{mem}(x)$ and $p_{non}(x)$ are the same used by W09 when analysing their dataset. With that of B11, as in the original article no probability distribution functions were used to separate members from nonmembers, we assumed Gaussian distributions in both $p_{mem}(x)$ and $p_{non}(x)$ for metallicity and Mg I line measurements, and the expressions of W09 for the velocity.

In addition, we also devised some modifications to the EM algorithm of W09:

- In W09 the likelihood was maximized through an iterative process in which the membership probabilities in Eq. 2.7 were substituted by the results from Eq. 2.8, and the parameters resulting from maximizing that likelihood were substituted back into Eq. 2.8 to update the membership probabilities. This recursive process was continued until convergence. Here, instead of iteratively calculating the likelihood and the membership probabilities separately, we decided to insert Eq. 2.8 into Eq. 2.7 to maximize this expression at once through the MCMC Hammer, as we did in Sect. 2.3.

- Regarding the parameter sets $\zeta_{mem}$, they were considered as constant across the whole field-of-view. Nonetheless we know that in dSphs, and in particular in Sextans, some of them can present radial gradients (e.g. in metallicity or velocity dispersion). Thus, we separately run the MCMC Hammer over elliptical annuli drawn from the King profile fitted in Sect. 2.3, in order to allow the different parameters to radially vary. Nevertheless, as it is reasonable to assume that parameter sets $\zeta_{non}$ do not vary along the projected major axis radius of Sextans, we first fitted them by applying the MCMC Hammer over the whole dataset, to keep $\zeta_{non}$ fixed when fitting $\zeta_{mem}$ over the elliptical annuli.

- While W09 estimate $p(a)$ via monotonic regression, we preferred to derive it from the mean surface density profile fitted in Sect. 2.3. We consider it gives us a better description of how the membership probability decays as a function of radius while at the same time not depending on a unique formula for the adopted surface density profile.

Finally, before applying the EM algorithm, we had to ensure a high reliability for the FLAMES dataset by excluding the same stars which did not satisfy the requirements established in B11. Once these stars have been excluded, we have a total of 141 overlapping stars between the W09 and B11 catalogues, with their positions agreeing within $\sim 1$ arcsec, for which we provide membership probabilities calculated separately from each catalogue. Overall, the combination of W09 and B11 measurements results into 1595 entries, from which the EM algorithm detected a total of 629 members by summing all their membership probabilities. In Fig. 2.14, the left panel displays the spatial distribution of the membership probabilities from the cross-correlated catalogue, while the right panel shows the differences with respect to their previously published

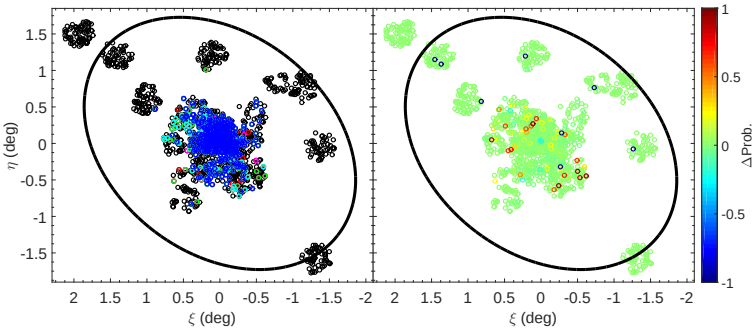


Figure 2.14: Location of stars along the line-of-sight to Sextans from the spectroscopic samples of W09 and B11. Left: Colour-coded using the updated membership probabilities from this work. The colour-coding is as in W09, with black, red, magenta, green, cyan and blue markers denoting $P_i \geq 0.00$, $> 0.01$, $> 0.50$, $> 0.68$, $> 0.95$, $> 0.99$ respectively. Right: Colour-coded using the difference in the membership probabilities here derived and in the previous works ($\Delta$Prob. $= P_{new} - P_{prev}$). Black ellipses show the nominal King tidal radius with parameters from this work. For these plots, in the case of the overlapping stars we opt to use the probabilities derived from the dataset of B11, as when evaluating their probabilities we can rely on three spectroscopic sources of information ($v_{hel}$, EW Mg and [Fe/H]), rather than two as in the case of the W09 dataset ($v_{hel}$ and $\Sigma$Mg). Further, we consider that the metallicity is a more reliable discriminant compared to just the Mg-triplet absorption feature from W09, as it depends on three parameters measured by B11: EW Mg of the star and apparent magnitudes in V band of both the star and the horizontal branch of the galaxy.

values. The agreement with the previous determinations is good; the few discrepant values are likely due to the fact that we are allowing for radial gradients of the properties and that we adopt the average density profile as a prior on membership probability as a function of radius.

Table 2.6 shows a sample from the cross-correlated spectroscopic catalogue generated, which, like the photometric one, is also supplied online. For each object the catalogue contains the celestial coordinates, the heliocentric velocities, the equivalent width of the Mg I line, the metallicity, the pseudo-equivalent width of the Mg-triplet absorption feature, the probabilities assigned in the original articles and the probabilities derived in this work. With respect to the dataset of B11, the error in the equivalent width of the integrated fit of the Mg I line was updated from $\sigma_{EW}$=2.8/(S/N) to $\sigma_{EW}$=3.6/(S/N) (Battaglia & Starkenburg 2012), while the metallicity and its error were derived as in B11, from the near-infrared Ca II triplet (CaT) region adopting the calibration of Starkenburg et al. (2010). As B11 did not assign proper membership probabilities, just member/nonmember designation, we associated their members and nonmembers with membership probabilities of 1 and 0 respectively.

| ID | Coordinates | | Dataset from Battaglia et al. (2011) | | | | | Dataset from Walker et al. (2009b) | | | | |
|---|---|---|---|---|---|---|---|---|---|---|---|---|
| | $\alpha_{2000}$ (hh:mm:ss) | $\delta_{2000}$ (dd:mm:ss) | $v_{hel}$ (km s$^{-1}$) | EW Mg (Å) | [Fe/H] (dex) | $P_{prev}$ | $P_{new}$ | $v_{hel}$ (km s$^{-1}$) | $\Sigma$Mg (Å) | $P_{prev}$ | $P_{new}$ |
| 1 | 10:11:35.40 | -01:58:13.7 | 214.23±1.11 | 0.007±0.151 | $-2.42^{+0.14}_{-0.15}$ | 1 | 0.999 | 217.4±1.4 | 0.42±0.05 | 0.985 | 0.995 |
| 2 | 10:12:43.34 | -01:32:05.2 | 56.51±1.40 | 1.192±0.114 | $-1.18^{+0.08}_{-0.08}$ | 0 | 0.000 | 56.3±0.7 | 0.93±0.02 | 0.000 | 0.000 |
| 3 | 10:12:32.66 | -02:00:05.2 | 220.25±2.56 | -0.526±0.233 | $-1.75^{+0.20}_{-0.21}$ | 1 | 0.976 | 222.7±2.5 | 0.80±0.08 | 0.002 | 0.545 |
| 4 | 10:12:53.46 | -01:15:16.5 | 230.86±1.87 | 0.184±0.217 | $-2.86^{+0.27}_{-0.36}$ | 1 | 0.999 | 233.5±2.0 | 0.02±0.07 | 0.738 | 0.999 |
| 5 | 10:13:00.59 | -01:25:47.0 | 111.31±0.68 | 0.448±0.057 | $-1.94^{+0.04}_{-0.05}$ | 0 | 0.000 | 109.7±0.7 | 0.88±0.01 | 0.000 | 0.000 |
| 6 | 10:13:01.59 | -01:21:49.9 | -18.28±2.87 | 0.842±0.180 | $-1.36^{+0.14}_{-0.15}$ | 0 | 0.000 | -18.0±0.7 | 0.99±0.04 | 0.000 | 0.000 |
| ... | ... | ... | ... | ... | ... | ... | ... | ... | ... | ... | ... |

Table 2.6: Sample from the combined W09 and B11 spectroscopic catalogues with updated probabilities of membership. The whole spectroscopic catalogue is available online. $P_{prev}$ is the probability assigned in the original article, while $P_{new}$ is the probability derived in this work. Columns #3−#7 correspond to the dataset of B11 (heliocentric velocity, equivalent width of the Mg I line, metallicity, $P_{prev}$, $P_{new}$), while #8−#11 to the one of W09 (heliocentric velocity, pseudo-equivalent width of the Mg-triplet absorption feature, $P_{prev}$, $P_{new}$).

## 2.7 Summary and conclusions

We present results from CTIO/DECam deep $g-$ and $r-$band photometry of the Sextans dSph out to a radius of $\sim 4$ deg, covering approximately 20 deg$^2$ and reaching $\sim 2$ magnitudes below the oldest main-sequence turn-off. The photometric catalogue of point-like sources is made publicly available.

We updated the structural parameters of the galaxy (Table 2.3) by fitting different surface density profiles through a Bayesian MCMC sampling of the likelihood evaluated at each star's location. We find overall agreement with the structural analysis of IH95, but with Sextans having a smaller half-light radius than previously reported by IH95 and R16. Likewise, through the posterior Bayes factor we established that the best-fitting King profile and corresponding structural parameters from this work are strongly favoured over the best-fitting models by IH95 and R16. In addition, we updated the apparent, absolute magnitude and central surface brightness in V-band: $V = 10.73^{+0.06}_{-0.05}$ mag, $M_V = -8.94^{+0.11}_{-0.09}$ mag and $\mu_V = 27.25^{+0.06}_{-0.05}$ mag/arcsec$^2$ respectively (already corrected for Galactic extinction), which are compatible with the values from Irwin & Hatzidimitriou (1995) but with considerably reduced errors.

We decontaminated two-dimensional surface density maps of Sextans overall stellar population by making use of an improved version of the McMonigal et al. (2014) matched-filter method. Sextans displays a fairly regular distribution with no significant distortions down to a surface brightness level of $\sim 31.8$ mag/arcsec$^2$ in V-band, unlike the surface density map generated by Roderick et al. (2016a). By studying the 2D distribution of residuals with respect to the fitted surface density axisymmetric models, we have detected several over-dense and under-dense clumps at the $2\sigma$ and $3\sigma$ levels from which we identified an overdensity in the galactic centre that might correspond to the cold substructure/s detected by Kleyna et al. (2004) and Battaglia et al. (2011). The origin of the under-dense clumps is still unclear. Stars forming part of these over- and under-dense clumps are therefore of particular interest for future spectroscopic studies of Sextans, in particular those stars belonging to the overdensity in its centre that might correspond to the cold substructure/s. We defer to Chapter 3 an in-depth analysis of the possible presence of sub-structures in Sextans' inner regions.

For the first time, we carried out a quantitative determination of the structural properties and number density profiles of stars in different evolutionary phases in Sextans, that is RHB, BHB and BS stars. No significant distortions are found for any of these populations. RHB and BHB stars have clearly distinct spatial distributions, with the RHB stars exhibiting a much smaller 2D half-light radius than the BHB ones (17 vs. 42 arcmin, respectively) and

slightly smaller than the overall Sextans stellar population (22 arcmin). This is consistent with the age and metallicity gradient found by Okamoto et al. (2017) and Battaglia et al. (2011), respectively, and puts on a quantitative basis the more qualitative type of findings by Bellazzini et al. (2001), Lee et al. (2003, 2009), Roderick et al. (2016a) and Okamoto et al. (2017). With regard to BSs, we confirmed that the bright BSs ($g < 22.3$) are less spatially extended than the faint ($g > 22.3$) ones. The compatibility of the spatial distribution of the bright BSs with the RHB stars, and of the faint BSs with the whole population, appears compatible with the hypothesis that the bulk of Sextans BSs evolved from mass transfer of primordial binaries.

Finally, we used the revised Sextans structural properties from the analysis of our photometric dataset to update the membership probabilities of stars in the spectroscopic catalogues by Battaglia et al. (2011) and Walker et al. (2009b), following the decontamination methodology of the latter in an improved form. This catalogue is also made publicly available in order to facilitate subsequent studies of the internal properties of Sextans.

# 3

# Appearances can be deceiving: clear signs of accretion in the seemingly ordinary Sextans dSph

**L. Cicuéndez and G. Battaglia**

Published as MNRAS, 2018, 480, 251

**ABSTRACT**

We report the discovery of clear observational signs of past accretion/merger events in one of the Milky Way satellite galaxies, the Sextans dwarf spheroidal (dSph). These were uncovered in the spatial distribution, internal kinematics and metallicity properties of Sextans stars using literature CTIO/DECam photometric and Magellan/MMFS spectroscopic catalogues. We find the spatial distribution of stars to vary as a function of the colour/metallicity, being rather regular and round for the blue (metal-poor) red giant branch and main-sequence turn-off stars but much more elliptical and irregularly shaped for the red (metal-rich) ones, with a distinct "shell-like" overdensity in the northeast side. We also detect kinematic anomalies, in the form of a "ring-like" feature with a considerably larger systemic line-of-sight velocity and lower metallicity than the rest of stars; even the photometrically selected component with a regular looking spatial distribution displays complex kinematics. With a stellar mass of just $\sim 5 \times 10^5 M_\odot$, Sextans becomes the smallest galaxy presenting clear observational signs of accretion to date.

## 3.1 Introduction

According to the Λ-Cold Dark Matter (ΛCDM) cosmological framework of structure formation, Milky Way (MW)-like and massive galaxies are formed in a hierarchical process through mergers and accretion of smaller systems (White & Rees 1978). Nevertheless, mergers are also expected between

low mass haloes (e.g. Fakhouri et al. 2010). Deason et al. (2014) showed, using dissipationless cosmological zoom-in simulations, that very few isolated dwarf galaxies in the Local Group (LG) could have escaped from a major merger in their formation history. More recently, also Benítez-Llambay et al. (2016), using cosmological zoom-in simulations of the LG formation, argued that mergers played a significant role in the formation of at least some isolated dwarfs. Regarding satellite dwarf galaxies, these are half as likely to have experienced a major merger as compared to isolated dwarfs of similar mass (Deason et al. 2014).

From an observational perspective, different substructures have been discovered in the kinematics and density distribution of the stellar component of several LG dwarf galaxies, probably resulting from the disruption of smaller accreted dwarfs. Among the galaxies with clear observational evidence of external accretion, the smallest one up to date is And II ($\sim 10^7$ solar masses in stars), in which Amorisco et al. (2014) detected the presence of a stellar stream. Subsequently, several studies modeled the galaxy as the result of a merger between two dwarfs (see e.g. Ebrová & Łokas 2015; Fouquet et al. 2017), reproducing also And II observed prolate rotation (Ho et al. 2012). Recently, prolate rotation was also detected in the Phoenix transition-type dwarf; this kinematic feature, combined with the peculiar spatial distribution of the young stars, was interpreted as a sign of an accretion or merger event (Kacharov et al. 2017). Another complex system is the Fornax dSph: Battaglia et al. (2006) found a double peaked line-of-sight (LOS) velocity distribution for the metal-poor stars of this galaxy, which, together with the asymmetric and more centrally concentrated distribution of its young stars, could have resulted from the recent accretion of external material after the merger with another dwarf, consistent with previous evidence of a shell-like feature (Coleman et al. 2004) and the scenario later proposed by Amorisco & Evans (2012) where Fornax formed from a late merger of a bound pair.

Other examples of substructures not necessarily formed by accretion of smaller galactic systems are also present among the dwarf galaxies satellites of the Milky Way. For example, Ursa Minor shows a secondary peak in its stellar density (Bellazzini et al. 2002), where Kleyna et al. (2003) then detected a cold kinematic signature also confirmed by Pace et al. (2014). In both these latter works it was argued that this cold kinematic sub-structure would probably correspond to a stellar object that survived to multiple orbits within the gravitational potential of the dwarf galaxy thanks to, either having its own dark matter halo protecting it, or due to Ursa Minor dark matter halo being cored instead of cuspy. The Sculptor dwarf spheroidal galaxy also presents cold kinematic substructures (see Chapter 4 in Battaglia 2007). As for the Sextans

dSph, Kleyna et al. (2004), Walker et al. (2006) and Battaglia et al. (2011) (hereafter K04, W06 and B11 respectively) identified localized cold kinematic substructures in the inner regions of this system; thanks to the availability of metallicity estimates for the individual stars, B11 traced the signature back as belonging to Sextans' metal-poor component.

In this chapter we report the detection of clear observational signs of accretion in the Sextans dSph, which impact on both the spatial distribution and internal kinematics of the dwarf galaxy. This chapter is structured as follows: in Sect. 3.2 we use the CTIO/DECam photometric catalogue from Chapter 2 and show that the spatial distribution of blue red giant branch (bRGB) and main-sequence turn-off (MSTO) stars is remarkably different from the one of red RGB (rRGB) and MSTO stars; in Sect. 3.3 we re-analyze the MMFS spectroscopic sample from Walker et al. (2009b) (hereafter W09) with the membership probabilities derived in Sect. 2.6 and detect the presence of a "ring-like" feature with a distinct velocity from the rest of Sextans's population and having a lower relative metallicity. Finally, we summarize the results and discuss the possible origins of the detected features in Sect. 3.4.

## 3.2 Anomalous differences in the spatial distribution of blue and red RGB stars

The CTIO/DECam photometric dataset from Chapter 2 published in Cicuéndez et al. (2018) consists of a catalogue of point-like sources with SDSS $g-$ and $r-$ magnitudes covering nearly 20 deg$^2$ around the Sextans dSph and reaching down to $\sim 2$ mag below Sextans' oldest main-sequence turn-off.

Here we use this dataset to analyze the spatial distribution of Sextans stars as a function of their colour. The majority of the following analysis is based on sources brighter than $g = 23$, because this guarantees that the photometric catalogue is unaffected by artificial overdensities appearing in the outer parts of the DECam pointings (see Sect. 2.2); at the distance of Sextans, this magnitude cut essentially corresponds to the base of the RGB. We will however also use stars in the range $23 < g < 24$, that is on the MSTO, down to the $S/N \sim 10$ level of the shallowest pointing in the mosaic, to verify that the results hold also for the stars in this evolutionary phase.

The colour-magnitude diagram (CMD) selection regions adopted for the analysis are displayed in Fig. 3.1. To define the CMD masks we first selected stars within a major axis distance of half a degree, in order to avoid most of the contaminants, and then retained only point-like sources compatible with being MSTO, sub-giants or RGB stars. The resulting CMD was then binned

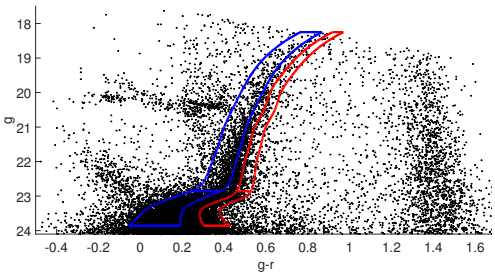


Figure 3.1: CMD from CTIO/DECam dataset of Chapter 2 for stars with major axis distance less than 0.5 deg from Sextans centre. Blue and red lines show the selection masks used to select blue and red RGB (and MSTO) stars, respectively. The horizontal line at $g = 23$ separates the RGB from the MSTO selection (see main text).

along the magnitude axis ($g$) and the 85th and 50th percentiles of the colour distribution in a given magnitude bin were evaluated; finally, these selection limits were cubic spline interpolated at each data point of the whole dataset, so that each object could be then easily assigned either to the blue or to the red selection. We used the 85th percentile of the colour distribution to define the "blue" (inner) limit of the red selection box, and the 50th percentile for the "red" limit of the blue selection, while their outer limits are defined by these ones plus one and minus two times the median colour uncertainties at each magnitude bin, respectively. Note that each selection box likely contains a fraction of stars that originally belong to the other one due to the colour uncertainties, which are typically larger than the gap between both selection boxes.

Figures 3.2 and 3.3 show the spatial distribution of bRGB and rRGB point-like sources. These have been decontaminated following two different methods: a matched-filter analysis as in Sect. 2.4 (see iso-density contours in the top-panels) and a decontamination method acting on the individual point-sources without spatial binning (bottom panels), described in Appendix B.1. One can appreciate a rather regular and almost round spatial distribution of the bRGB stars, while the spatial distribution of rRGB stars is clearly more elliptical and with an irregular shape, with the presence of an overdensity of stars in the northeast side, reminiscent of the shells observed in much larger galaxies, and the centre of the bulk of the population slightly displaced southwest with respect to the one of the bRGB stars. We note that we have explored different color cuts and converged on the one that best highlights the differences in the spatial distribution of bRGB and rRGB stars, while not compromising number statistics.

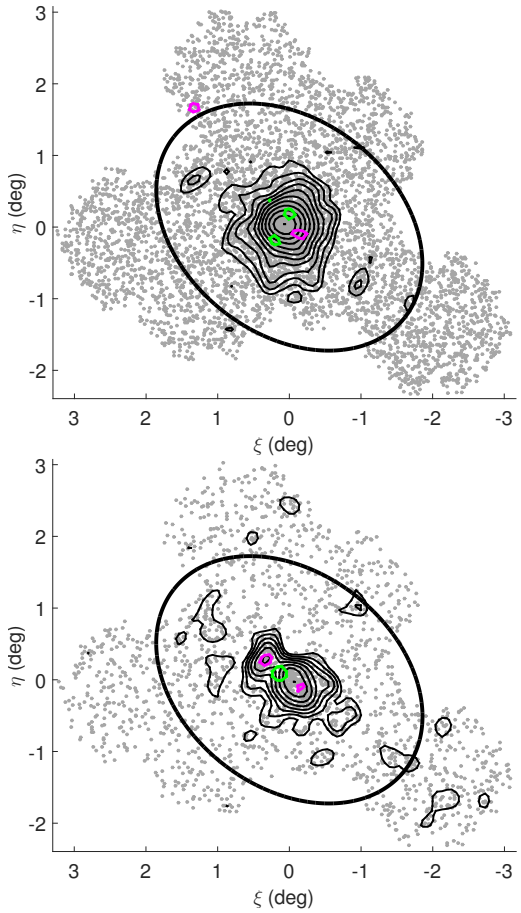


Figure 3.2: Spatial distribution of blue (top) and red (bottom) RGB stars (see CMD masks in Fig. 3.1), with overlaid iso-density contours from the matched-filtering method denoting exponentially increasing values of stellar number density, with the outermost contours tracing the $3\sigma$ detection. Green and magenta contours respectively trace the $3\sigma$ detections above and below the mean of the residuals between the decontaminated matched-filtered maps of the corresponding deep CMD selection boxes (MSTO) and the mean of their best-fitting axisymmetric models (King, Sersic, Plummer and exponential profiles). Black ellipses show the nominal King tidal radius derived in Sect. 2.3.

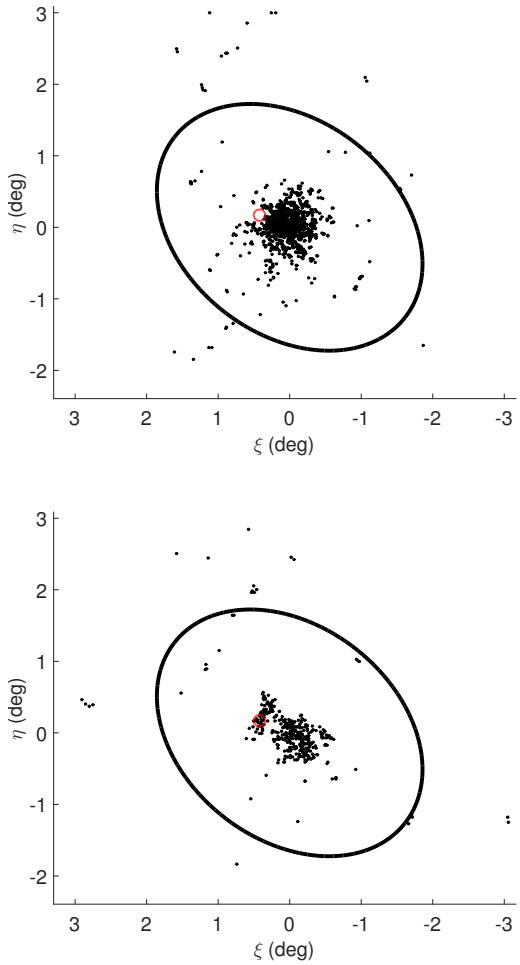


Figure 3.3: Spatial distribution of blue (top) and red (bottom) RGB stars (see CMD masks in Fig. 3.1), after decontaminating the stellar locations with the method explained in Appendix B.1. Black ellipses show the nominal King tidal radius derived in Sect. 2.3 and red circles delimit the region centered on (0.42,0.17) deg where a considerably higher concentration of redder stars was detected (see also Fig. 3.5).

Being the spatial distribution of the bRGB fairly axisymmetric, we derived its structural parameters following the method from Sect. 2.3 based on Richardson et al. (2011), which works by evaluating at the locations of the individual stars a likelihood expression which depends on the surface density profile to be fitted as well as on the ellipticity, position angle, etc. As in Sect. 2.3, in this expression we also included the surface density of contaminants by modelling it with a spatial bilinear distribution (i.e. a plane) to account for the expected spatial gradient in the density of MW contaminants. The most probable value of each structural parameter is then evaluated by sampling this likelihood expression through a Markov chain Monte Carlo (MCMC) sampler, where in our case we used "The MCMC Hammer" (Foreman-Mackey et al. 2013)[1].

The visual impression is confirmed by this quantitative analysis (see Tab. 3.1): the ellipticity of the bRGB is 0.05, to be compared to the value of 0.27 of Sextans overall stellar population down to the same magnitude limit; the position angle of this blue RGB population is ill-determined, due the round shape; there is also a hint of a smaller half-light radius of the bRGB stars with respect to the overall Sextans stellar population, with the former having $\sim 19$ arcmin and the latter $\sim 22$ arcmin (see Table 2.3). We checked that the half-light radius of the bRGB population becomes even smaller if adopting a bluer selection, reaching down to values as low as $\sim 17$ arcmin; this can probably be understood by the bRGB box containing stars originally belonging to the rRGB populations, scattered in the blue box by photometric errors in the colour, if the rRGB population has a larger half-light radius than the bRGB one (see below).

Even though at magnitudes fainter than $g = 23$ artificial artifacts starts appearing in the outer regions of the pointings, we repeated the analysis on the point-sources falling within the blue and red selection boxes in the magnitude range $23 < g < 24$ to test whether the features detected are preserved at fainter magnitudes, below the MSTO. In this case, we also derived the structural parameters of the red population, which should be taken with a grain of salt due to the departures from axisymmetry in the spatial distribution of these stars. The results are summarized in Table 3.1: the round shape of the blue population and much flatter distribution of the red one are confirmed, as it is the difference in the centre coordinates; furthermore, the red component is significantly less concentrated than the blue one, as reflected in the value of the half-light radius. Since our aim here was not to determine which functional form

[1] As in Sect. 2.3, the code we used (`https://github.com/grinsted/gwmcmc`) was developed at Centre for Ice and Climate (Niels Bohr Institute), for which we defined a total of 80 walkers, each of them doing approximately $10^4$ steps.

| Parameter | Blue RGB | Blue MSTO | Red MSTO |
|---|---|---|---|
| $\alpha_{2000}$ ($^{\rm o}$) | $153.282^{+0.008}_{-0.008}$ | $153.285^{+0.004}_{-0.004}$ | $153.25^{+0.02}_{-0.02}$ |
| $\delta_{2000}$ ($^{\rm o}$) | $-1.613^{+0.008}_{-0.009}$ | $-1.619^{+0.004}_{-0.004}$ | $-1.588^{+0.009}_{-0.009}$ |
| Ellipticity | $0.05^{+0.05}_{-0.04}$ | $0.05^{+0.03}_{-0.03}$ | $0.44^{+0.04}_{-0.04}$ |
| Pos. angle ($^\circ$) | $20^{+40}_{-30}$ | $40^{+20}_{-20}$ | $59^{+3}_{-3}$ |
| $r_e$ ($'$) | $11.6^{+0.6}_{-0.6}$ | $10.7^{+0.3}_{-0.3}$ | $13.8^{+0.6}_{-0.6}$ |
| 2D $r_h$ ($'$) | $19^{+1}_{-1}$ | $18.0^{+0.4}_{-0.4}$ | $23^{+1}_{-1}$ |

Table 3.1: Structural parameters (median values of the marginalized posterior distributions) for Sextans stars falling in three of the selection boxes plotted in Fig. 3.1, derived with the MCMC Hammer when modelling the surface number density as an exponential profile. Regarding the 2D half-light radii $r_h$, they were derived from the exponential ones $r_e$ using $r_h = 1.678\, r_e$ (Wolf et al. 2010). If we were to fit a Plummer profile, the only statistical difference would be in all the values of the 2D $r_h$ being $\sim 1-2$ arcmin larger.

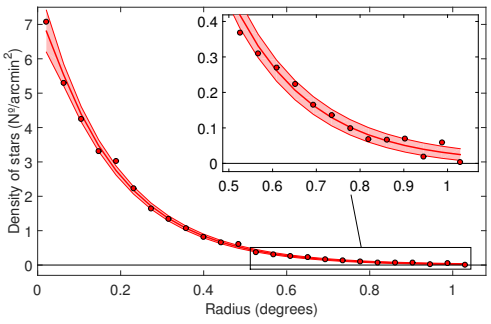


Figure 3.4: Contamination subtracted surface number density profile of the blue MSTO stars as a function of the major axis radius (with the external parts zoomed in), overlaid onto the $1\sigma$ confidence interval (red band) of the best-fitting exponential profile obtained with the MCMC Hammer. The $1\sigma$ confidence interval is computed from the best-fitting model assuming Poisson variances in each elliptical annulus.

best represents the surface number density of the stars in the different CMD selections, but to quantify relative differences in their spatial distribution, we report the results only for an exponential profile, in order to restrict the number of free parameters. Figure 3.4 shows that the best-fitting exponential model gives a satisfactory representation of the observed surface density profile of the axisymmetric blue MSTO, even despite the artificial artifacts in the outer regions of the pointings. We also tested whether the "shell-like" overdensity of rRGB stars in the northeast part of the field-of-view continues being present also in the fainter selection; to this end, we studied the distribution of residuals between the decontaminated matched-filter density map of the red stars from the deeper, MSTO selection and the best-fitting axisymmetric models: the $3\sigma$ contours of over- and under-densities are plotted in Fig. 3.2 and show that indeed the $3\sigma$ over- and underdensities detected in the MSTO red selection coincide with the "shell-like" feature in the distribution of rRGB stars and the gap between such feature and the bulk of the rRGB population.

Using theoretical isochrones from the canonical models of the BaSTI library[2] we constrained the mean metallicity of the blue and red selections to be within $-3.6 < [\mathrm{Fe/H}] < -2.6$ and $-2.6 < [\mathrm{Fe/H}] < -1.6$, respectively. These two intervals are compatible with the two metallicity peaks found by B11 in the spectroscopic metallicity distribution function of the RGB stars, which the authors fitted with a sum of two Gaussians of means $[\mathrm{Fe/H}] = -2.7$ and $[\mathrm{Fe/H}] = -2.0$. We also checked that these values are broadly in agreement with the spectroscopic metallicities measured by B11 for the stars falling in each of our RGB CMD selection boxes: the blue and red selections are indeed associated with B11 metal-poor and metal rich populations respectively and they are incompatible with being extracted from a common parent distribution in metallicity (p-value $< 0.03$ from a Kolmogorov-Smirnov test).

We conclude then that stars falling within the blue selection, which display a round and regular spatial distribution, encompass the metal-poor part of Sextans's stellar population, while those in the red selection, which have an asymmetric, clumpy and fairly flat distribution, encompass the metal-rich population of Sextans. As we will see in Sect. 3.3, anomalous properties can also be appreciated in the internal kinematics of Sextans's stellar component.

Here we notice that the presence of these stellar populations with distinctly different spatial distributions appears to be the culprit for the different structural parameters obtained in Chapter 2 as a function of magnitude when analyzing Sextans overall stellar population, where a deeper magnitude cut ($(g, r) = (24.9, 24.9)$, Table A.3) was yielding a rounder and more concentrated

[2] `http://albione.oa-teramo.inaf.it`

spatial distribution than when adopting a brighter cut ($(g, r) = (23.0, 23.0)$, Table 2.3). In that work the cause for this behavior could not be traced back to any obvious difference in the stellar population mix as a function of magnitude. Since at magnitudes fainter than $g = 23$ the outer parts of the pointings of the DECam dataset from Chapter 2 suffered from artificial overdensities caused by the morphological misclassification between extended and point-like objects due to out-of-focus regions, and fainter than $g \sim 24$ small differences in depth between the pointings start appearing, we maintained a cautious approach and based on the structural parameters derived from the brighter portion of the photometric catalogue. Thanks to the analysis in this chapter, this behaviour can now be understood as due to a variable proportion of blue versus red stars as a function of magnitude, which we find to be higher at the deepest magnitudes. Therefore, in practice, the structural parameters derived for Sextans *are* dependent on the magnitude cut adopted, due to the varying proportion of blue/red stars having distinct spatial distributions. Strictly speaking, when regarding Sextans as a whole, the structural parameters derived from the deepest catalogue (Table A.3), which encompass more of Sextans's stars, should be more appropriate.

Finally, we note that the over- and under- densities in the middle panel of Fig. 2.9 in Sextans's overall stellar population can be confirmed as real features and understood as a consequence of the inadequacy of one single axisymmetric model in capturing the complexity of the underlying stellar population.

We also note that in the region marked with a red circle in the bottom panels of Fig. 3.3 the distribution of red stars is particularly clumpy, and coincides with an apparent decrease in the number of stars plotted in the decontaminated blue RGB map. No clear overdensity, such as a stellar cluster, is visible in the DECam images at that location. The CMD of this region is particularly red with respect to the CMD of the remaining stars at the same elliptical radius (Fig. 3.5), and comparison with BaSTI isochrones suggests a metallicity [Fe/H]$= -1.6$, that is at the high metallicity end of what found for the red RGB and MSTO selection; this is perhaps signaling that star formation in that region occurred more recently than in the surroundings and could give hints as to the details of the process that caused the shell-like feature and asymmetric distribution of the red stars.

### 3.3 A "ring-like" kinematic substructure

The W09 spectroscopic dataset consists of LOS heliocentric velocities and pseudo-equivalent widths of the Mg-triplet absorption feature ($\Sigma$Mg) obtained with the Michigan/MIKE Fiber System at the Magellan 6.5m Clay Telescope;

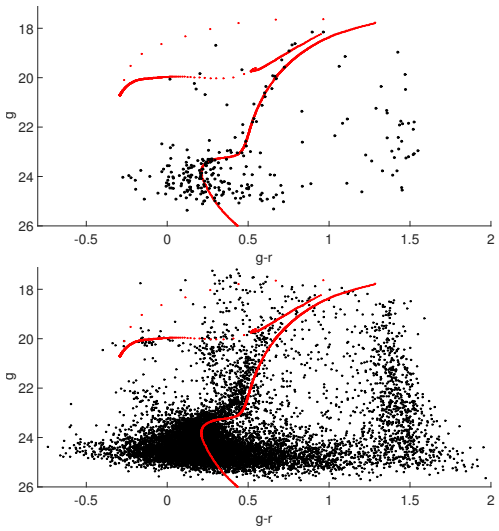


Figure 3.5: CMDs of the detected red blob at position (0.42,0.17) deg in Fig. 3.3 (top) and of the rest of stars at the same major axis distance (bottom) for comparison; the isochrone (red line) has [Fe/H]= −1.6 and 13 Gyr in age and was produced by the canonical models of the BaSTI stellar library.

here we include only those 440 RGB and horizontal branch (HB) stars with a probability higher than 95% of being members to the Sextans dSph, as determined in Sect. 2.6.

The top-left panel of Fig. 3.6 shows the W09 LOS velocities with respect to the dwarf galaxy rest frame (DRF), after smoothing them with a kernel of $\sim 5$ arcmin. The original W09 LOS velocities in the heliocentric rest frame (HRF) were converted into the DRF ones using Eq. 4 of Walker et al. (2008), a systemic velocity of 224.3 km/s (W09) and the transformations derived in their appendix, together with the HRF proper motion of Sextans dSph measured in Casetti-Dinescu et al. (2017)[3]. In this plot we can distinguish a "ring-like" feature, which has a systemic LOS velocity larger than the rest of the stars; this feature is also visible when looking at the HRF velocities, before converting them into the DRF system. We note that we used only the W09 dataset because neither the VLT/FLAMES dataset by B11 nor the Keck/DEIMOS one by Kirby et al.

[3]After submission of the corresponding article to the journal, the Gaia collaboration released Gaia DR2 based systemic proper motions for the classical dwarf galaxies satellites of the Milky Way (Gaia Collaboration et al. 2018). We have verified that using the Gaia collaboration systemic proper motion for Sextans to transform the velocities into the DRF system the results presented in this section are unaffected.

(2010) have the appropriate spatial coverage to properly sample the detected feature; also, we decided not to combine datasets due to some systematics showing up in the comparison of velocities from overlapping Sextans members (see Figure A1 in B11), which could alter the signal.

Since the LOS velocities from the W09 Michigan/MIKE Fiber System dataset are the result of the weighted mean of measurements performed with the blue and red spectrograph channel, and sometimes of repeated measurements between overlapping pointings, we checked that the observed "ring-like" shape was not caused by any systematic difference between the velocities measured with one channel or the other, systematics in some fields or in the overlapping regions between them, or outliers in the individual measurements used to obtain the mean velocity of each star. We also analyzed the velocities of all the spectroscopic targets without considering their membership probabilities, searching for some foreground/background object in the LOS of Sextans that could be responsible of creating this "ring-like" feature on the kinematics, but none was found. We conclude then that the "ring-like" feature is real and belongs to the Sextans dSph.

The "ring-like" feature is also clearly visible at the same location in a smoothed map of ΣMg values[4] (top-right panel of Fig. 3.6), which indicates that the stars of this feature have a lower metallicity relative to the rest.

In order to characterize this feature, we used the map of smoothed velocities as a reference to manually isolate the stars of the "ring" (152 sources) according to their spatial location and to define a control sample, that is the stars located in the inner and outer regions defined by the "ring" (179 sources). We note that to characterize these two samples we analyse the original measurements in velocity and ΣMg, not the smoothed ones. To this end, before proceeding, we first performed a Kolmogorov-Smirnov (K-S) test on the measurements in DRF velocity and ΣMg of the inner and outer regions of the control sample and verified that they are compatible with having been extracted from the same distributions in velocity and ΣMg (p-values $> 0.85$ and 0.50, respectively); we can therefore treat them as a single control sample.

Already at a visual inspection, the distribution of the DRF velocities of stars in the region of the "ring" shows evident differences with respect to the control sample, and mild differences are detected also between the ΣMg distributions

[4]The ΣMg values we use throughout this work were corrected for the dependence of opacity on the gravity and temperature of the star, which Walker et al. (2009a) showed correlates with V-$V_{HB}$ along the RGB. To this aim, we applied the correction in Eq. 3 of Walker et al. (2009a), using the V magnitudes measured by W09 and B11. We excluded the stars compatible with being HB stars at the distance of Sextans, because the correction was originally developed only for RGB stars.

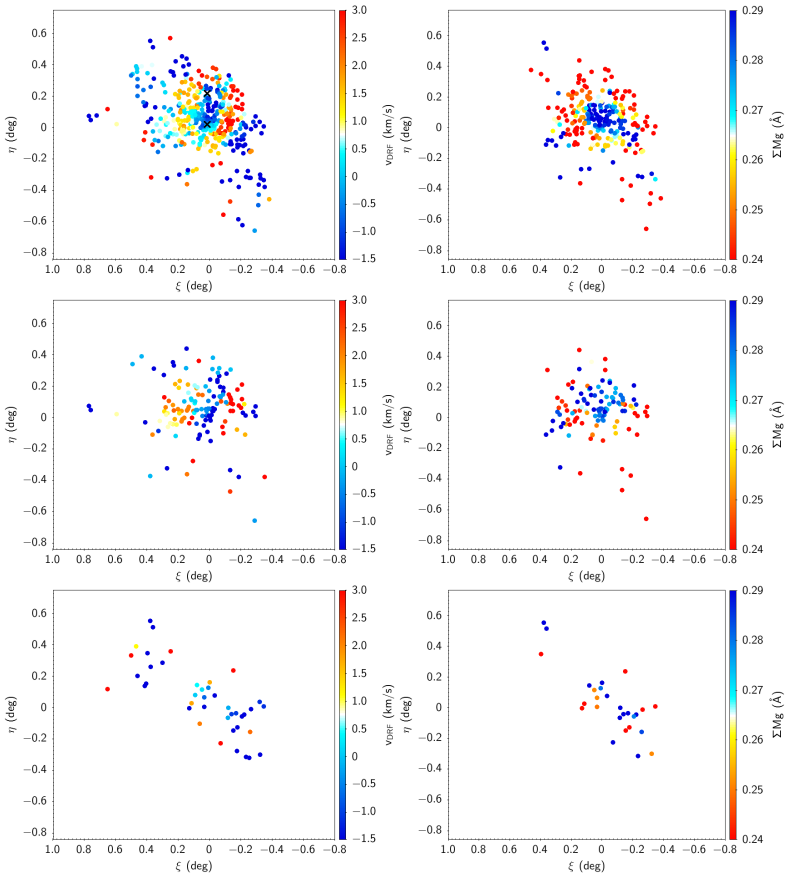


Figure 3.6: W09 spectroscopic sample of Sextans most probable members, colour-coded using median smoothed (with a kernel of $\sim$ 5 arcmin) DRF LOS velocities (left) and $\Sigma$Mg values (right), with the latter excluding the HB stars. The middle and bottom panels correspond to the blue and red CMD selections plotted in Fig. 3.1, respectively. Those members whose values of DRF LOS velocities and $\Sigma$Mg are lower and higher than the range shown in the colourbar are plotted in blue and red. This was done to enhance the contrast and emphasize the "ring", given the fact that those stars with less close neighbors are not as smoothed as the central ones. Upper and lower black crosses in the top-left panel mark the centres of the cold kinematic substructures detected in W06, and in K04 and B11, respectively.

| Parameter | "Ring" sample | Control sample |
|---|---|---|
| $\overline{v}_{DRF}$ (km/s), sample formula | 2.79 | -1.77 |
| $\sigma(v_{DRF})$ (km/s), sample formula | 8.93 | 8.47 |
| $\overline{v}_{DRF}$ (km/s), MCMC | $2.93^{+0.65}_{-0.65}$ | $-1.87^{+0.58}_{-0.58}$ |
| $\sigma(v_{DRF})$ (km/s), MCMC | $7.33^{+0.51}_{-0.47}$ | $7.27^{+0.46}_{-0.43}$ |
| $\overline{\Sigma Mg}$ (Å), sample formula | 0.254 | 0.281 |
| $\sigma(\Sigma Mg)$ (Å), sample formula | 0.104 | 0.120 |
| $\overline{\Sigma Mg}$ (Å), MCMC | $0.246^{+0.009}_{-0.009}$ | $0.273^{+0.009}_{-0.009}$ |
| $\sigma(\Sigma Mg)$ (Å), MCMC | $0.046^{+0.009}_{-0.009}$ | $0.069^{+0.009}_{-0.009}$ |

Table 3.2: Means and standard deviations of the DRF LOS velocities and ΣMg distributions for the "ring" and control samples, obtained with sample formulas and the MCMC Hammer.

(see Fig. 3.7), both when unconvolved (top) and convolved (middle) with the measurement errors; specifically, when considering the unconvolved distributions, the mean velocities and ΣMg confirm that the "ring" moves faster and is more metal-poor than the control sample, while no significant difference is measured in the spread (quantified by the standard deviation) for both observables (see Table 3.2). If we approximate the distributions as Gaussians, as it is commonly done (an approximation valid to a first order only, as we will see below), and derive the mean and intrinsic dispersions via a MCMC maximum likelihood analysis that takes into account the scatter caused by the uncertainties on the individual measurements, we confirm that the "ring" moves faster and is more metal-poor than the control sample, with the means of the distributions being separated by more than $7\sigma$ and $3\sigma$ (see Table 3.2). K-S tests between the "ring" and the whole control sample yield a negligible (p-value $< 10^{-8}$ in velocity) and unlikely (p-value $< 0.05$ in ΣMg) probability that they were extracted from the same parent distributions. We note that neither the "ring" nor the control sample have a systemic velocity equal to the literature values, while there are not appreciable changes in the velocity dispersion.

In order to estimate the number of "ring" members from its selected candidates, we summed all their membership probabilities according to the Gaussian distributions fitted for the control and "ring" samples, obtaining a total of 84 stars following the velocity and ΣMg distributions of the "ring"; that is $\sim 20\%$ of the total 440 analysed stars. This would set a lower limit in the number of "ring" members if considered as an accreted object.

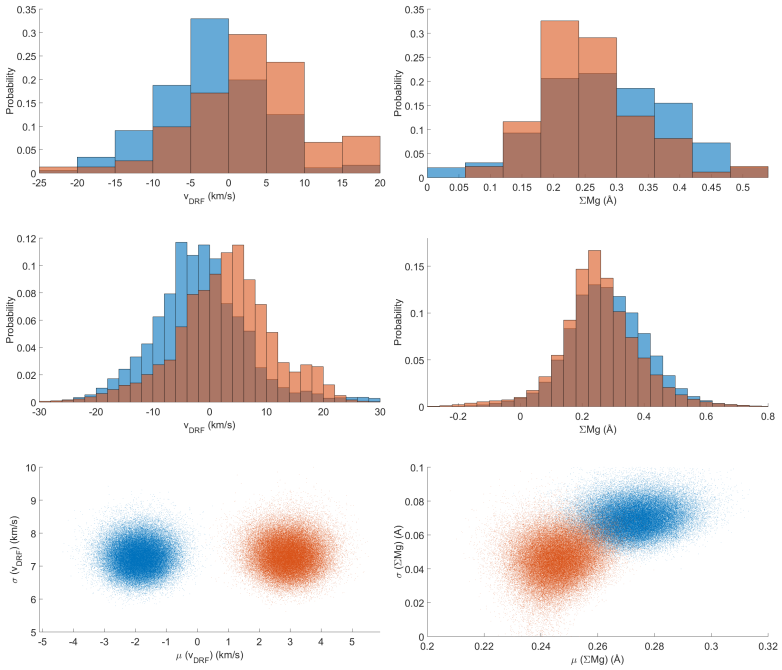


Figure 3.7: Left: DRF LOS velocity analysis. Right: ΣMg analysis. Top and middle panels: Distributions not convolved and convolved by the errors in the measurements, respectively. Bottom: Samplings from the MCMC Hammer of the mean and intrinsic standard deviation of the distributions. The results corresponding to the "ring" and control samples are plotted in red and blue respectively.

From Fig. 3.7 it is also apparent that neither the "ring" nor the control sample velocity distributions are Gaussians. In order to substantiate this statement, while taking into account the fact that the shape of the distributions might be influenced by the measurement errors, we randomly extracted numerous resamples from both convolved distributions, each with the same number of members as their original samples, and performed an Anderson-Darling test to each of them. As a result, we obtained an unlikely probability for both samples of being extracted from a Gaussian velocity distribution (median p-values $< 0.007$ and 0.05 from the control and "ring" resamples, respectively). While this fact in itself does not necessarily imply that the populations are not in dynamical equilibrium, it appears indicative of complex stellar kinematics, probably due to the left-over of the accretion/merging event that produced the "ring-like" feature.

Finally, the middle and bottom panels of Fig. 3.6 show the smoothed DRF velocity and $\Sigma$Mg maps associated to the targets with magnitude and colours that place them in the blue and red CMD selections, respectively, used in Sect. 3.2. The round shape observed for the blue population selected in the CTIO/DECam photometric data is reflected in the round shape of the blue spectroscopic targets, as it is the flattened and clumpy distribution of the red population, despite the much brighter magnitude cut used in the spectroscopic sample, just below the HB. In spite of the lower statistics caused by the CMD selection and the colour uncertainties mixing both populations, we can still distinguish the "ring" in the blue selection, both in the velocity and $\Sigma$Mg maps, but not in the red selection, in which it coincides with a lack of stars. Therefore, even the population of CMD-blue selected stars, with a seemingly regular spatial distribution, harbors complex kinematic features, whose origin is difficult to understand within a quiet evolutionary history, and would strongly suggest a past accretion or merging event. Being the spatial distribution of the blue stars the most axisymmetric of the CMD-selected components, we show in Fig. 3.8 the LOS velocity dispersion profile of the CMD-selected spectroscopic members in the DRF system as complementary information. It was calculated using the expectation maximization (EM) technique outlined in W09, in the alternative form described in Sect. 2.6. It is possible that the "ring" feature is contributing to the slightly larger velocity dispersion values visible between a radius of 0.1 and 0.3 deg.

We note that the cold kinematic substructures previously detected in W06 and K04 fall within the inner region of the control sample (see black crosses in the top-left panel of Fig. 3.6), while the cold substructure detected in B11 for the metal-poor stars encompasses both parts of the control and "ring" samples. As in W06, in this work we do not detect any cold substructure for the metal-

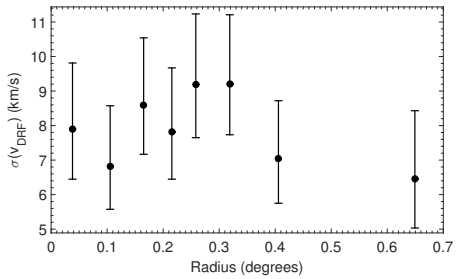


Figure 3.8: DRF LOS velocity dispersion profile of the blue CMD-selected spectroscopic members as a function of the elliptical radius.

poor stars where B11 detected it, that is within a major axis distance of 0.2 deg (Fig. 3.8). This is probably due to the different number of stars being analyzed in this region (6 in B11 vs. 18 per bin in this work) and to the different selection in metallicity. Regarding the ones detected in W06 and K04, we have not performed an analysis of the local velocity dispersion properties of all the available stars, therefore our findings are not excluding the presence of these features, which, within an accretion/merging scenario, could perhaps be the local clustering of accreted stars close to apocenter.

## 3.4 Discussion and conclusions

By analyzing literature wide-area photometric and spectroscopic datasets for large samples of individual stars in the Sextans dSph, we have uncovered anomalies in both the spatial distribution and kinematic properties of Sextans' stellar component. We have found a clearly different spatial distribution for the blue and red RGB (and MSTO) stars, which is almost round and regular for the former, while being asymmetric and clumpy for the latter. In addition we have found that their different spatial distributions are the responsible of the dependence of the obtained structural parameters on the chosen magnitude cut in Chapter 2 and the underdensities there detected. Comparison with isochrones and spectroscopic metallicities showed that the photometrically selected blue stars are on average more metal-poor than the red stars.

In the analysis of the spectroscopic dataset, we have found that Sextans hosts a "ring-like" feature which is detected both in the kinematic and relative metallicity (as given by the ΣMg) properties. Despite there being a few wiggles in the LOS velocity dispersion profile of Sextans (W09, B11 and Fig. 3.8), as the "ring" feature can be described as a tilted ellipse, it was not previously detected as a clear change in the mean velocity or increase in the velocity dis-

persion at a given radius when studying these properties via binning individual velocities in elliptical annuli. The CMD-selected, seemingly regular looking, blue component has actually complex underlying properties, being the composition of at least two velocity and metallicity distributions with different means, one of which forms the aforementioned "ring". It has to be noted that both the velocities of the "ring" and the ones of the surrounding stars have an unlikely probability of being extracted from a Gaussian distribution, which probably indicates even further kinematic complexities within these populations.

A likely explanation for the anomalies we detected is a past accretion/merger event; in fact, several of the characteristics are reminiscent of those seen in on-going accretion events or in systems thought to have experienced an accretion/merger. For example, the clump from the red RGB stars in Sextans resembles a portion of a stellar stream, shell or ripple related to accretion events detected in larger galaxies (Martínez-Delgado et al. 2009, 2012; Rich et al. 2012), while "ring-like" projected shapes (usually referred as arcing loops or just stellar streams) similar to the one detected in this work have also been found in more massive galaxies (Martínez-Delgado et al. 2008; Chonis et al. 2011).

As in the case of Sextans, the Fornax dSph, which is possibly the result of the late-merger of a bound pair (Amorisco & Evans 2012), shows a shell-like feature within its main-body (Coleman et al. 2004), a clump off-set from the centre after dividing its RGB into a blue and a red portion (Fig. 8 in Battaglia et al. 2006), and was found to display hints for a non-equilibrium kinematics in its metal-poor stellar population in the central regions (Battaglia et al. 2006); later on, an even more complex picture was unveiled, with evidences for counter-rotation between the metal-poor and metal-rich component (Amorisco & Evans 2012). The kinematically detected "ring" in Sextans bears a morphological resemblance to the stellar stream in the And II dSph (Amorisco et al. 2014), which likely merged with another dwarf of at least one tenth of And II stellar mass. Differently from the case of And II though, where a clear velocity gradient is observed across the stream, the "ring" in Sextans appears to have overall a higher systemic LOS velocity than the rest of Sextans population, perhaps resulting from an helical orbit. However the "ring" could be telling just part of the story and being formed by the dispersed stars of the accreted object which happen to have a more distinct kinematic pattern, while the rest is *hiding* under a more normal kinematics, and showing up in the non-Gaussianity of the LOS velocity distribution of stars at the location of the "ring" and outside.

Since the kinematically detected "ring" displays on average a lower metallicity than the rest of the population, it is possible that it is, at least partly, formed by the remnant of an object more metal-poor than Sextans; this appears rea-

sonable at the light of the luminosity-metallicity relation of LG dwarfs (Kirby et al. 2013). But how did the asymmetric, clumpy, redder/more metal-rich component originate? Did it originate *in-situ* during the accretion or merger event? Simulations such as those by Benítez-Llambay et al. (2016) point to the possibility that the old stellar component of dwarf galaxies might be assembled in mergers, while the younger one would mostly form *in situ* from the accreted gas a few Gyr after. However, the star formation history and general chemical properties of Sextans are compatible with the galaxy being a fossil from the pre-reionization era (Bettinelli et al. 2018; Revaz & Jablonka 2018), which imposes tight constraints for the sequence of events that shaped the object and makes it hard to understand how the clumps and asymmetries could have survived for such a long time. Clearly, understanding the details of the possible accretion/merger event experienced by Sextans will require dedicated simulations, which should take into account the wealth of observational information available for this galaxy.

Finally, it is worth mentioning that while the smallest galaxy with univocal signs of accretion up to date was the And II dSph (Amorisco et al. 2014), which has a stellar mass of $\sim 10^7 M_\odot$ (McConnachie et al. 2007), Sextans has a stellar mass of just $\sim 5 \times 10^5 M_\odot$ (McConnachie 2012), that is to say $\sim 5\%$ of the luminous mass of And II. This places Sextans as the smallest galaxy presenting clear observational signs of accretion to date.

# 4

# Tracing the stellar component of low surface brightness Milky Way Dwarf Galaxies to their outskirts II: Ursa Minor

**L. Cicuéndez, G. Battaglia, M. Irwin, E. Tolstoy**

**ABSTRACT**

**Aims.** We present results from deep and wide-area archive CFHT/MegaCam $g$ and $r$ photometry (reaching out to $\sim 2.5$ magnitudes below the oldest main-sequence turn-off and covering $\sim 4$ deg$^2$) around the Ursa Minor (UMi) dwarf spheroidal galaxy. We use this dataset to study the global structure of UMi overall stellar component and to search for possible substructures and signs of tidal disturbance from the Milky Way, which would indicate departure from dynamical equilibrium.

**Methods.** By applying Bayesian Markov chain Monte Carlo methods to the individual stars' locations, we obtained the most accurate structural parameters to-date of UMi overall stellar component. Its surface density map was statistically decontaminated by a matched filter analysis of its colour-magnitude diagram and a decontamination method acting on the individual stars without spatial binning, and then examined for deviations from axisymmetry.

**Results.** We find overall agreement with the structural parameters derived in early studies. We also identify a previously reported stellar overdensity in the northeast side of the galaxy, which was found in the literature to be associated with a cold kinematic substructure, and reveal other overdensities in the southwest side and another one close to the galactic centre. While the latter could result from a plausible central black hole often investigated in the literature, the other overdensities are probably remnants of a disrupted stellar cluster. No other statistically significant distortions or signs of tidal disturbances were found down to a surface brightness limit of $\sim 32$ mag/arcsec$^2$ in V-band. Finally, we calculate the membership probabilities of a literature spectroscopic sample, analyzing the metallicity and line-of-sight velocity distributions of its probable members and not finding any radial gradient across de galaxy either on the individual metallicities or in the velocity dispersion.

## 4.1 Introduction

In this chapter we study the properties of the stellar component of the Milky Way (MW) satellite UMi, searching for the possible presence of signs of tidal disturbance and quantifying the structural properties of its overall stellar population.

Discovered in the Palomar survey by Wilson (1955), UMi is at an heliocentric distance of $76 \pm 4$ kpc (Carrera et al. 2002), has a luminosity of $3.9^{+1.7}_{-1.3} \times 10^5 L_\odot$ in V-band (Wolf et al. 2010) and a mean line-of-sight (LOS) velocity of $-247.0 \pm 0.8$ km/s with $11.61 \pm 0.63$ km/s of average velocity dispersion (Pace et al. 2014). Some of these values translate into a dynamical mass-to-light ratio of $\sim 100-200\ M_\odot/L^V_\odot$ (Lora et al. 2012), which makes UMi one of the most dark matter dominated galaxies known.

Its structural parameters were carefully derived for the first time in Hodge (1964) from photographic plates, and the latter estimates of its half-light radius give a value of $0.445 \pm 0.044$ kpc (Palma et al. 2003, hereafter P03). Bermejo-Climent et al. (2018) further showed that all the structural parameters of its horizontal branch (HB) stars are fully compatible with the ones of the overall stellar population (Irwin & Hatzidimitriou 1995, hereafter IH95; P03), which implies that the spatial distribution of the stars older than $\gtrsim 10$ Gyr does not differ from the global one. Spectroscopic observations show that UMi has an average metallicity of [Fe/H] $= -2.13$ with a spread of $\sigma = 0.34$ (Kirby et al. 2011) and no metallicity gradients are detected across the galaxy (Carrera et al. 2002; Kirby et al. 2011; Jin et al. 2016) out to its tidal radius.

Its stars appear to have been formed earlier than 10 Gyr ago, with 90% of them having formed more than 13 Gyr ago (Carrera et al. 2002). Deep radio observations have not detected HI gas (Young 2000) from which stars could form now, what Ural et al. (2015) ascribed to a continuous loss of gas modeled as winds.

UMi also shows a secondary peak in its stellar surface density (Bellazzini et al. 2002), where Kleyna et al. (2003) later detected a cold kinematic substructure also confirmed by Pace et al. (2014). These two latter works argued that this cold substructure could probably be a stellar object that survived orbiting within the gravitational potential of the galaxy thanks to, either having its own dark matter halo that protects it, or to a UMi dark matter halo being cored rather than cuspy. Additionally, Wilkinson et al. (2004) reported another kinematically cold population in the outer parts of UMi, but Muñoz et al. (2005) and Wu (2007) later argued that this was just an artifact that only appears under certain spatial binning schemes.

On the other hand, Bellazzini et al. (2002) demonstrated that the inner regions of UMi are highly structured, not necessarily what is expected for a galaxy in dynamical equilibrium. This fact, UMi's large ellipticity ($\epsilon = 0.55$ vs. a typical value of $\sim 0.3$ for the classical dSphs) and its relatively small pericentric distance of its orbit around the MW (Fritz et al. 2018) make UMi a good candidate for being tidally disturbed by the MW, although hard to study in detail due to the difficulty of completely mapping its large stellar body (with a King tidal radius of $\sim 1$ deg) and separating its stars from the MW contaminants. Indeed, some works have reported the presence of candidate 'extra-tidal stars' in UMi (P03; Muñoz et al. 2005) by making selections in the colour-magnitude and two-colour diagrams (CMD and 2CD, respectively), and in radial velocity. Nonetheless, in addition to the fact that these selections can still be contaminated by nonmember stars, other later works have not confirmed these detections of candidate 'extra-tidal stars' (Read et al. 2006; Wu 2007) and, although for a long time UMi has been suspected of being tidally disturbed, overdense regions and cold kinematic substructures cannot result from tidal interactions (Kleyna et al. 2003; Read et al. 2006; Sánchez-Salcedo & Lora 2007). Likewise, the time elapsed from its last pericentric passage (Gaia Collaboration et al. 2018) is dozens of times larger than its dynamical timescale, so that UMi is expected to have relaxed back to equilibrium since then, erasing any signs of a possible past tidal interaction with the MW (Peñarrubia et al. 2008).

Finally, Strobel & Lake (1994) suggested the possible existence of a central black hole in UMi which might be detectable in radio and X-rays and could cause a prominent cusp in the star counts close to it. In fact, at the centre of the galaxy, Nucita et al. (2013) later detected a possible X-ray source spatially coincident with a previously discovered radio object (Maccarone et al. 2005). These two detections are indeed possibly associated with a black hole hosted at the centre of the galaxy, with a minimum mass of $5 \cdot 10^4 M_\odot - 5 \cdot 10^5 M_\odot$ (Nucita et al. 2013).

In this chapter we present a comprehensive wide-area study of UMi' stellar population using deep photometry in $g-$ and $r-$ bands (reaching out to $\sim 2.5$ magnitudes below the oldest main sequence turn-off) from a mosaic of CFHT/MegaCam pointings over $\sim 2{\times}2$ deg$^2$ centered on the UMi dwarf spheroidal galaxy (dSph), hence reaching beyond its nominal IH95 King tidal radius. This photometry was also recently published and analyzed in Muñoz et al. (2018) (hereafter M18), and yields the most deep and spatially extended photometric dataset available for UMi so far. Using statistically sophisticated tools, we performed a detailed quantitative analysis of the structural properties of this galaxy. This chapter is organized as follows. Section 4.2 presents

the observations, the reduction of the resulting data and the obtained photometric catalogue. In Sect. 4.3 we obtain the structural parameters of the overall stellar population of the galaxy and calculate the goodness-of-fit of various functional forms for the surface density profile. We decontaminate UMi surface density map, obtain its deviations from axisymmetry and derive the two-dimensional likelihood ratios between the best-fitting density profiles in Sect. 4.4. In Sect. 4.5 we calculate the membership probabilities of the stars from the Jin et al. (2016) spectroscopic sample of UMi, analyzing and searching for possible radial gradients in the metallicity and LOS velocity distributions of its probable members. Finally, we present the summary and conclusions of this work in Sect. 4.6.

## 4.2 Observations and data reduction

The data were obtained from the CFHT archive. The observations were carried out on the nights of June 12-14 and July 7-13 2010 with the instrument MegaCam on the 3.6m CFHT (PI: P. Côté). MegaCam is a wide-field CCD imager containing 36 2048×4612 pixel CCDs, covering a field of view of almost 1×1 deg at 0.187 arcsecond/pixel resolution.

The observations consisted of a mosaic composed of 4 pointings centered on the UMi dSph and covering approximately 4 deg$^2$, reaching out to slightly beyond the IH95 estimate of its nominal King tidal radius. All the pointings were observed with six exposures of 360s in both the $g-$ and $r-$ bands, dithering between the individual exposures with spatial offsets chosen to approximately fill the gaps between the chips. The typical seeing was around 0.7-0.9".

The data were reduced by the Cambridge Astronomical Survey Unit (CASU), using the same pipeline used with Sextans' data in Chapter 2 (Irwin & Lewis 2001). Henceforth this section is analogous to Sect. 2.2 and we describe in the following the analysis that was not carried out by CASU. We did not carry out artificial star tests but we are confident that there is no crowding in our data: we have checked that there is no increase of extended/blends sources in the innermost regions, and that the magnitude limit in the central region compares well with the rest of the data.

In the following we will only refer to those sources classified as point-like in both photometric bands, in order to exclude noise, background galaxies and blends. Indeed, as it can be seen in Fig. 4.1, by selecting only point-like sources in both photometric bands we effectively removed the artificial overdensities and clusters of galaxies.

Once the instrumental magnitudes of the different pointings from the mosaic were internally calibrated, the whole mosaic was externally calibrated at once

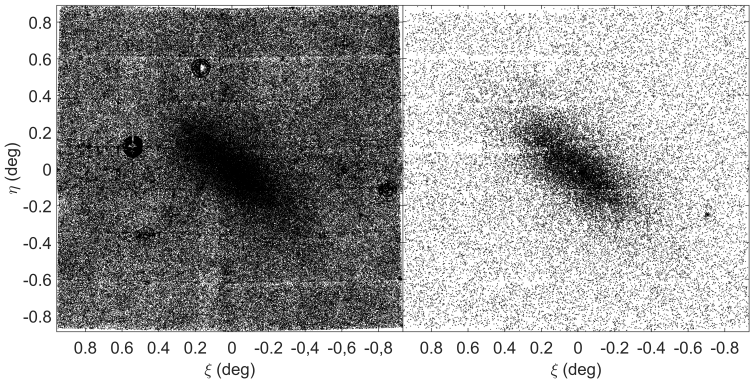


Figure 4.1: Locations of the objects from the CFHT/MegaCam photometric catalogue. Left: all sources; right: point-like sources brighter than $(g, r) = (24.6, 23.9)$, that is S/N=10 of the shallowest pointing. The MFM contamination filter was obtained from the northwest corner of the surveyed area.

by cross-correlating our MegaCam catalogue with the SDSS DR14 point-like catalogue (Albareti et al. 2017) in $g_{SDSS}$ and $r_{SDSS}$ bands. A linear fitting (Eq. 2.1 from Chapter 2) was enough for the purpose (Fig. 4.2). The fitted colour terms are $c_g = -0.1732$ and $c_r = -0.0311$, with a scatter of $\sigma_g = 0.032$ mag and $\sigma_r = 0.033$ mag. The measured $g_{SDSS}$ band magnitudes and those predicted by the relation (top panel Fig. 4.2) are in very good agreement, with only a minor deviation for the faintest sources, where the completeness in $r_{instr.}$ band starts decaying first. Regarding the $r_{SDSS}$ band, the bottom panel of Fig. 4.2 shows that the transformation works well down to the faintest magnitudes. The separations from the associated pairs retained by the linear fitting reveals that the measured positions of our stars agree with the SDSS astrometry within $\sim 0.6''$. The depth of the catalogue is $M_{g,\,AB} \simeq 25.6$ and $M_{r,\,AB} \simeq 25.0$ at S/N $\simeq 5$, $M_{g,\,AB} \simeq 26.2$ and $M_{r,\,AB} \simeq 25.5$ at S/N $\simeq 3$.

Next, we corrected the calibrated $g-$ and $r-$ magnitudes of the individual sources for Galactic extinction using the dust map of Schlegel et al. (1998) and the 14% reddening recalibration and extinction coefficients from Schlafly & Finkbeiner (2011): the median values of the extinction in our surveyed area were $A_g = 0.092$ mag and $A_r = 0.064$ mag, the minimum were $A_g = 0.053$ mag and $A_r = 0.037$ mag and the maximum $A_g = 0.126$ mag and $A_r = 0.087$ mag. A sample of the catalogue of point-like sources is given in Table 4.1. In

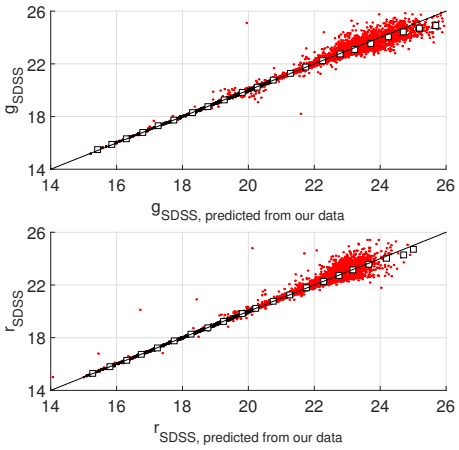


Figure 4.2: Linearity checks of the photometric calibration with SDSS in $g-$ (top) and $r-$ (bottom) bands. The stars used for the linear fitting are shown as black dots, and are the majority of those having $g_{\rm SDSS} \lesssim 21$ and $r_{\rm SDSS} \lesssim 20.5$, while the stars not used are shown as red dots (outliers or those with errors larger than 0.03 mag). In both panels the white squares give the median values in 0.5 mag-wide bins and the black line shows the one-to-one relation.

the following we will only show the photometry corrected for extinction and reddening.

The CMD of the whole photometric catalogue for point-like sources is shown in Fig. 4.3. The features of UMi stellar population (sub- and red giant branch, main sequence, main sequence turn-off, blue stragglers and horizontal branch) are clearly distinguishable, as well as the presence of contaminating Milky Way foreground stars.

Hereafter, unless otherwise specified, we carry out our analysis over the photometric catalogue cut at S/N=10 of the shallowest pointing, that is $(g, r) \simeq (24.6, 23.9)$ (right panel of Fig. 4.1).

## 4.3 Structural parameters

We derived the structural parameters following the methodology described in Sect. 2.3 based on Richardson et al. (2011) to avoid the loss of information due to spatial binning of the data, that is evaluating at the individual stellar locations a likelihood expression depending on the surface density profile to be fitted, the position angle, ellipticity, density of contaminants, etc. As in Sect. 2.3, for the dSph surface density profile we evaluated the performance of an exponential profile, a King profile (King 1962), a Sérsic profile (Sersic 1968) and a Plummer model (Plummer 1911). The surface density of foreground and background contaminants was instead modelled as an uniform distribution,

| ID | $\alpha_{2000}$ (hh:mm:ss) | $\delta_{2000}$ (dd:mm:ss) | g (mag) | g class | r (mag) | r class | E(B-V) (mag) |
|---|---|---|---|---|---|---|---|
| 1 | 15:18:36.996 | 67:04:11.67 | 23.512±0.035 | -1 | 22.113±0.020 | -1 | 0.02584 |
| 2 | 15:17:48.009 | 67:04:17.74 | 23.979±0.050 | -1 | 23.221±0.048 | -1 | 0.02883 |
| 3 | 15:15:14.316 | 67:04:23.82 | 24.999±0.125 | -1 | 24.414±0.123 | -1 | 0.03430 |
| 4 | 15:17:31.983 | 67:04:24.06 | 24.083±0.061 | -1 | 23.891±0.079 | -1 | 0.03087 |
| 5 | 15:16:47.166 | 67:04:24.43 | 24.886±0.117 | -2 | 25.002±0.199 | -1 | 0.03129 |
| 6 | 15:13:05.704 | 67:04:25.24 | 23.846±0.049 | -1 | 22.997±0.039 | -1 | 0.03398 |
| 7 | 15:13:53.547 | 67:04:25.32 | 24.220±0.072 | -1 | 22.938±0.036 | -1 | 0.03587 |
| 8 | 15:09:58.273 | 67:04:25.71 | 24.316±0.079 | -1 | 23.748±0.072 | -1 | 0.03478 |
| 9 | 15:10:56.679 | 67:04:26.42 | 23.935±0.058 | -1 | 23.134±0.044 | -2 | 0.03523 |
| 10 | 15:14:17.975 | 67:04:26.62 | 23.281±0.034 | -1 | 23.079±0.041 | -1 | 0.03753 |
| ... | ... | ... | ... | ... | ... | ... | ... |

Table 4.1: Sample of the UMi point-like source catalogue in the SDSS photometric system. The classification flags in each band are described in Sect. 2.2. The reddening E(B-V) was derived from Schlegel et al. (1998) dust map. These $g-$ and $r-$ magnitudes are not corrected for their corresponding extinctions.

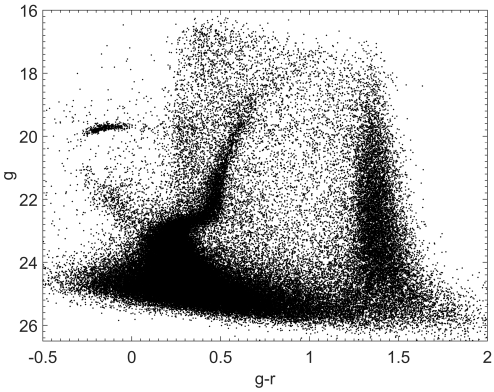


Figure 4.3: CMD of the whole MegaCam catalogue for point-like sources. RGB, MS, MSTO, BSs candidates and HB features from UMi stellar population are clearly visible.

due to the much smaller surveyed area compared to that from Chapter 2. The most likely value of each structural parameter was then obtained by sampling the likelihood expression with a Bayesian Markov chain Monte Carlo (MCMC) sampler of the form from Goodman & Weare (2010): 'The MCMC Hammer'[1] (Foreman-Mackey et al. 2013).

As UMi is also at relatively low Galactic latitude ($l = 105.0$, $b = +44.8$), we still expect a large number of foreground MW stars contaminating our photometric catalogue, besides the unresolved background galaxies. Thus, to limit the amount of such contaminants as in Sect. 2.3, from now on we will only consider point-like sources within a contour at approximately 1% the maximum value of the Hess diagram from the central part of the galaxy (left panel of Fig. 4.4). High resolution Hess diagrams from Fig. 4.4 were obtained from the central $\sim 10$ arcmin of UMi (left panel) and the northwest corner of the surveyed area (right panel), and smoothed with a two-dimensional Gaussian of $\sigma_{g-r} \simeq 0.06$ mag and $\sigma_g \simeq 0.11$ mag.

Table 4.2 shows the obtained structural parameters of the different surface density profiles fitted, as well as their posterior Bayes factors (PBFs) in the alternative way described by Aitkin (1991). The 2D half-light radius $r_h$ of the different functional forms were again derived using the formulas in Appendix B of Wolf et al. (2010). As an example, Fig. 4.5 shows the resulting Bayesian posterior distributions of the structural parameters when using a Plummer profile to model the observed surface number density.

[1] `https://github.com/grinsted/gwmcmc`

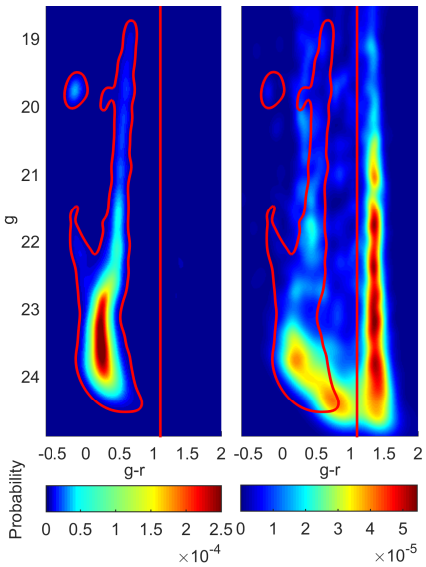


Figure 4.4: High resolution Hess diagrams from two different spatial regions. Left: central parts of UMi (MFM signal filter). Right: control region (MFM contamination filter). Stars redder than $g - r = 1.1$ (red vertical line) were excluded from the analysis, as they correspond mainly to MW dwarf stars. Red contours: window defined to exclude most contaminants. Hess diagrams are colour-coded according to the probability of finding a star with a given mag and colour.

We can see that the values of the centre, position angle and ellipticity we derive from the MegaCam catalogue (Tab. 4.2) are compatible within their $1\sigma$ uncertainties between the different surface number density profiles fitted, and in good agreement with those from IH95, P03 and M18, except for the fact that the value of the centre in M18 is slightly offset from the rest. On the other hand, our mean 2D half-light radius is slightly larger than the one by IH95 (though we note the stronger disagreement between the 2D half-light radius derived from the best-fitting parameters of the IH95 King and exponential models) but compatible with the ones from P03 and M18. As our photometric catalogue is much deeper than the ones from IH95 and P03, it is expected that the structural parameters here are better constrained. The tidal radius fitted here is also larger than the one of IH95, but again compatible with the ones from P03 and M18, and our Sérsic index is exactly the same as the one of M18. In addition, all our structural parameters are fully compatible with the ones of the HB stars obtained by Bermejo-Climent et al. (2018), who not only analysed the same photometric catalogue as us, but also used our method to derive them. This fact implies that the spatial distribution of the stars older than $\gtrsim$ 10 Gyr does not differ from the one of the overall stellar population.

| Parameter | Exponential | Sérsic | Plummer | King | IH95 | P03 | M18 |
|---|---|---|---|---|---|---|---|
| $\alpha_{2000}$ (º) | $227.257^{+0.002}_{-0.002}$ | $227.258^{+0.002}_{-0.002}$ | $227.259^{+0.002}_{-0.002}$ | $227.259^{+0.002}_{-0.002}$ | $227.25^{+0.03}_{-0.03}$ | $227.266^{+0.007}_{-0.007}$ | $227.242^{+0.005}_{-0.005}$ |
| $\delta_{2000}$ (º) | $67.228^{+0.002}_{-0.002}$ | $67.229^{+0.002}_{-0.002}$ | $67.229^{+0.002}_{-0.002}$ | $67.229^{+0.002}_{-0.002}$ | $67.23^{+0.02}_{-0.02}$ | $67.231^{+0.006}_{-0.006}$ | $67.222^{+0.002}_{-0.002}$ |
| Ellipticity | $0.540^{+0.005}_{-0.005}$ | $0.543^{+0.005}_{-0.005}$ | $0.540^{+0.005}_{-0.005}$ | $0.542^{+0.005}_{-0.005}$ | $0.56^{+0.05}_{-0.05}$ | $0.54^{+0.02}_{-0.02}$ | $0.55^{+0.01}_{-0.01}$ |
| Position angle (º) | $51.1^{+0.4}_{-0.4}$ | $51.0^{+0.3}_{-0.4}$ | $51.1^{+0.4}_{-0.4}$ | $51.0^{+0.4}_{-0.4}$ | $53^{+5}_{-5}$ | $49.0^{+1.6}_{-1.6}$ | $50^{+1}_{-1}$ |
| Sérsic index n | - | $0.82^{+0.02}_{-0.02}$ | - | - | - | - | $0.82^{+0.01}_{-0.01}$ |
| Sérsic factor b(n) | - | $0.8^{+0.5}_{-0.5}$ | - | - | - | - | - |
| Exponential $r_e$ (′) | $10.58^{+0.10}_{-0.09}$ | - | - | - | $10.1^{+0.1}_{-0.1}$ | - | $10.89^{+0.07}_{-0.07}$ |
| Plummer $r_p$ (′) | - | - | $19.2^{+0.2}_{-0.2}$ | - | - | - | $18.3^{+0.2}_{-0.2}$ |
| Sérsic $r_s$ | - | $12^{+5}_{-5}$ | - | - | - | - | $17.3^{+0.2}_{-0.2}$ |
| King $r_c$ (′) | - | - | - | $14.2^{+0.3}_{-0.3}$ | $16^{+2}_{-2}$ | $17.9^{+2.1}_{-2.1}$ | $13.5^{+0.3}_{-0.3}$ |
| King $r_t$ (′) | - | - | - | $74^{+2}_{-2}$ | $51^{+4}_{-4}$ | $77.9^{+8.9}_{-8.9}$ | $77.3^{+0.7}_{-0.7}$ |
| 2D half-light $r_h$ (′) | $17.8^{+0.2}_{-0.2}$ | $12^{+5}_{-5}$ | $19.2^{+0.2}_{-0.2}$ | $17.2^{+0.3}_{-0.3}$ | $17.0^{+0.2}_{-0.2}$ (Exp.) | - | $18.2^{+0.1}_{-0.1}$ (Exp.) |
| | | | | | - | - | $17.3^{+0.2}_{-0.2}$ (Sérsic) |
| | | | | | $14.5^{+0.8}_{-0.8}$ (King) | $19.6^{+2.3}_{-2.3}$ (King) | $18.3^{+0.2}_{-0.3}$ (Plum.) |
| | | | | | - | - | $15.4^{+0.3}_{-0.3}$ (King) |
| 2ln (PBF) | - | 100.7 $\left(\frac{\text{Sérsic}}{\text{Exp}}\right)$ | 44.8 $\left(\frac{\text{Plummer}}{\text{King}}\right)$ | 14.0 $\left(\frac{\text{King}}{\text{Sérsic}}\right)$ | | | - |

Table 4.2: UMi structural parameters (median values of the marginalized posterior distributions) derived with the MCMC Hammer, plus posterior Bayes factors of the different surface density profiles. All these PFBs correspond to very strong evidences according to Table A.2. The last three columns refer to the best-fitting profiles of IH95, P03 and M18. The errors are derived from the percentiles 15.87-84.13 (corresponding to $\pm 1\sigma$ in case of normal distributions) of the marginalized Bayesian posterior distributions.

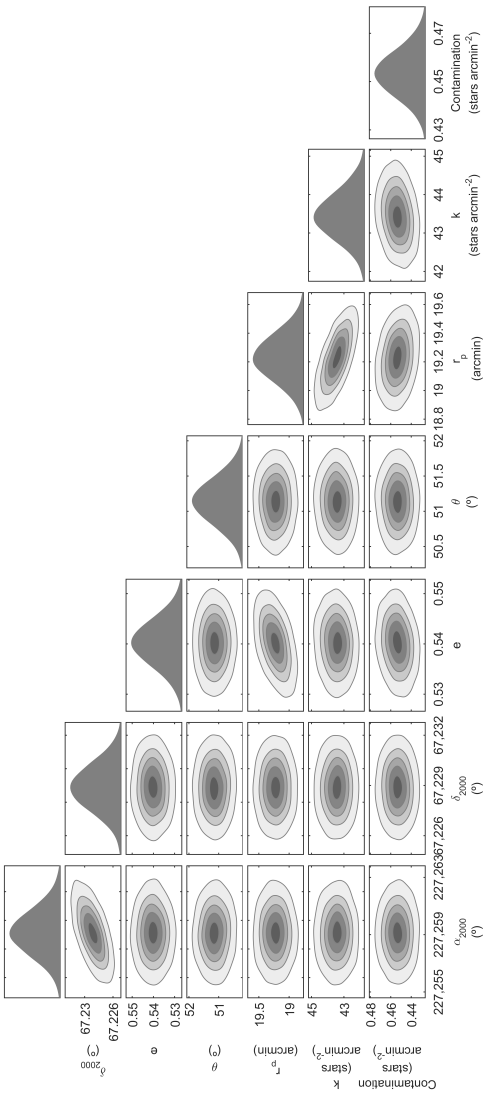


Figure 4.5: Bayesian posterior distributions of the structural parameters obtained with the MCMC Hammer when modelling the dSph surface number density as an empirical Plummer profile. Contours contain 10%, 30%, 50%, 70% and 90% of the points sampled by the MCMC Hammer. From left to right: RA ($\alpha_{2000}$), DEC ($\delta_{2000}$), ellipticity ($e = 1 - b/a$), position angle ($\theta$), Plummer radius ($r_p$), scale factor (k) and contamination density. Two-dimensional normal distributions aligned with x- and y-axes are indicative of uncorrelated parameters.

Finally, with regard to the PBFs, they favour the Plummer profile with a very strong evidence (overwhelming in the scale of Aitkin 1991) over the rest of models. The evidences given by the PBFs in Tab. 4.2 are still compatible with the work from IH95, as they only fitted an exponential and a King model to their observed surface density profile, finding a better fit for the latter, as the PBFs reveal in this work. With regard to M18 and P03, as the first ones did not analyse the goodness-of-fit of their best-fitting models, and the latter only fitted a King profile, no comparison can be done between the goodness-of-fit of different models in these two works.

In conclusion, we have obtained the most accurate structural parameters to date of the overall stellar population of UMi, which are also in overall good agreement with the ones determined by previous studies. Besides, the Plummer model turns out as the best-fitting profile for the catalogue used here, as well as the corresponding values of the centre, position angle, ellipticity and half-light radius.

In order to have larger statistics, we repeated the analysis using the photometric catalogue cut at S/N=5 of the shallowest pointing, that is $(g, r) = (25.6, 25.0)$, and checked that the structural parameters and order in the goodness-of-fit according to the PBFs remain the same. Nonetheless we restricted to the analysis at S/N=10 because the S/N=5 one is affected by small differences in depth between some pointings. Therefore, in UMi the structural parameters do not reveal any variable proportion of stellar populations as a function of magnitude through their different spatial distributions, as happened with Sextans in Chapter 2, where different structural parameters were obtained according to the adopted magnitude cut.

## 4.4 Surface density maps

The top panel of Fig. 4.6 shows the spatial distribution of UMi's point-like sources. It was decontaminated following the two methods already explained in the previous two chapters: a matched-filter analysis (MFM) as in Sect. 2.4 for obtaining the red contours and the decontamination method described in Appendix B.1 for the point-sources. The black arrow shows the direction of the systemic proper motion (Fritz et al. 2018) corrected for the solar reflex motion. In the bottom panel we derived a two-dimensional map of residuals between the MFM decontaminated surface number density map of UMi and the mean surface density obtained from the best-fitting Plummer, King, Sérsic and exponential models.

To derive the MFM iso-density contours we used the Hess diagrams of Fig. 4.4 as the 'source' and 'contamination' colour-magnitude filters, with a

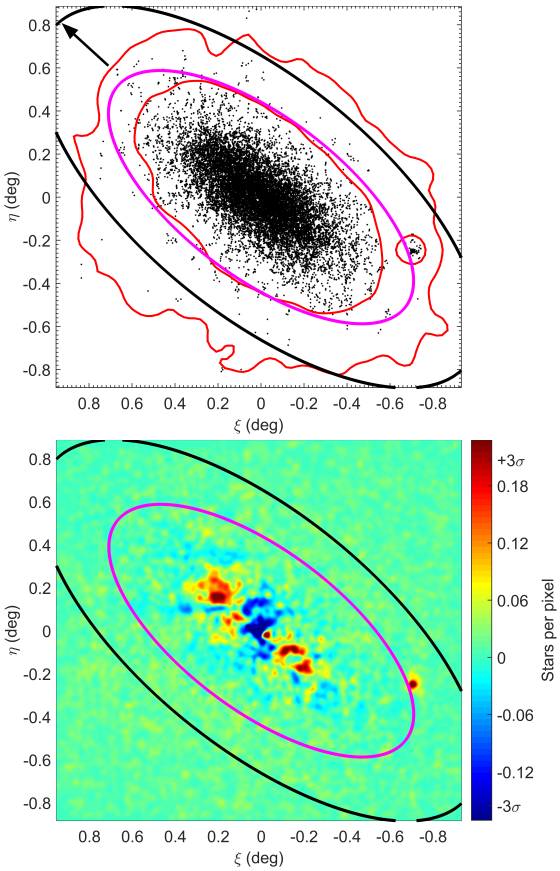


Figure 4.6: Top: Spatial distribution of UMi's stars decontaminated with the method described in Appendix B.1. The overlaid red iso-density contours trace the $1\sigma$ ($\sim 32$ mag/arcsec$^2$ in V-band) and $2\sigma$ detections from the MFM surface number density map. The pink and black ellipses show the nominal King tidal radius with parameters from IH95 and this work, respectively, while the black arrow in the northeast corner shows the direction of UMi' proper motion (Fritz et al. 2018) corrected for the solar reflex motion, that is in the Galactocentric reference frame. Bottom: Map of residuals between UMi's surface number density map decontaminated with the MFM and the mean surface density produced by the best-fitting Plummer, King, Sersic and exponential profiles (for their parameters see Table 4.2).

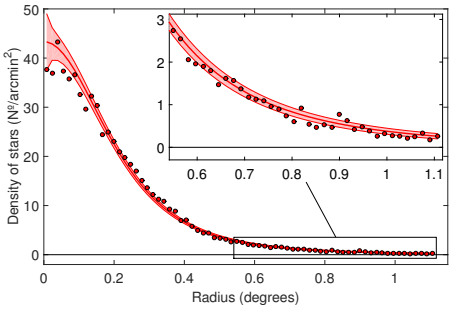


Figure 4.7: Contamination subtracted surface number density profile of UMi stars as a function of the major axis radius (with the external parts zoomed in), overlaid onto the $1\sigma$ confidence interval (red band) of the best-fitting Plummer profile obtained with the MCMC Hammer. The $1\sigma$ confidence interval is computed from the best-fitting model assuming Poisson variances in each elliptical annulus.

bin size of 1.5 arcmin per side and smoothed with a two-dimensional Gaussian of dispersion $\sigma_\xi = \sigma_\eta \sim 3$ arcmin. For the map of the residuals however, due to the presence of over- and underdensities whose sizes are smaller than these scales (see e.g. the stellar cluster that does not belong to UMi, at $(\xi, \eta) \simeq (-0.70, -0.25)$ deg, already discovered in Muñoz et al. 2012), we set a bin size of $\sim$ 10 arcsec and smoothed with a two-dimensional Gaussian of dispersion $\sigma_\xi = \sigma_\eta \sim 40$ arcsec.

The outer parts of UMi (Fig. 4.6) appear regular, with no over- or underdensities apart from the stellar cluster in the west side of the covered area, which does not belong to UMi (Muñoz et al. 2012), nor detection of large scale tidal structures with a well defined spatial trend (e.g. tidal tails). These would be expected to be located along the direction given by the systemic proper motion if UMi would be tidally affected at the present time at a Galactocentric distance of 78 kpc (Fritz et al. 2018), which would be indeed very improbable. In fact, it can be checked that its very external regions, which would be the most tidally affected, are slightly elongated with respect to the overall ellipticity of the galaxy but in the direction perpendicular to the systemic proper motion, as opposed to what would be expected if UMi would be currently tidally interacting with the MW. Nevertheless, we do find any plausible explanation for such a decrease in the ellipticity in the most external regions.

Regarding the inner regions of UMi however, the two-dimensional map of residuals does reveal some over-dense small clumps as well as under-dense regions with statistical significances larger than $3\sigma$, as the aforementioned stellar cluster, which could not otherwise be appreciated in the surface density map. The over-dense clump in the northeast side of the galaxy was already revealed in the surface density maps of IH95 and Bellazzini et al. (2002), where Kleyna et al. (2003) then detected a cold kinematic signature later confirmed by

Pace et al. (2014). This clump was not detected in M18 probably due to applying a large smoothing kernel to the surface density map or to not obtaining its corresponding map of residuals. Kleyna et al. (2003) also showed that this clump is consistent with being the remnant of a disrupted stellar cluster, and argued, as later Lora et al. (2012), that it is still orbiting within the gravitational potential of the dSph thanks to a cored dark matter halo for the galaxy instead of cuspy. The inner under-dense region is caused by an appreciable core in the inner regions of the stellar density profile (Fig. 4.7), while the stellar overdensity next to it (corresponding to the third point from the left in Fig. 4.7) could also result from a possible central black hole whose presence was originally suggested by Strobel & Lake (1994) and later possibly detected first in radio (Maccarone et al. 2005) and then in X-rays (Nucita et al. 2013), whose minimum mass would be in the range $5 \cdot 10^4 M_\odot - 5 \cdot 10^5 M_\odot$ (Nucita et al. 2013). With regard to the southwest overdensities with statistical significances larger than $3\sigma$, these were probably undiscovered in the surface density map before due to their locations in denser regions of the galaxy and smaller sizes compared to the northeast clump. Nonetheless, the velocity offset object detected by Pace et al. (2014) in spectroscopic data indeed comprises them. We also checked the map of objects classified as extended and found no correspondence between background galaxy clusters and the detected overdensities. Basing on the just mentioned work from Pace et al. (2014), on other previous works that studied the origin of the rest of overdensities also detected by us, and on the simulations from Peñarrubia et al. (2009) showing the projected stellar debris deposited during the disruption of a stellar cluster within a dwarf galaxy, which further do not dissolve in time, the most plausible explanation we find for these new overdensities is that they are probably more remnants from the disrupted stellar cluster that produced the northeast overdensity.

We also show in Fig. 4.8 the maps of the classical likelihood ratios between the best-fitting profiles, in increasing order of PFB, evaluating the likelihoods over the MFM decontaminated surface density map. Thus one can see in which regions the less probable profile of the two best reproduces the decontaminated density map. For example, we can see how the Plummer profile provides a better fit than the King one in the outer regions of UMi, while the Sérsic profile fits better than the exponential one in its inner regions. In between however, we can see a ring where the King model provides a better fit than the Sérsic one. These are just direct consequences of the different "shapes" of the fitted profiles, which are defined by their functional forms. For example, the exponential profile is cuspy (i.e. the slope of its functional form is negative at the galactic centre), while the Plummer one is cored (i.e. its functional form is flat at the galactic centre), so that an observed density profile with a central

cusp will be better fitted at its centre by an exponential profile rather than a Plummer one. Clearly, the aforementioned over- and underdensities are also reflected in these maps, as any fluctuation in the stellar density will affect the goodness of fit of whichever considered profile at its location. However, more than focusing on particular fluctuations, one should pay more attention to those features over the global structure of the galaxy that are symmetric around its galactic centre, such as the ones we have mentioned.

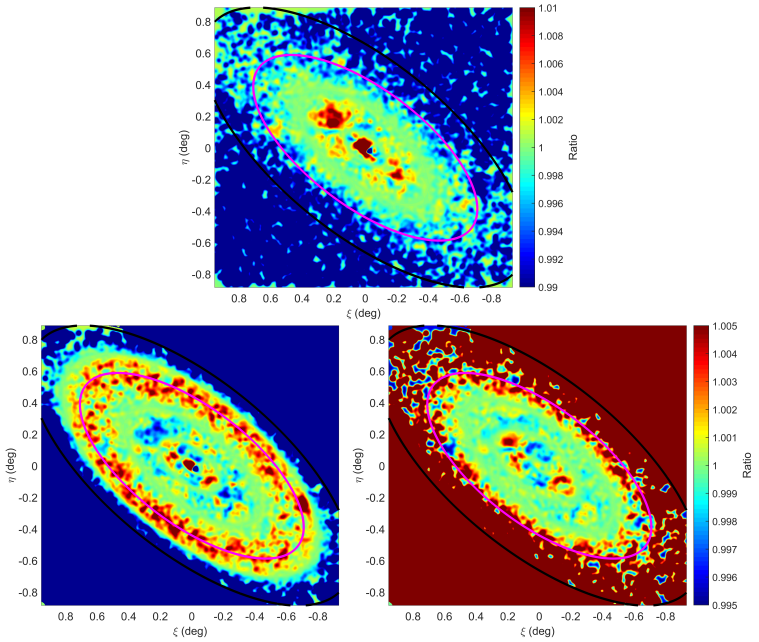


Figure 4.8: Maps showing classical likelihoods ratios between pairs of best-fitting surface density profiles, calculated pixel by pixel, in increasing order of PBF. Top: Sérsic/Exponential. Bottom-left: King/Sérsic. Bottom-right: Plummer/King. Likelihoods were calculated using the MFM decontaminated surface density map of UMi' overall stellar population (contours on the first panel of Fig. 4.6), assuming Poisson statistics at each spatial pixel. These maps allow us to detect the spatial regions where the less probable profiles fit better than the immediately more probable ones. The pink and black ellipses show the nominal King tidal radius with parameters from IH95 and this work, respectively.

## 4.5 Spectroscopic analysis

We studied the spectroscopic sample of red giant branch candidate stars in UMi presented in the preliminary work of Jin et al. (2016), obtained with the AutoFib2 (AF2) Wide Field Fibre Optical Spectrograph (WYFFOS) on the William Herschel Telescope (WHT), using the R1200R grating centered on the Ca II triplet (CaT) region and covering out to the nominal tidal radius. We analysed it with the "expectation maximization" (EM) technique outlined in Section 2.6 (W09), which also allows us to calculate the membership probabilities of the stars.

The measurements we used are the heliocentric velocity, the metallicity ([Fe/H]) and the projected distance from the galactic centre. For the probability distribution functions of the velocities and metallicities we again used the expressions given in W09 when analysing their dataset, while for the one of the galactocentric distances we adopted our revised structural parameters of the galaxy.

Lastly, before applying the EM algorithm, we ensured a high reliability for the dataset by excluding those measurements which did not satisfy these requisites: for the velocities, a signal-to-noise ratio (S/N) per Å larger than 7 and errors lower than 50 km/s, while for the metallicities we further required a S/N per Å larger than 10 (see Battaglia et al. 2008b), errors lower than 1 dex and negative values for the equivalent widths (EW) of both second and third CaT lines (we exclude the first one since it is not used in the EW−[Fe/H] relation we adopt; see below). As a result, this clean catalogue contains 335 entries, from which a total of 133 members were detected by summing all the membership probabilities from the EM algorithm. Figure 4.9 displays the spatial distribution of the resulting membership probabilities, while Fig. 4.10 shows their distribution in metallicity versus velocity.

Table 4.3 is a sample from the generated spectroscopic catalogue. For each object the catalogue contains the celestial coordinates, the heliocentric velocity, the metallicity, and the membership probabilities we derived. The metallicity and its error were derived as in Battaglia et al. (2011), from the CaT region adopting the calibration of Starkenburg et al. (2010), using the $V$ magnitudes derived with the $(g-r) \rightarrow (V-g)$ equations of Jordi et al. (2006) applied to the $g$ and $r$ magnitudes of our MegaCam photometric catalogue.

The means and standard deviations fitted by the EM algorithm for the velocities and metallicities of UMi are $\overline{\mathrm{v}}_{hel} = -243 \pm 1$ km/s ($-242.7$ km/s in Kirby et al. 2011), $\sigma(\mathrm{v}_{hel}) = 9.7 \pm 0.8$ km/s ($9.5 \pm 1.2$ km/s in Walker et al. 2010), $\overline{[\mathrm{Fe/H}]} = -2.17 \pm 0.05$ ($-2.13 \pm 0.01$ in Kirby et al. 2011) and $\sigma([\mathrm{Fe/H}]) = 0.35 \pm 0.04$ (0.34 in Kirby et al. 2011). Figure 4.11 further shows

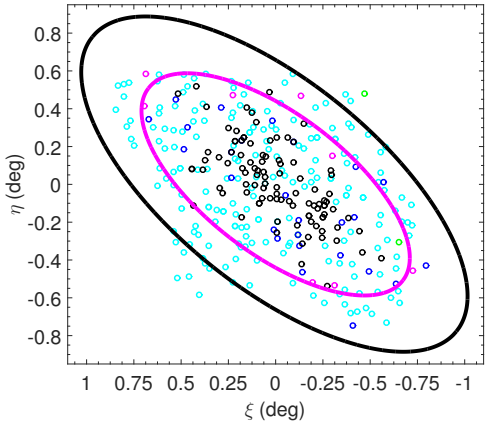


Figure 4.9: Location of stars from the spectroscopic sample along the line-of-sight to UMi. Colour-coded using the membership probabilities calculated in this work, with black, blue, magenta, red, green and cyan markers denoting $P_i \geq 0.99$, $> 0.95$, $> 0.68$, $> 0.50$, $> 0.01$, $> 0.00$, respectively. The pink and black ellipses show the nominal King tidal radius with parameters from IH95 and this work, respectively.

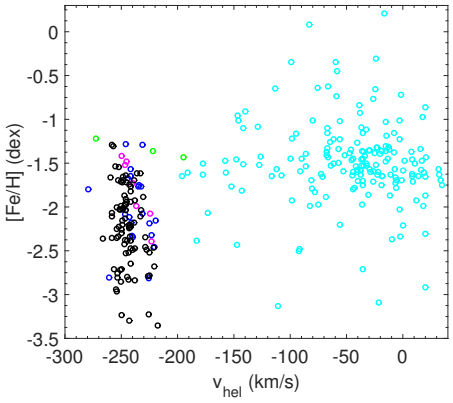


Figure 4.10: Distribution in metallicity vs. heliocentric velocity of the spectroscopic sample of UMi. Colour-coded using the membership probabilities calculated in this work, with black, blue, magenta, red, green and cyan markers denoting $P_i \geq 0.99$, $> 0.95$, $> 0.68$, $> 0.50$, $> 0.01$, $> 0.00$, respectively.

| $\alpha_{2000}$ (hh:mm:ss) | $\delta_{2000}$ (dd:mm:ss) | $v_{hel}$ (km $s^{-1}$) | [Fe/H] (dex) | P |
|---|---|---|---|---|
| 15:07:40.14 | 67:15:31.1 | -227.48±5.58 | $-2.49^{+0.22}_{-0.25}$ | 0.999 |
| 15:13:56.43 | 66:51:46.1 | -30.13±3.88 | $-1.35^{+0.13}_{-0.13}$ | 0.000 |
| 15:13:30.32 | 67:06:36.9 | -228.53±2.33 | $-2.46^{+0.07}_{-0.07}$ | 0.996 |
| 15:16:18.05 | 67:37:47.2 | -246.87±5.03 | $-1.52^{+0.16}_{-0.16}$ | 0.876 |
| 15:02:29.39 | 66:50:15.1 | -33.73±2.28 | $-1.42^{+0.06}_{-0.06}$ | 0.000 |
| 15:02:21.79 | 66:54:43.3 | -222.05±6.57 | $-1.36^{+0.26}_{-0.26}$ | 0.266 |
| ... | ... | ... | ... | ... |

Table 4.3: Sample from the spectroscopic catalogue of UMi with the obtained probabilities of membership. $v_{hel}$ is the heliocentric velocity and P is the membership probability.

that the metallicities are spatially well-mixed, with no radial gradient across the galaxy, as Carrera et al. (2002), Kirby et al. (2011) and Jin et al. (2016) already proved. Although the first two works were based on spectroscopic datasets that only covered out to approximately the half of the maximum elliptical radius reached here, the latter used the same dataset as us. However, Jin et al. (2016) did not calculate the probabilities of membership of the different stars nor use any other technique to decontaminate the sample or model its spatial, kinematic or chemical distributions, apart from just applying a hard-cut around ±50 km/s of the systemic heliocentric velocity of UMi to separate members from contaminants. The lack of a metallicity gradient on a MW dSph is something very unusual and could indicate that UMi has been tidally disturbed by the MW, as tidal interactions can erase a non-uniform metallicity distribution (Sales et al. 2010). Unfortunately, with regard to the over- and underdensities discussed in Section 4.4, they were not sufficiently sampled to allow their spectroscopic study, with no more than two spectroscopic targets observed in the most sampled ones.

In order to further check if the velocity distribution of the high probable members ($P_i > 0.99$) is Gaussian, we first converted their LOS velocities in the heliocentric rest frame (HRF) into the dwarf galaxy rest frame (DRF) as in Section 3.3, that is by using Eq. 4 of Walker et al. (2008) and the transformations derived in their appendix, together with our fitted systemic velocity of -243 km/s and the HRF proper motion of UMi measured in Fritz et al. (2018). These DRF velocities are plotted in Fig. 4.12, while Fig. 4.13 shows their LOS velocity dispersion profile, calculated with the EM algorithm.

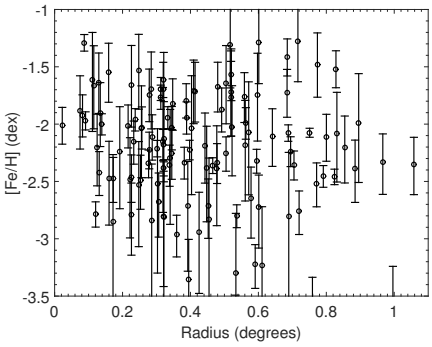


Figure 4.11: Metallicity as a function of elliptical radius for those UMi targets with a membership probability larger than 68%. No metallicity gradient is observed across the galaxy.

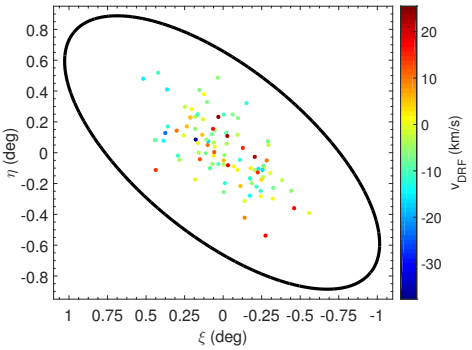


Figure 4.12: Location of the high probable members ($P_i > 0.99$) from the spectroscopic sample along the line-of-sight to UMi. Colour-coded according to the LOS velocities in the dwarf galaxy rest frame calculated in this work. The black ellipse show the nominal King tidal radius with parameters from this work.

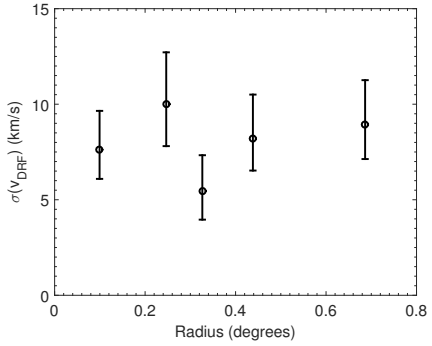


Figure 4.13: LOS velocity dispersion as a function of elliptical radius of those UMi targets from Fig. 4.12 (20 stars used per bin). No gradient in the velocity dispersion is observed across the galaxy.

Figure 4.13 further shows that no radial gradient is observed across the galaxy in the velocity dispersion, as found by Walker et al. (2010) from a completely independent sample.

We then proceeded as in Section 3.3: to take into account that the shape of this velocity distribution is affected by the errors in the measurements, we randomly extracted numerous resamples from the distribution convolved by the measurement errors, each with the same number of members as the original sample, and performed an Anderson-Darling test to each of them. As a result, we obtained an unlikely probability for UMi members of being extracted from a Gaussian velocity distribution (median p-value $< 0.03$). While this fact does not necessarily imply that the stellar population is out of dynamical equilibrium, it appears indicative of complex kinematics, which could potentially be caused by some of the stellar over- and underdensities detected, like the north-east clump in which Kleyna et al. (2003) and Pace et al. (2014) discovered a cold substructure.

## 4.6 Summary and conclusions

We present results from CFHT/MegaCam deep $g-$ and $r-$band photometry of the UMi dSph out to a radius of $\sim 1$ deg, covering approximately 4 deg$^2$ and reaching $\sim 2.5$ magnitudes below the oldest main-sequence turn-off, which yields the most spatially extended and deep photometric dataset of the galaxy with respect to those in the literature.

We obtained the most accurate structural parameters to date of the UMi dSph (Table 4.2) by fitting different surface density profiles with a Bayesian MCMC sampling of the likelihood evaluated at the individual stellar locations. We find overall agreement with the structural parameters derived in previous studies and the posterior Bayes factor establishes that the Plummer profile is the best-fitting model over the King, Sérsic and exponential profiles.

We decontaminated the two-dimensional spatial distribution of UMi overall stellar population by making use of an improved version of the McMonigal et al. (2014) matched-filter method (Sect. 2.4) and an alternative decontamination method acting on the individual point-sources without requiring spatial binning (Appendix B.1). The outer parts of UMi displays a fairly regular distribution with no significant distortions nor tidal tails down to a surface brightness limit of $\sim 32$ mag/arcsec$^2$ in V-band. Although UMi has a pericentric distance around the MW small enough to be at risk of being strongly tidally affected when close to its pericentre (Fritz et al. 2018), at the present time it is located almost at the apocentre of its quite eccentric orbit (Fritz et al. 2018; Gaia Collaboration et al. 2018) and the time elapsed from its last

pericentric passage (Gaia Collaboration et al. 2018) is dozens of times larger than its internal dynamical timescale, so that UMi is expected to have relaxed back to equilibrium since then, erasing any signs of tidal tails/debris. If UMi indeed gets tidally disturbed when being close to its pericentre, to then relax back to equilibrium during the rest of its journey along its quite eccentric orbit until its next pericentric passage, this may be the reason of its well-mixed metallicities with no radial gradient across the galaxy, as Jin et al. (2016) noted that the metallicity gradient of a dwarf galaxy can be easily erased through the tidal interactions with its host galaxy, in this case the MW. With regard to its relatively high ellipticity, which one could interpret as tidal "stretching", there are other MW dSphs whose pericentric distances are too large to allow any tidal disturbance from the MW while their ellipticities are similar or even considerably higher to the one of UMi (Fritz et al. 2018; McConnachie 2012), such as Ursa Major ($\epsilon = 0.80$). Thereby, their high ellipticities are thought to be a consequence of their velocity anisotropies instead of tidal interactions. In addition, the relatively high value of the ellipticity of UMi could also be due in part to a mere projection effect. As we measure the projected ellipticity and this is the minimum possible value of the real one, those galaxies whose spatial orientation maximize their projected ellipticity will present higher ellipticities, and UMi could be one of these cases. Furthermore, although the pericentric distance of its twin dSph Draco (Bellazzini et al. 2002) is even smaller for a very similar eccentricity of its orbit (Gaia Collaboration et al. 2018), its projected ellipticity is considerably lower ($\epsilon = 0.31$) and a clear radial gradient is observed in its metallicities (Jin et al. 2016). Thus, it is improbable that the relatively high ellipticity of UMi and the lack of a radial gradient in its metallicities could result from its tidal interaction with the MW, given the absence of these features in its twin dSph Draco despite its closer pericentric distance and similar eccentricity of its orbit.

We obtained the 2D distribution of residuals with respect to the fitted surface density axisymmetric models, detecting several over-dense and under-dense clumps with statistical significances larger than $3\sigma$ from which we identify an overdensity in the northeast side of the galaxy that corresponds to the one revealed in the surface density maps of IH95 and Bellazzini et al. (2002), where Kleyna et al. (2003) then detected a cold kinematic signature also confirmed by Pace et al. (2014); Kleyna et al. (2003) argued that this clump is consistent with being the remnant of a disrupted stellar cluster. We also detect an already discovered stellar cluster that does not belong to UMi (Muñoz et al. 2012) in the west side of our coverage. Likewise, we identify a central overdensity that could also be caused by a possible central black hole, which was originally suggested by Strobel & Lake (1994) and later detected first in radio (Maccarone et al.

2005) and then in X-rays (Nucita et al. 2013), and whose minimum mass would be in the range $5 \cdot 10^4 M_\odot - 5 \cdot 10^5 M_\odot$ (Nucita et al. 2013). With regard to the new overdensities detected in the southwest side of the galaxy, they are probably more remnants from the disrupted stellar cluster that could produce the northeast clump, while the inner under-dense region is caused by a marked core in the inner regions of UMi stellar density profile.

Finally, we analysed the spectroscopic catalogue of UMi from the preliminary work of Jin et al. (2016) with an improved form of the decontamination method developed by W09, which allows us to also calculate the membership probabilities of its different targets. The means and standard deviations fitted for the velocities and metallicities of the UMi members are $\overline{\mathrm{v}}_{hel} = -243 \pm 1$ km/s (in agreement with Kirby et al. 2011), $\sigma(\mathrm{v}_{hel}) = 9.7 \pm 0.8$ km/s (in agreement with Walker et al. 2010), $\overline{[\mathrm{Fe/H}]} = -2.17 \pm 0.05$ dex (in agreement with Kirby et al. 2011) and $\sigma([\mathrm{Fe/H}]) = 0.35 \pm 0.04$ dex (in agreement with Kirby et al. 2011). On the other hand, no radial gradient was detected across the galaxy either on the individual metallicities or in the velocity dispersion, as Jin et al. (2016) and Walker et al. (2010) already found. Regarding the stellar over- and underdensities here detected, they were not sufficiently sampled to allow their spectroscopic study, reason why their stars are of particular interest for future spectroscopic studies of UMi. We also converted the heliocentric LOS velocities of the high probable members into the dwarf galaxy rest frame and checked that their distribution is unlikely to be Gaussian. While this fact does not imply that the system is not in dynamical equilibrium, it would be indicative of complex kinematics probably caused by some of the over- and underdensities detected in this work, like the northeast clump in which a cold substructure was detected by Kleyna et al. (2003) and Pace et al. (2014).

# 5

# Eridanus II and its candidate star cluster

**(incl. L. Cicuéndez)**

Paper in preparation

**ABSTRACT**

We used very deep photometric observations of the central regions of the Eridanus II (Eri II) dwarf spheroidal galaxy (dSph), in order to better characterize the structural parameters of a candidate star cluster recently reported in the literature. To that end we applied a Bayesian Markov chain Monte Carlo (MCMC) method to the individual stars' positions. We provide the fitted structural parameters for the region where the cluster would be located, which turn out to be all compatible with the ones of Eridanus II. Furthermore, the available observational evidence and a fitted ellipticity of $\epsilon = 0.4$, which would make this cluster the most elliptical one known to date with all the rest having $\epsilon < 0.3$, suggest this would be a very unusual star cluster.

## 5.1 Introduction

Recently the presence of a central overdensity was reported in the Eri II dSph and interpreted as a stellar cluster (Crnojević et al. 2016, hereafter CR16), which would make Eri II the faintest galaxy ($M_V = -7.1$, CR16) known to host a cluster. The presence of a stellar cluster in such a faint galaxy can have important implications for the ΛCDM cosmological model of structure formation. This model predicts galactic dark matter (DM) halos characterized by central cusps whose density diverges as $\rho \propto r^{-1}$ (e.g. Dubinski & Carlberg 1991; Navarro et al. 1996), but according to Contenta et al. (2018) the existence of this cluster would favour a cored DM halo in Eri II over a cusped one. This is because a cusped DM halo would require the star cluster

to lie extremely far from of Eri II's centre ($> 1$ kpc), with a high inclined orbit being observed at a specific orbital phase to have been able to survive for more than 5 Gyr (since its age is consistent with $\simeq$ 10 Gyr; Amorisco 2017, and no stars younger than 5 Gyr have been observed; Contenta et al. 2018) or, as Amorisco (2017) showed, that the cluster formed at rest at the centre of the potential. This last scenario could be checked by measuring the proper motion of the cluster within the galaxy, which does not appear possible with current data. The presence of such cluster would also provide strong constraints on the existence of massive compact halo objects (MACHOs) with masses larger than $\sim 5M_{\odot}$ (Brandt 2016). MACHO dark matter would dynamically heat the star cluster, dissolving it into Eri II in less than 3 Gyr. In addition, should the nature of this central overdensity be confirmed to be a stellar cluster, it would extend the empirical relationship between the number of globular clusters hosted by a galaxy and the total mass of the galaxy itself (corresponding to a frequency of 0.06 - 0.39 clusters per $10^9 M_{\odot}$ of total mass) about two orders of magnitude below the previous limit in stellar mass (Zaritsky et al. 2016). Furthermore, using a subhalo mass function from literature high-resolution numerical simulations and populating the Milky Way (MW) subhalos with masses smaller than $10^{10} M_{\odot}$ with the aforementioned empirically constrained frequency from Eri II, Zaritsky et al. found that $\sim 90\%$ of the DM halos that could potentially host globular clusters are less massive than that of Eri II. With this mass-normalized cluster specific frequency and the available evidence about the stellar mass - halo mass function and the subhalo mass function, they further conclude that some of the star clusters in the MW's outer halo could be within undetected halos with extremely faint stellar counterparts.

Motivated by the report of this stellar cluster in Eri II, we used photometric observations obtained by C. Gallart and J.D. Simon, much deeper than CR16 ones, to better characterize its structural parameters. The chapter is organized as follows: Section 5.2 presents the details of our observations, in Sect. 5.3 we derive the structural parameters of the candidate cluster, and Sect. 5.4 is dedicated to the discussion and conclusions of this work.

## 5.2 Observations and data reduction

In this study we analyzed two independent photometric datasets: the one presented in CR16, spatially extended, and the deeper one covering only the central regions. With regard to the former, it consists of a catalogue of point-sources from a Megacam pointing from the Magellan Clay telescope, with deep g and r photometry (covering near $\sim 24' \times 24'$ and reaching out to $\sim 2$ mag below the oldest main-sequence turn-off). We refer the reader to CR16 for more details.

Our deeper photometric data for the central regions of Eri II ($\sim 200'' \times 200''$) were instead obtained with the ACS/WFC (Ford et al. 1998) aboard the Hubble Space Telescope (HST) in September 22 and 23 2016 under the program GO#14224 (P.I. C. Gallart) in cycle 23. The observations were designed to obtain a signal-to-noise ratio $\sim 40$ near the magnitude level of the oldest main sequence turnoff (oMSTO), at $M_{F814W} \sim +2.75$. Under this program, the galaxy was observed during six orbits, organized in two visits of three orbits each. The available exposure time was distributed almost evenly in $F475W$ and $F814W$, and short and long exposures were taken in order to increase the dynamical range of our colour-magnitude diagram. In this way, we reach the oMSTO with good photometric accuracy and precision, while maintaining unsaturated the stars at the tip of the Red Giant Branch (RGB). The total exposure time devoted to Eri II was 7,644 s in $F475W$ and 7,900 s in $F814W$.

Another ACS/WFC program was devoted to image the same galaxy in cycle 23. GO#14234 (P.I. J.D. Simon) used 13 orbits to observe the central regions of Eri II between January 16 and February 6 2016. 16 exposures were collected in the $F606W$ band and 10 in the $F814W$ filter, with individual exposure times ranging from 1,220 s to 1,390 s. The total integration time was therefore of 12,830 s and 20,680 s, respectively.

The data reduction was performed by M. Monelli using the DAOPHOT IV/ALLFRAME suite of code (Stetson 1987, 1994), following the prescriptions of Monelli et al. (2010). Briefly, images are individually treated to derive optimal point spread functions based on bright stars, unaffected by cosmic rays and distributed over the full field of view to take into account the spatial variations. Original FLT images from the HST archive pipeline were used. The list of sources inputed to ALLFRAME was generated on stacked median image. This ensures that most, if not all, cosmic rays are filtered out and do not pollute the object lists. Visual inspection of the images revealed the presence of a large number of background extended objects in both the whole field-of-view and the region of the candidate star cluster in particular. Most of them have been efficiently removed using the SHARPNESS parameter ($|\mathrm{SHARPNESS}| < 0.1$). The final selected photometric catalogue was calibrated to the VEGAMAG system using the latest zero points available on the ACS web page.

Given the rotation of $\sim 121^\circ$ between the two ACS/WFC datasets, these have been independently reduced, and cross-matched a posteriori, after correcting the coordinate system for geometric distortion. The final list includes 19,830 bonafide stars: 12,152 are in common between the $F475W$ and the $F814W$ filters, and 15,693 are detected in the $F606W$ and in the $F814W$ bands.

## 5.3 Structural parameters

We first checked the structural parameters of Eri II derived in CR16, in order to use them to model the background contamination of the candidate cluster when fitting its structural parameters. Thus, we fitted an exponential function to their more spatially extended dataset, as they did, plus a uniform distribution of contaminants. To derive the structural parameters of the galaxy we followed the same methodology of Sect. 2.3 based on Richardson et al. (2011), that is by evaluating with 'The MCMC Hammer' (Foreman-Mackey et al. 2013) at the individual stellar locations a likelihood expression depending on the surface density profile to be fitted as well as on the position angle, ellipticity, etc.

We confirm the validity of the structural parameters of Eri II derived in CR16 as all our fitted values were compatible with theirs within $2\sigma$. While for comparison purposes we fitted an exponential profile, if instead we were to fit a Plummer model, as it has the same number of free parameters, all the fitted values of the structural parameters would be the same as in our exponential fit. Indeed, in Fig. 5.1 we can see that a Plummer model gives a satisfactory representation of the observed surface number density profile of Eri II. In addition, CR16 remarked that the fitted values of the structural parameters of the galaxy remain the same regardless the stellar cluster is masked or not.

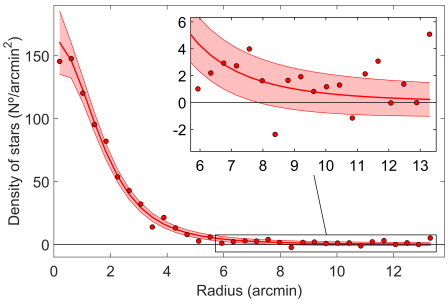


Figure 5.1: Contamination subtracted surface number density profile of Eri II stars as a function of the major axis radius (with the external parts zoomed in) from the CR16 dataset, overlaid onto the $1\sigma$ confidence interval (red band) of the best-fitting Plummer profile obtained with the MCMC Hammer. The possible stellar cluster would be at the second inner point. The $1\sigma$ confidence interval is computed from the best-fitting model assuming Poisson variances in each elliptical annulus. We do not use a logarithmic scale so as to be able to show the density fluctuations below the estimated background (negative values); otherwise plots mimic the presence of extra-tidal stars.

We then used our deeper dataset, covering a much smaller portion of the galaxy, to fit the surface density profile of the candidate star cluster by modeling

its background contamination density as the already fitted profile of Eri II plus a uniform distribution to account for contamination by foreground MW stars. Table 5.1 shows the structural parameters obtained for the cluster and Fig. 5.2 their Bayesian posterior distributions. The resulting structural parameters show that Eri II and its candidate star cluster share the same centre, ellipticity and position angle (considering their respective error bars), while there is no reason why they should coincide. This led us to think that we were probably just fitting the central cusp of the stellar surface density profile of Eri II.

| Parameter | Eridanus II (CR16) | Eridanus II (this work) | Cluster (CR16) | Cluster (this work) |
|---|---|---|---|---|
| $\alpha_{2000}$ (º) | $56.08^{+0.05}_{-0.05}$ | $56.085^{+0.005}_{-0.005}$ | $56.093^{+0.005}_{-0.005}$ | $56.0933^{+0.0002}_{-0.0002}$ |
| $\delta_{2000}$ (º) | $-43.534^{+0.002}_{-0.002}$ | $-43.533^{+0.002}_{-0.002}$ | $-43.5331^{+0.0006}_{-0.0006}$ | $-43.5334^{+0.0001}_{-0.0001}$ |
| Ellipticity | $0.48^{+0.04}_{-0.04}$ | $0.43^{+0.03}_{-0.04}$ | - | $0.40^{+0.06}_{-0.06}$ |
| Position angle (º) | $73^{+4}_{-4}$ | $78^{+3}_{-3}$ | - | $74^{+6}_{-6}$ |
| 2D half-light $r_h$ (′) | $2.3^{+0.2}_{-0.2}$ | $2.4^{+0.2}_{-0.2}$ | $0.11^{+0.01}_{-0.01}$ | $0.20^{+0.02}_{-0.02}$ |

Table 5.1: Structural parameters derived in this work and CR16 for Eri II and its candidate cluster when modelling the surface number density as an exponential profile. The 2D half-light radius $r_h$ from this work was derived using the formula in Wolf et al. (2010).

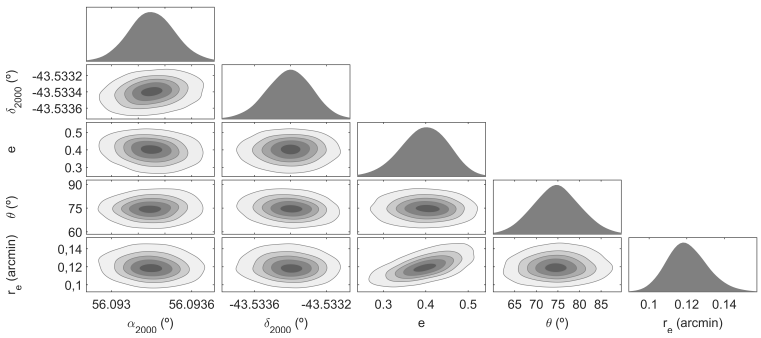


Figure 5.2: Bayesian posterior distributions of the structural parameters from the candidate star cluster in Eri II, obtained with the MCMC Hammer from our dataset when modelling its surface number density as an empirical exponential profile. Contours contain 10%, 30%, 50%, 70% and 90% of the points sampled by the MCMC Hammer. From left to right: RA ($\alpha_{2000}$), DEC ($\delta_{2000}$), ellipticity ($e = 1 - b/a$), position angle ($\theta$) and exponential radius ($r_e$). Two-dimensional normal distributions aligned with x- and y-axes are indicative of uncorrelated parameters.

## 5.4 Discussion and conclusions

By analyzing two different photometric datasets of Eri II, we have shown that all the structural parameters of its candidate star cluster would be compatible with the ones of the galaxy itself. Hence the central cluster reported in CR16 could be just the innermost part of Eri II, which corresponds to the densest region of the galaxy. Besides, if this stellar cluster would exist, both Eri II and the hosted cluster would be unique for numerous reasons. First of all, Eri II would be the faintest galaxy hosting a stellar cluster up to date, which in addition would be one of the most extended ones, with a half-light radius here derived of $r_h = 21.3$ pc (assuming a distance of $366 \pm 17$ kpc; CR16) while at most they have $r_h \sim 20$ pc. Second, this half-light radius together with its absolute magnitude $M_V = -3.5$ (CR16) 'places the cluster in a similar parameter space to the least luminous and most compact MW ultrafaint dwarfs' (CR16), not to the globular clusters (see top panel in Fig. 6 of McConnachie 2012). Third, it would be also a candidate nuclear cluster, while any of the clusters in the satellite dwarf galaxies of the MW or M31 is a nuclear one, and beyond the LG a deep study of the Fornax galaxy cluster (Muñoz et al. 2015) found no galaxies with $M_V > -10$ (Eri II has $M_V = -7.1$; CR16) holding a nuclear star cluster.

Furthermore, the colour-magnitude diagram of the star cluster would be indistinguishable from the one of the galaxy (see the bottom panel in Fig. 4 of CR16) and CR16 noted that all the structural parameters of Eri II they obtained remain the same regardless the candidate star cluster is masked or not. This implies that either its contribution is very small, or its spatial distribution is not very different from the one of the galaxy. Finally, while CR16 did not calculate the ellipticity of the cluster because it seemed visually round before reducing their photometric data, after reducing our deeper dataset it is clearly elliptical ($\epsilon = 0.4$), which further leads to a considerably larger fitted value of its half-light radius ($r_h = 21.3$ pc in this work vs. $r_h = 13$ pc in CR16). Its ellipticity though, while typical for a dwarf galaxy (see ellipticities of dwarfs e.g. in McConnachie 2012), is so high for a globular cluster that this would become the most elliptical globular cluster discovered till the date, with all the rest having $\epsilon < 0.3$ (see the most complete catalogs with ellipticities of globular clusters in the MW, Harris 2010; M31, Staneva et al. 1996 and LMC, Goodwin 1997).

All these reasons suggest that this object, instead of being an actual stellar cluster, might be just the central cusp of the stellar density profile of Eri II.

Nevertheless, since we cannot completely exclude that it would indeed be a very unusual star cluster, we remind that Table 5.1 provides the best fitting structural parameters derived in this work of the region where it would be located.

# 6

# Conclusions

In this thesis we have studied the global structure of a sample of dwarf spheroidal galaxies (dSph) satellites of the Milky Way (MW) and uncovered the presence of several internal substructures in these systems. The galaxies analyzed are Sextans, Ursa Minor (UMi) and the recently discovered Eridanus II (Eri II). To that end, we mainly studied the spatial distribution of their stellar component, from very wide-area photometric samples of large numbers of individual stars, but also the distributions on metallicity and line-of-sight (LOS) velocity for the sub-sets of stars with spectroscopic measurements. In the following we summarize the main conclusions derived for each chapter of this thesis.

## 6.1 Tracing the stellar component of low surface brightness Milky Way Dwarf Galaxies to their outskirts I: Sextans

Chapter 2 was devoted to the study of the Sextans dSph. We obtained very spatially extended and deep CTIO/DECam $g$ and $r$ photometry (out to a radius of $\sim 4$ deg and reaching $\sim 2$ magnitudes below the oldest main-sequence turn-off) and publicly released the corresponding reduced catalogue of point-like sources. The main outcomes were the following:

- We updated the structural parameters of the dSph and found that the galaxy is significantly less extended than previous studies suggested. We showed that the structural parameters retrieved for this system depend on the magnitude cut adopted, yielding a more concentrated and rounder spatial distribution when adopting a deeper magnitude cut.

- We decontaminated the surface density map of Sextans overall stellar population. No signs of tidal disturbance were found down to a surface brightness of $\sim 31.8$ mag/arcsec$^2$ in V-band, while we revealed some over-dense and under-dense clumps.

- For the first time, we obtained the structural parameters and decontaminated surface density maps of the red and blue Horizontal Branch stars (RHB and BHB, respectively) and bright and faint Blue Stragglers (BSs). No significant distortions were found for any of these populations, but the BHB stars were found to be considerably more extended than the rest of evolutionary phases, which is consistent with the age and metallicity gradient determined in the literature. Although we also confirmed that bright BSs are less spatially extended than the faint ones, their different spatial distributions appear compatible with the bulk of Sextans BSs having evolved from mass transfer of primordial binaries and not necessarily by the disruption of a globular cluster, as suggested in the literature.

- Finally, we updated the membership probabilities of two literature spectroscopic catalogues, making them publicly available to facilitate subsequent studies of the internal properties of Sextans, as the one performed in Chapter 3.

## 6.2 Appearances can be deceiving: clear signs of accretion in the seemingly ordinary Sextans dSph

In Chapter 3 we dealt with the discovery of clear observational signs of past accretion/merger events in Sextans. Using the same photometric catalogue and the high probable spectroscopic members from Chapter 2, the major findings were these:

- A clearly different spatial distribution for the blue and red Red Giant Branch (and Main-Sequence Turn-Off) stars, which is almost round and regular for the former, but much more elliptical and asymmetric for the latter, which further exhibits a distinct 'shell-like" overdensity in the northeast side. Such features are difficult to explain in a scenario where Sextans evolved undisturbed by external events. Comparison with isochrones and spectroscopic metallicities showed that blue stars are on average more metal-poor than the red stars.

- Although in Chapter 2 the dependence of the structural parameters on the adopted magnitude cut could not be traced back to any obvious difference in the stellar population mix as a function of magnitude, in this chapter we found that this is due to a variable proportion of the aforementioned blue versus red stars having distinct spatial distributions. This ratio was found to be higher at the deepest magnitudes. Thus, we could confirm that the structural parameters derived for Sextans do depend on the adopted magnitude cut.
- A "ring-like" spatial feature on both the LOS velocities and metallicities, with a considerably larger systemic velocity and lower metallicity than the rest of stars, and a non-Gaussian LOS velocity distribution.

We interpreted these features as very likely due to an accretion/merger event. These kind of anomalies have been already seen in larger systems with on-going accretion events and, while the smallest galaxy with univocal signs of accretion up to date was the Andromeda II dSph, with a stellar mass of $\sim 10^7 M_\odot$, now Sextans, with a stellar mass of just $\sim 5 \times 10^5 M_\odot$ (i.e. $\sim 5\%$ of the one of And II), thus becomes the smallest galaxy with clear observational signs of accretion to date.

## 6.3 Tracing the stellar component of low surface brightness Milky Way Dwarf Galaxies to their outskirts II: Ursa Minor

In Chapter 4 we studied UMi from wide-area CFHT/MegaCam $g$ and $r$ deep photometry (covering $\sim 4$ deg$^2$ and reaching out to $\sim 2.5$ magnitudes below the oldest main-sequence turn-off). Taking advantage of the tools developed in the previous chapters, we applied to UMi an analysis similar to the one performed in Chapter 2 on Sextans:

- We updated the structural parameters of the overall stellar population of UMi and found overall agreement with the structural parameters derived in previous studies. The Plummer model is strongly favoured as the best-fitting surface density profile over the King, Sérsic and exponential models.
- We decontaminated the two-dimensional spatial distribution of UMi overall stellar population. The outer parts of the dwarf displays a fairly regular distribution with no tidal disturbances down to a surface brightness limit of $\sim 32$ mag/arcsec$^2$ in V-band. However, we did detect some internal overdensities that could result from a disrupted stellar cluster. Nevertheless, we further detected one stellar overdensity close to the galactic

centre that could also result from a plausible central black hole often investigated in the literature, with reported detections in both X-rays and radio.

- Finally, we analysed the metallicity and LOS velocity distributions from a literature spectroscopic catalogue of UMi, calculating the membership probabilities of its different targets. No radial gradients were found either on the individual metallicities or in the velocity dispersion. We also checked that the distribution of the LOS velocities of the high probable members in the dwarf galaxy rest frame is unlikely to be Gaussian. While this fact does not imply that the system is out of dynamical equilibrium, it could be caused by some of the stellar clumps detected in this work.

### 6.4 Eridanus II and its candidate star cluster

Finally, Chapter 5 was about Eri II and its candidate star cluster whose presence was recently reported in Crnojević et al. (2016). We used very deep Magellan Clay/MegaCam and ACS/WFC photometry in order to better characterize the structural parameters of the putative cluster. The main results were these:

- The structural parameters of the putative cluster turned out to be all compatible with the ones of Eri II. Hence the central cluster reported in CR16 could be just the innermost part of Eri II, which corresponds to the densest region of the galaxy.
- Additional observational evidence and a fitted ellipticity of $\epsilon = 0.4$, which would make this cluster the most elliptical one known to date with all the rest from the literature having $\epsilon < 0.3$, suggest it would be a very unusual star cluster in case it would not be just the central cusp of the surface density profile of Eri II.
- Since we could not completely rule out that it would indeed be a very unusual star cluster, we still provided the best fitting structural parameters derived in this work for the region where it would be located.

# 7

# Future prospects

In this thesis we have searched for possible tidal tails caused by the interaction between the studied dSphs and the MW, as they would indicate departure from dynamical equilibrium, which is required for the correct estimates of the dark matter halo properties. However, we have not found them down to $\sim 32$ mag/arcsec$^2$ in V-band. The greatest contribution of the ESA's Gaia space telescope to the study of MW dwarf galaxies in this respect has been its recently released measurements of their stellar proper motions from which to infer the systemic ones. These systemic proper motions have allowed the determination of at least their last orbit around the MW, and thus their pericentric and apocentric distances and times elapsed since their last pericentric passage (Fritz et al. 2018; Gaia Collaboration et al. 2018). In this way, the pericentric distances of Sextans and Eri II (larger than 70 kpc and 350 kpc, respectively) have turned out to be too large to cause appreciable signs of tidal disturbances in these dSphs (see e.g. the N-body simulations of Sales et al. 2010), although the pericentric distance of UMi (between 30 kpc and 45 kpc) has resulted to be rather lower. Despite this, even in the case of UMi, the time elapsed from its last pericentric passage (Gaia Collaboration et al. 2018) is dozens of times larger than the crossing time within its half-light radius. Thus, UMi is expected to have relaxed back to equilibrium since then, erasing any signs of a possible past tidal interaction with the MW as well. Therefore, for future searches of tidal tails/debris in dwarf galaxies caused by their interaction with the MW, basing on their lowest pericentric distances (reaching within 20 kpc) derived with the Gaia proper motions, the best candidates as of today are Tucana III, Sagittarius I, Hercules I, Draco II, Crater II, Triangulum II, Segue 1 and Will-

man 1 (Fritz et al. 2018). Among these, no signs of tidal disturbance have been detected yet in the latter three systems, which could be due in part to the difficulty in detecting tidal features in very faint systems and/or the errors in their pericentric distances.

We have also proved that accretion or merger events can take place even at the mass scale of dSphs as small as Sextans. As we have checked, these events can have a huge impact on the structural properties of the affected dwarfs, such as their structural parameters or the presence of internal substructures, but also on their metallicities and kinematics, perhaps even placing them out of dynamical equilibrium. The particular case of Sextans also lowers the faint end of the galaxy mass function at which some predictions of the hierarchical theory of galaxy formation have been qualitatively verified. Notwithstanding, there are still some issues about its accretion/merger event such as the origin of the asymmetric, clumpy and redder/more metal-rich component given the lower metallicity of the "ring" feature, as it could be the remnant of an accreted object more metal-poor than Sextans, in agreement with the luminosity-metallicity relation. Besides, in case the young component originated *in-situ*, the star formation history and chemical properties of Sextans, compatible with it being a fossil from the pre-reionization era (Revaz & Jablonka 2018; Bettinelli et al. 2018), make it hard to understand how the clumps and asymmetries could have survived for such a long time. Dedicated simulations taking into account the wealth of available observational information will be needed to address these issues. On the other hand, could there be other MW satellites of similar or even lower mass still affected by a past accretion/merger event? Clearly, in order to check this, additional very deep and wide area photometry and spectroscopy of other MW dwarfs, together with the subsequent careful decontamination of the datasets, will be required. In this respect, future wide-field multi-object spectrographs such as WEAVE, 4MOST and DESI will be of particular interest.

We have also seen that the inner over-dense clumps such as the ones detected in the UMi dSph can correspond to cold kinematic substructures that could result, for example, from a disrupted stellar cluster. To check if this is indeed the case, stars forming part of these over-dense clumps are of particular interest for future spectroscopic studies, in order to assess possible differences in their metallicity and LOS velocity with respect to those from the host galaxy. In the same way, dedicated simulations taking into account all the collected information will be required to assess their possible origin, and in the particular case of UMi, to reveal if all the detected substructures could share a common origin. All this also applies to the particular case of Eri II and its candidate star cluster, in order to check if it could be just the central cusp of the galactic surface density profile, and if not, to investigate its possible origin.

Finally, with regard to the new datasets of MW dwarfs from the Big Data Archive of Gaia, applying some of the Bayesian tools used in this thesis such as the EM algorithm but including the new information from the measured proper motions and parallaxes will increase the precision of the results, due inter alia to much more constrained membership probabilities of the spectroscopic targets. These proper motions and parallaxes will be particularly important for decontaminating the ultrafaint dwarf galaxies due to their very small number of spectroscopic targets, in which the inclusion of just a few contaminants can have a huge impact on the kinematic and chemical properties derived for these dwarfs, leading to even mislead globular clusters with ultrafaint dwarfs.

# Bibliography

Aitkin, M. 1991, J. R. Stat. Soc. B, 53, 111

Alam, S., Albareti, F. D., Allende Prieto, C., et al. 2015, ApJS, 219, 12

Albareti, F. D., Allende Prieto, C., Almeida, A., et al. 2017, ApJS, 233, 25

Amorisco, N. C. 2017, ApJ, 844, 64

Amorisco, N. C., & Evans, N. W. 2012, ApJ, 756, L2

Amorisco, N. C., Evans, N. W., & van de Ven, G. 2014, Nature, 507, 335

Aparicio, A., & Gallart, C. 2004a, AJ, 128, 1465

—. 2004b, AJ, 128, 1465

Bailyn, C. D. 1995, ARA&A, 33, 133

Bailyn, C. D., & Pinsonneault, M. H. 1995, ApJ, 439, 705

Bate, N. F., McMonigal, B., Lewis, G. F., et al. 2015, MNRAS, 453, 690

Battaglia, G. 2007, PhD thesis, Kapteyn Astronomical Institute, University of Groningen

Battaglia, G., Helmi, A., & Breddels, M. 2013, New Astronomy Reviews, 57, 52

Battaglia, G., Helmi, A., Tolstoy, E., et al. 2008a, ApJ, 681, L13

Battaglia, G., Irwin, M., Tolstoy, E., de Boer, T., & Mateo, M. 2012a, ApJ, 761, L31

Battaglia, G., Irwin, M., Tolstoy, E., et al. 2008b, MNRAS, 383, 183

Battaglia, G., Rejkuba, M., Tolstoy, E., Irwin, M. J., & Beccari, G. 2012b, MNRAS, 424, 1113

Battaglia, G., & Starkenburg, E. 2012, A&A, 539, A123

Battaglia, G., Tolstoy, E., Helmi, A., et al. 2011, MNRAS, 411, 1013

—. 2006, A&A, 459, 423

Bellazzini, M., Ferraro, F. R., Origlia, L., et al. 2002, AJ, 124, 3222

Bellazzini, M., Ferraro, F. R., & Pancino, E. 2001, MNRAS, 327, L15

Benítez-Llambay, A., Navarro, J. F., Abadi, M. G., et al. 2016, MNRAS, 456, 1185

Bermejo-Climent, J. R., Battaglia, G., Gallart, C., et al. 2018, MNRAS, 479, 1514

Bertelli, G., Bressan, A., Chiosi, C., Fagotto, F., & Nasi, E. 1994, A&AS, 106

Bettinelli, M., Hidalgo, S. L., Cassisi, S., Aparicio, A., & Piotto, G. 2018, MNRAS, arXiv:1801.08145

Binney, J., & Tremaine, S. 2008, Galactic Dynamics: Second Edition (Princeton University Press)

Bonnarel, F., Fernique, P., Bienaymé, O., et al. 2000, A&AS, 143, 33

Brandt, T. D. 2016, ApJ, 824, L31

Brasseur, C. M., Martin, N. F., Macciò, A. V., Rix, H.-W., & Kang, X. 2011, ApJ, 743, 179

Breddels, M. A., & Helmi, A. 2013, A&A, 558, A35

Carrera, R., Aparicio, A., Martínez-Delgado, D., & Alonso-García, J. 2002, AJ, 123, 3199

Carrera, R., Pancino, E., Gallart, C., & del Pino, A. 2013, MNRAS, 434, 1681

Casetti-Dinescu, D. I., Girard, T. M., & Schriefer, M. 2017, ArXiv e-prints, arXiv:1710.02462

Chonis, T. S., Martínez-Delgado, D., Gabany, R. J., et al. 2011, AJ, 142, 166

Choudhury, T. R., Ferrara, A., & Gallerani, S. 2008, MNRAS, 385, L58

Cicuéndez, L., Battaglia, G., Irwin, M., et al. 2018, A&A, 609, A53

Coleman, M., Da Costa, G. S., Bland-Hawthorn, J., et al. 2004, AJ, 127, 832

Contenta, F., Balbinot, E., Petts, J. A., et al. 2018, MNRAS, arXiv:1705.01820

Crnojević, D., Sand, D. J., Zaritsky, D., et al. 2016, ApJ, 824, L14

de Boer, T. J. L., Tolstoy, E., Hill, V., et al. 2012, A&A, 539, A103

de Vaucouleurs, G. 1948, Annales d'Astrophysique, 11, 247

Deason, A., Wetzel, A., & Garrison-Kimmel, S. 2014, ApJ, 794, 115

Dolphin, A. E. 2002, MNRAS, 332, 91

Dubinski, J., & Carlberg, R. G. 1991, ApJ, 378, 496

Ebrová, I., & Łokas, E. L. 2015, ApJ, 813, 10

Faber, S. M., & Lin, D. N. C. 1983, ApJ, 266, L17

Fakhouri, O., Ma, C.-P., & Boylan-Kolchin, M. 2010, MNRAS, 406, 2267

Faria, D., Feltzing, S., Lundström, I., et al. 2007, A&A, 465, 357

Ferguson, A. M. N., & Mackey, A. D. 2016, in Astrophysics and Space Science Library, Vol. 420, Tidal Streams in the Local Group and Beyond, ed. H. J. Newberg & J. L. Carlin, 191

Ford, H. C., Bartko, F., Bely, P. Y., et al. 1998, in Proc. SPIE, Vol. 3356, Space Telescopes and Instruments V, ed. P. Y. Bely & J. B. Breckinridge, 234–248

Foreman-Mackey, D., Hogg, D. W., Lang, D., & Goodman, J. 2013, PASP, 125, 306

Fouquet, S., Łokas, E. L., del Pino, A., & Ebrová, I. 2017, MNRAS, 464, 2717

Fritz, T. K., Battaglia, G., Pawlowski, M. S., et al. 2018, ArXiv e-prints, arXiv:1805.00908

Gaia Collaboration, Helmi, A., van Leeuwen, F., et al. 2018, ArXiv e-prints, arXiv:1804.09381

Geha, M., Willman, B., Simon, J. D., et al. 2009, ApJ, 692, 1464

Goodman, J., & Weare, J. 2010, CAMCS, 5, 1, 65

Goodwin, S. P. 1997, MNRAS, 286, L39

Harbeck, D., Grebel, E. K., Holtzman, J., et al. 2001, AJ, 122, 3092

Harris, W. E. 2010, ArXiv e-prints, arXiv:1012.3224

Hills, J. G., & Day, C. A. 1976, Astrophys. Lett., 17, 87

Ho, N., Geha, M., Munoz, R. R., et al. 2012, ApJ, 758, 124

Hodge, P. W. 1961, AJ, 66, 83

—. 1964, AJ, 69, 438

—. 1966, AJ, 71, 204

Hubble, E. P. 1930, ApJ, 71, doi:10.1086/143250

Ibata, R., Lewis, G. F., Irwin, M., Totten, E., & Quinn, T. 2001, ApJ, 551, 294

Ibata, R. A., Gilmore, G., & Irwin, M. J. 1994, Nature, 370, 194

Irwin, M., & Hatzidimitriou, D. 1995, MNRAS, 277, 1354

Irwin, M., & Lewis, J. 2001, New Astronomy Reviews, 45, 105

Irwin, M. J., Bunclark, P. S., Bridgeland, M. T., & McMahon, R. G. 1990, MNRAS, 244, 16P

Jin, S., Irwin, M., Tolstoy, E., Lewis, J., & Hartke, J. 2016, in Astronomical Society of the Pacific Conference Series, Vol. 507, Multi-Object Spectroscopy in the Next Decade: Big Questions, Large Surveys, and Wide Fields, ed. I. Skillen, M. Balcells, & S. Trager, 241

Jordi, K., Grebel, E. K., & Ammon, K. 2006, A&A, 460, 339

Kacharov, N., Battaglia, G., Rejkuba, M., et al. 2017, MNRAS, 466, 2006

Kass, R. E., & Raftery, A. E. 1995, J. Amer. Statist. Assoc., 90

Kazantzidis, S., Mayer, L., Callegari, S., Dotti, M., & Moustakas, L. A. 2017, ApJ, 836, L13

Kepner, J., Fan, X., Bahcall, N., et al. 1999, ApJ, 517, 78

King, I. 1962, AJ, 67, 471

King, I. R. 1966, AJ, 71, 64

Kirby, E. N., Cohen, J. G., Guhathakurta, P., et al. 2013, ApJ, 779, 102

Kirby, E. N., Lanfranchi, G. A., Simon, J. D., Cohen, J. G., & Guhathakurta, P. 2011, ApJ, 727, 78

Kirby, E. N., Guhathakurta, P., Simon, J. D., et al. 2010, ApJS, 191, 352

Kleyna, J. T., Wilkinson, M. I., Evans, N. W., & Gilmore, G. 2004, MNRAS, 354, L66

Kleyna, J. T., Wilkinson, M. I., Gilmore, G., & Evans, N. W. 2003, ApJ, 588, L21

Law, D. R., Johnston, K. V., & Majewski, S. R. 2005, ApJ, 619, 807

Lee, M. G., Yuk, I.-S., Park, H. S., Harris, J., & Zaritsky, D. 2009, ApJ, 703, 692

Lee, M. G., Park, H. S., Park, J.-H., et al. 2003, AJ, 126, 2840

Lejeune, T., Cuisinier, F., & Buser, R. 1997, A&AS, 125, astro-ph/9701019

Lora, V., Just, A., Sánchez-Salcedo, F. J., & Grebel, E. K. 2012, ApJ, 757, 87

Maccarone, T. J., Fender, R. P., & Tzioumis, A. K. 2005, MNRAS, 356, L17

Mapelli, M., Ripamonti, E., Battaglia, G., et al. 2009, MNRAS, 396, 1771

Mapelli, M., Ripamonti, E., Tolstoy, E., et al. 2007, MNRAS, 380, 1127

Martínez-Delgado, D., Peñarrubia, J., Gabany, R. J., et al. 2008, ApJ, 689, 184

Martínez-Delgado, D., Pohlen, M., Gabany, R. J., et al. 2009, ApJ, 692, 955

Martínez-Delgado, D., Romanowsky, A. J., Gabany, R. J., et al. 2012, ApJ, 748, L24

Martínez-Vázquez, C. E., Monelli, M., Bono, G., et al. 2015, MNRAS, 454, 1509

Massari, D., Breddels, M. A., Helmi, A., et al. 2018, Nature Astronomy, 2, 156

Mayer, L., Kazantzidis, S., Mastropietro, C., & Wadsley, J. 2007, Nature, 445, 738

McConnachie, A. W. 2012, AJ, 144, 4

McConnachie, A. W., Arimoto, N., & Irwin, M. 2007, MNRAS, 379, 379

McConnachie, A. W., & Irwin, M. J. 2006, MNRAS, 365, 1263

McCrea, W. H. 1964, MNRAS, 128, 147

McMonigal, B., Bate, N. F., Lewis, G. F., et al. 2014, MNRAS, 444, 3139

Momany, Y., Held, E. V., Saviane, I., et al. 2007, A&A, 468, 973

Monelli, M., Hidalgo, S. L., Stetson, P. B., et al. 2010, ApJ, 720, 1225

Muñoz, R. P., Eigenthaler, P., Puzia, T. H., et al. 2015, ApJ, 813, L15

Muñoz, R. R., Côté, P., Santana, F. A., et al. 2018, ApJ, 860, 66

Muñoz, R. R., Geha, M., Côté, P., et al. 2012, ApJ, 753, L15

Muñoz, R. R., Majewski, S. R., & Johnston, K. V. 2008, ApJ, 679, 346

Muñoz, R. R., Frinchaboy, P. M., Majewski, S. R., et al. 2005, ApJ, 631, L137

Navarro, J. F., Frenk, C. S., & White, S. D. M. 1996, ApJ, 462, 563

Newby, M., Cole, N., Newberg, H. J., et al. 2013, AJ, 145, 163

Norris, J. E., Wyse, R. F. G., Gilmore, G., et al. 2010, ApJ, 723, 1632

Nucita, A. A., De Paolis, F., Manni, L., & Ingrosso, G. 2013, NA, 23, 107

Okamoto, S., Arimoto, N., Tolstoy, E., et al. 2017, MNRAS, arXiv:1701.04422

Olszewski, E. W., Aaronson, M., & Hill, J. M. 1995, AJ, 110, 2120

Pace, A. B., Martinez, G. D., Kaplinghat, M., & Muñoz, R. R. 2014, MNRAS, 442, 1718

Palma, C., Majewski, S. R., Siegel, M. H., et al. 2003, AJ, 125, 1352

Peñarrubia, J., Navarro, J. F., & McConnachie, A. W. 2008, ApJ, 673, 226

Peñarrubia, J., Walker, M. G., & Gilmore, G. 2009, MNRAS, 399, 1275

Piatti, A. E. 2018, MNRAS, 473, 492

Pietrinferni, A., Cassisi, S., Salaris, M., & Castelli, F. 2004, ApJ, 612, 168

Plummer, H. C. 1911, MNRAS, 71, 460

Pont, F., Zinn, R., Gallart, C., Hardy, E., & Winnick, R. 2004, AJ, 127, 840

Press, W. H., Teukolsky, S. A., Vetterling, W. T., & Flannery, B. P. 1992, Numerical recipes in FORTRAN. The art of scientific computing

Read, J. I., & Gilmore, G. 2005, MNRAS, 356, 107

Read, J. I., Wilkinson, M. I., Evans, N. W., Gilmore, G., & Kleyna, J. T. 2006, MNRAS, 367, 387

Revaz, Y., & Jablonka, P. 2018, ArXiv e-prints, arXiv:1801.06222

Rey, S.-C., Lee, Y.-W., Ree, C. H., et al. 2004, AJ, 127, 958

Rich, R. M., Collins, M. L. M., Black, C. M., et al. 2012, Nature, 482, 192

Richardson, J. C., Irwin, M. J., McConnachie, A. W., et al. 2011, ApJ, 732, 76

Robert, C. P., & Casella, G. 2004, Monte Carlo Statistical Methods, 79–122

Robin, A. C., Reylé, C., Derrière, S., & Picaud, S. 2003, A&A, 409, 523

Rockosi, C. M., Odenkirchen, M., Grebel, E. K., et al. 2002, AJ, 124, 349

Roderick, T. A., Jerjen, H., Da Costa, G. S., & Mackey, A. D. 2016a, MNRAS, 460, 30

Roderick, T. A., Jerjen, H., Mackey, A. D., & Da Costa, G. S. 2015, ApJ, 804, 134

Roderick, T. A., Mackey, A. D., Jerjen, H., & Da Costa, G. S. 2016b, MNRAS, 461, 3702

Rutledge, G. A., Hesser, J. E., & Stetson, P. B. 1997, PASP, 109, 907

Sales, L. V., Helmi, A., & Battaglia, G. 2010, Advances in Astronomy, 2010, 194345

Sánchez-Salcedo, F. J., & Lora, V. 2007, ApJ, 658, L83

Schlafly, E. F., & Finkbeiner, D. P. 2011, ApJ, 737, 103

Schlegel, D. J., Finkbeiner, D. P., & Davis, M. 1998, ApJ, 500, 525

Sersic, J. L. 1968, Atlas de galaxias australes

Smirnov, N. V. 1939, Bulletin of Moscow University, 2, 3

Staneva, A., Spassova, N., & Golev, V. 1996, A&AS, 116, 447

Stark, D. P., Bunker, A. J., Ellis, R. S., Eyles, L. P., & Lacy, M. 2007, ApJ, 659, 84

Starkenburg, E., Hill, V., Tolstoy, E., et al. 2010, A&A, 513, A34

Stetson, P. B. 1987, PASP, 99, 191

—. 1994, PASP, 106, 250

Strobel, N. V., & Lake, G. 1994, ApJ, 424, L83

Tammann, G. A. 1994, in European Southern Observatory Conference and Workshop Proceedings, Vol. 49, European Southern Observatory Conference and Workshop Proceedings, ed. G. Meylan & P. Prugniel, 3

Tollerud, E. J., Beaton, R. L., Geha, M. C., et al. 2012, ApJ, 752, 45

Tolstoy, E., Hill, V., & Tosi, M. 2009, ARA&A, 47, 371

Tolstoy, E., Irwin, M. J., Helmi, A., et al. 2004, ApJ, 617, L119

Ural, U., Cescutti, G., Koch, A., et al. 2015, MNRAS, 449, 761

Walker, M. 2013, Dark Matter in the Galactic Dwarf Spheroidal Satellites, ed. T. D. Oswalt & G. Gilmore, 1039

Walker, M. G., Mateo, M., & Olszewski, E. W. 2008, ApJ, 688, L75

—. 2009a, AJ, 137, 3100

Walker, M. G., Mateo, M., Olszewski, E. W., et al. 2006, ApJ, 642, L41

—. 2010, ApJ, 710, 886

Walker, M. G., Mateo, M., Olszewski, E. W., Sen, B., & Woodroofe, M. 2009b, AJ, 137, 3109

Walker, M. G., & Peñarrubia, J. 2011, ApJ, 742, 20

White, S. D. M., & Rees, M. J. 1978, MNRAS, 183, 341

Wilkinson, M. I., Kleyna, J. T., Evans, N. W., et al. 2004, ApJ, 611, L21

Willman, B., Geha, M., Strader, J., et al. 2011, AJ, 142, 128

Wilson, A. G. 1955, PASP, 67, 27

Wolf, J., Martinez, G. D., Bullock, J. S., et al. 2010, MNRAS, 406, 1220

Wu, X. 2007, ArXiv Astrophysics e-prints, astro-ph/0702233

Young, L. M. 2000, AJ, 119, 188

Zaritsky, D., Crnojević, D., & Sand, D. J. 2016, ApJ, 826, L9

Zhu, L., van de Ven, G., Watkins, L. L., & Posti, L. 2016, MNRAS, 463, 1117

# A

# Appendix of Chapter 2

## A.1 On the outer regions of DECam pointings

We attempted to overcome the morphological misclassification of point-like versus extended objects in the out-of-focus regions of the DECam pointings in various ways, testing the outcome of the possible solutions by looking at the resulting surface density maps: our "figure-of-merit" was the lack of ring-like over-densities of point-like objects in the external regions of the pointings, above the $\sigma$ detection limits used for the scientific analysis of the density maps (see Sect. 2.4).

We first tried to quantify the morphological misclassification by creating a density map of point sources expected to have a fairly constant spatial distribution on the probed spatial regions, that is Milky Way foreground stars, which we could then use as a correction factor. To this end, we selected objects in the colour range $1.1 < g-r < 1.6$, in order to avoid the region of the CMD occupied by Sextans stars. Figure A.1 shows the mean density of point-like (top-left) and extended (top-right) objects falling in this colour range, discarding $3\sigma$ outliers, with $\sigma$ being the standard deviation between the different pointings. However, the change in the out-of-focus regions from pointing to pointing was large enough that the point-like object mask created more inhomogeneities in the density map than it solved.

The next attempt was to correct for all artificial inhomogeneities in the whole mosaic area at once (e.g. changes in the density caused by differences in depth between pointings or the mentioned morphological misclassification) by measuring the smoothed density of the point-like objects in the colour range $1.1 < g - r < 1.6$ across the full mosaic area. However, this attempt was

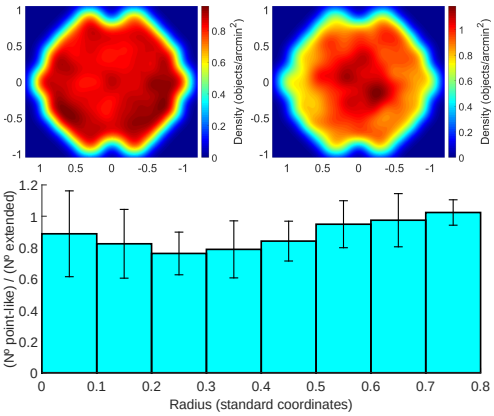


Figure A.1: Smoothed map of the mean density pattern for point-like (top-left) and extended (top-right) objects with $1.1 < g - r < 1.6$ in standard coordinates, discarding $3\sigma$ outliers, with $\sigma$ being the standard deviation between the different pointings. The bottom panel plots the ratio of point-like/extended objects, showing the spatial gradient in the morphological misclassification when moving away from the centre of the pointings. The error bars indicate the standard deviation of the ratios derived from the different measurements in all the pointings.

also unsuccessful; one issue with this approach was that the morphological misclassification depends on magnitude, and the luminosity function both of point-like and extended sources in the colour range $1.1 < g - r < 1.6$ is not representative of the luminosity function across the whole colour range of the data (for example in the region occupied by Sextans stars).

We also tried ignoring our morphological discriminators, using all objects except probable noise. Nonetheless multiple galaxy clusters from the background contamination appeared in different regions of the mosaic, impacting on the density map of Sextans dSph stars.

Adopting a more restrictive morphological classification, that is using for the analysis only the objects that the pipeline identified as the most likely to be stars (morphological classification flag $-1$ in both photometric bands), did not help, while reducing considerably the statistics. Finally, we tried using the inverse density map of extended objects as a correction factor to the map of point-like sources, since the overdensities of morphologically misclassified point-like sources correspond to underdensities of extended objects. Nonetheless clusters of galaxies and differences in depth between pointings introduce much larger inhomogeneities in the map of extended objects than those created by the star/galaxy misclassification, so applying this mask created even more cosmetic features.

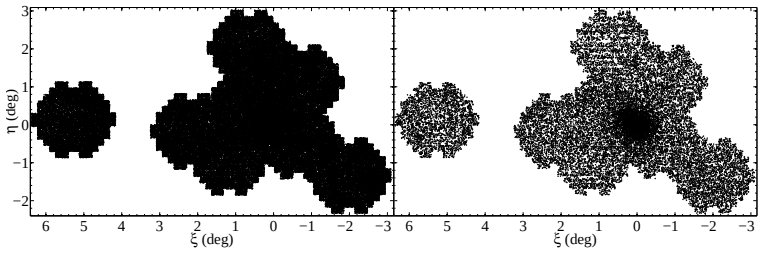


Figure A.2: Locations of the objects from our photometric catalogue. Left: all sources; right: point-like sources brighter than $(g, r) = (23.0, 23.0)$.

The most satisfactory solution was to use only point-like sources brighter than $(g, r) = (23.0, 23.0)$, approximately the region where the locus of unresolved galaxies starts appearing on the CMD. As it can be seen in Fig. A.2, artificial overdensities and clusters of galaxies are effectively removed, though at the cost of reduced statistics. Although the sample under consideration has a brighter magnitude limit than the catalogue used by R16, comparing Fig. 2.8 with their Fig. 8 one can see that the central densities of both catalogues are very similar ($\sim$ 4 stars/arcmin$^2$). This implies that, in spite of their deeper magnitude cut, the reached number density of stars from the galaxy (and therefore the statistics) is similar in both datasets, possibly due to distinct selection criteria compensating the different magnitude cuts. In addition, apart from the larger covered area in our mosaic, while their magnitude cut correspond to the 90% completeness level of their shallowest pointing, our magnitude cut is likely to ensure a $\sim$ 100% completeness level for the whole mosaic.

When attempting to correct for artificial features, the aforementioned masks were applied in the form of a 'flat-field', that is dividing the density maps of point-like sources by the normalized masks. In R16 the mask for the whole mosaic created from stars outside their CMD window (likely contaminants) was applied to the normalized density map of the stars falling inside it (likely Sextans' stars) in the form of a flat-field too; however, it was then also subtracted from the resulting 'flat-fielded' map to emphasize low-density features of Sextans' stars. As we have explained, this flat-fielding would not fix any of these artificial problems except the gaps between CCDs if no dithering was done (not our case), while in our opinion the last step may strongly affect the real shape of the dSph by underestimating the galactic density in the most contaminated regions, regardless of whether their galaxy/contamination density ratio is high or low. This would create holes in the contour map of the galaxy, mimick-

ing the appearance of over-dense distortions surrounding the overdensities of contamination, where instead the galactic density can remain constant. We think this may contribute to the boxy appearance of Sextans in R16, aligned with its major and minor axes; this would be caused by the higher detected contamination density in the overlapping regions of the pointings placed along the major and minor axes of Sextans.

## A.2 MCMC Hammer applied to mock galaxies

We tested the performance of the MCMC Hammer method used in Sect. 2.3 by applying it to mock datasets of point-sources, aimed at probing different regimes of number statistics and spatial coverage of the dataset.

First, we generate catalogues of point-sources distributed according to a given surface density profile $f(r)$ following the method outlined in *Numerical Recipes* (Press et al. 1992) for the generation of random numbers with a desired distribution. Here $r$ denotes the distance along the projected major axis of the mock galaxy. Its normalized CDF is:

$$F(R) = \int_0^R f(r) 2\pi r \, \mathrm{d}r \Big/ \int_0^\infty f(r) 2\pi r \, \mathrm{d}r \,, \tag{A.1}$$

which describes the fraction of stars that we expect to find within a radius $R$, being equal to 0 if $R = 0$ and equal to 1 when $R \to \infty$. If $x$ is a uniform random number between 0 and 1, it can be shown (Press et al. 1992) that a random number following the desired number density distribution is generated by: $r(x) = F^{-1}(x)$, where $F^{-1}$ is the inverse of the CDF described by Eq. A.1.

Thus, to create the mock galaxy we first generate random numbers $x_i$ between 0 and 1, from which we calculate the corresponding major axis radii $r_i(x_i) = F^{-1}(x_i)$ for an exponential profile of scale radius $r_e$, using a computational bisection algorithm to find inverse functions. We then generate the angular coordinates following a uniform distribution between 0 and $2\pi$, transform the angular coordinates into cartesian ones, adjust the ellipticity ($e$) by multiplying the vertical coordinates by the factor $(1 - e)$ and finally rotate all the data points by the position angle $\theta$. This produces a mock galaxy with an exponential surface density profile centered on the origin. In order to simulate realistic observational conditions, we also added a constant contamination density by generating random stars with a uniform spatial distribution.

The exponential radius and position angle are fixed to $r_e = 10$ arcmin and $\theta = 50°$, respectively. The parameters we vary are the number of mock stars within the spatial coverage of the mock dataset, $N$, the ellipticity of the galaxy,

$e$, and the coverage. We generate 18 mock galaxies corresponding to a grid of 3x2x3 in the aforementioned parameters ($N$ = 200, 1000, 5000; $e$ = 0.1, 0.3; for the coverage we used squares of sides equal to 2, 5 and 10 times $r_e$). We set the number of contaminants to 20% of the total number $N$ of stars, which is fixed inside the different coverages. This results into different contamination densities and scale factors $k$ (equal to the central densities in the case of the exponential profile) between the different coverages with same $N$. As when fitting the dataset of the Sextans dSph, in the MCMC Hammer we defined 80 walkers, each of them doing approximately $10^4$ steps.

Table A.1 summarizes the best-fitting parameters we obtain. As expected, there is a clear effect of the ellipticity on the determination of position angles, especially at low coverages and number of data points. Likewise, the effect of the area is important since low coverages produce difficulties in fitting the contamination density when there are no areas with low density of galaxy population. Even if the number of analysed stars is high, as with $N = 5000$, there are still high dispersions in this parameter at $2r_e$ coverage. The scale length, the position angle and the ellipticity are also quite affected by the size of the analysed area, having higher error bars at low coverages. In the case of the dataset of Sextans we had an ellipticity close to 0.3, a total number of stars from the galaxy near 5000 and a coverage larger than $10r_e$. These numbers make the dataset of Sextans similar to the mock one with the structural parameters most constrained by the MCMC Hammer.

The large error bars in some parameters can make the Bayesian posterior distribution non-gaussian when there are prior restrictions on the parameter. This happens with the central surface density and contamination density, which are set to be greater than zero in order to have physical meaning; and with the ellipticity, that is defined between 0 and 1. However, what really matters for this work is how reliable the inferred error bars on the parameters estimates are. *In this respect Table A.1 shows that, if the models are a good representation of the data, we can rely on the error bars, since the input parameters for all the mock galaxies are always recovered within the 2$\sigma$ confidence level and in most cases within the 1$\sigma$ level, even for low number statistics and restricted spatial coverages; the trade-off being much larger error bars, obviously.*

## A.3 Goodness-of-fit indicators

The $\chi^2_{red}$ was calculated from the observed surface number density profile derived from elliptical, concentric annuli and the best-fitting profiles, by assuming that star counts follow Poisson distributions with means equal to the star counts from the best-fit model. As the $\chi^2_{red}$ test requires normal distributions,

| $e_i$ | Coverage ($r_e$) | $\sigma_{c,\,i}$ (stars/arcmin$^2$) | $k$ (stars/arcmin$^2$) | $r_e$ (′) | $\alpha_0$ (º) | $\delta_0$ (º) | $\theta$ (º) | $e$ | $\sigma_c$ (stars/arcmin$^2$) |
|---|---|---|---|---|---|---|---|---|---|
| 0.1 | 2 | 0.100 | $0.48^{+0.19}_{-0.22}$ | $29.1^{+89.7}_{-17.7}$ | $0.01^{+0.04}_{-0.04}$ | $0.02^{+0.03}_{-0.03}$ | $63^{+31}_{-33}$ | $0.45^{+0.31}_{-0.39}$ | $0.209^{+0.168}_{-0.142}$ |
| 0.1 | 5 | 0.016 | $0.42^{+0.07}_{-0.07}$ | $8.7^{+1.6}_{-1.6}$ | $0.00^{+0.02}_{-0.02}$ | $0.00^{+0.02}_{-0.02}$ | $48^{+32}_{-31}$ | $0.11^{+0.09}_{-0.08}$ | $0.022^{+0.011}_{-0.011}$ |
| 0.1 | 10 | 0.004 | $0.25^{+0.05}_{-0.05}$ | $9.8^{+1.6}_{-1.4}$ | $0.00^{+0.02}_{-0.02}$ | $0.00^{+0.02}_{-0.02}$ | $65^{+38}_{-38}$ | $0.10^{+0.11}_{-0.07}$ | $0.007^{+0.002}_{-0.002}$ |
| 0.3 | 2 | 0.100 | $0.57^{+0.23}_{-0.24}$ | $18.7^{+51.5}_{-11.9}$ | $0.03^{+0.03}_{-0.03}$ | $0.00^{+0.03}_{-0.03}$ | $53^{+32}_{-40}$ | $0.39^{+0.39}_{-0.23}$ | $0.258^{+0.159}_{-0.174}$ |
| 0.3 | 5 | 0.016 | $0.51^{+0.14}_{-0.11}$ | $7.5^{+1.9}_{-1.3}$ | $0.01^{+0.02}_{-0.02}$ | $0.03^{+0.02}_{-0.02}$ | $35^{+16}_{-16}$ | $0.26^{+0.13}_{-0.13}$ | $0.035^{+0.010}_{-0.010}$ |
| 0.3 | 10 | 0.004 | $0.31^{+0.06}_{-0.05}$ | $10.6^{+1.1}_{-1.0}$ | $0.00^{+0.02}_{-0.02}$ | $0.01^{+0.02}_{-0.02}$ | $51^{+13}_{-13}$ | $0.21^{+0.09}_{-0.10}$ | $0.003^{+0.001}_{-0.001}$ |
| 0.1 | 2 | 0.50 | $4.40^{+0.51}_{-0.55}$ | $8.9^{+2.7}_{-2.7}$ | $0.00^{+0.01}_{-0.01}$ | $0.00^{+0.01}_{-0.01}$ | $73^{+18}_{-27}$ | $0.16^{+0.14}_{-0.10}$ | $0.74^{+0.60}_{-0.50}$ |
| 0.1 | 5 | 0.08 | $1.81^{+0.20}_{-0.16}$ | $10.0^{+1.5}_{-1.4}$ | $0.00^{+0.01}_{-0.01}$ | $0.01^{+0.01}_{-0.01}$ | $40^{+15}_{-13}$ | $0.14^{+0.06}_{-0.07}$ | $0.09^{+0.04}_{-0.04}$ |
| 0.1 | 10 | 0.02 | $1.58^{+0.13}_{-0.11}$ | $9.4^{+0.5}_{-0.5}$ | $0.00^{+0.01}_{-0.01}$ | $-0.01^{+0.01}_{-0.01}$ | $43^{+17}_{-18}$ | $0.08^{+0.05}_{-0.04}$ | $0.02^{+0.01}_{-0.01}$ |
| 0.3 | 2 | 0.50 | $4.67^{+0.50}_{-0.51}$ | $9.4^{+2.3}_{-2.3}$ | $0.00^{+0.01}_{-0.01}$ | $-0.01^{+0.01}_{-0.01}$ | $47^{+21}_{-21}$ | $0.17^{+0.10}_{-0.10}$ | $0.58^{+0.53}_{-0.40}$ |
| 0.3 | 5 | 0.08 | $2.39^{+0.21}_{-0.19}$ | $10.2^{+0.9}_{-0.8}$ | $0.00^{+0.01}_{-0.01}$ | $0.00^{+0.01}_{-0.01}$ | $46^{+4}_{-4}$ | $0.38^{+0.04}_{-0.04}$ | $0.07^{+0.02}_{-0.02}$ |
| 0.3 | 10 | 0.02 | $1.71^{+0.13}_{-0.12}$ | $10.9^{+0.6}_{-0.6}$ | $0.00^{+0.01}_{-0.01}$ | $0.00^{+0.01}_{-0.01}$ | $51^{+3}_{-3}$ | $0.36^{+0.04}_{-0.04}$ | $0.02^{+0.01}_{-0.01}$ |
| 0.1 | 2 | 2.50 | $21.5^{+1.2}_{-1.4}$ | $11.3^{+1.4}_{-1.6}$ | $-0.01^{+0.01}_{-0.01}$ | $0.00^{+0.01}_{-0.01}$ | $52^{+16}_{-19}$ | $0.10^{+0.06}_{-0.05}$ | $1.41^{+1.65}_{-1.03}$ |
| 0.1 | 5 | 0.40 | $8.7^{+0.4}_{-0.3}$ | $10.3^{+0.7}_{-0.6}$ | $0.00^{+0.01}_{-0.01}$ | $0.00^{+0.01}_{-0.01}$ | $47^{+21}_{-21}$ | $0.04^{+0.03}_{-0.03}$ | $0.32^{+0.10}_{-0.10}$ |
| 0.1 | 10 | 0.10 | $7.2^{+0.3}_{-0.3}$ | $10.0^{+0.2}_{-0.2}$ | $0.00^{+0.01}_{-0.01}$ | $0.00^{+0.01}_{-0.01}$ | $54^{+7}_{-7}$ | $0.09^{+0.02}_{-0.02}$ | $0.10^{+0.01}_{-0.01}$ |
| 0.3 | 2 | 2.50 | $22.5^{+1.3}_{-1.4}$ | $10.6^{+1.8}_{-1.8}$ | $0.00^{+0.01}_{-0.01}$ | $0.00^{+0.01}_{-0.01}$ | $48^{+6}_{-6}$ | $0.30^{+0.04}_{-0.04}$ | $2.52^{+1.69}_{-1.65}$ |
| 0.3 | 5 | 0.40 | $10.3^{+0.5}_{-0.4}$ | $10.3^{+0.5}_{-0.5}$ | $0.00^{+0.01}_{-0.01}$ | $0.00^{+0.01}_{-0.01}$ | $47^{+3}_{-3}$ | $0.29^{+0.02}_{-0.02}$ | $0.40^{+0.06}_{-0.06}$ |
| 0.3 | 10 | 0.10 | $9.1^{+0.3}_{-0.3}$ | $10.1^{+0.2}_{-0.2}$ | $0.00^{+0.01}_{-0.01}$ | $0.00^{+0.01}_{-0.01}$ | $49^{+2}_{-2}$ | $0.31^{+0.02}_{-0.02}$ | $0.10^{+0.01}_{-0.01}$ |

Table A.1: Structural parameters (median values of the marginalized posterior distributions) obtained with the MCMC Hammer for mock galaxies with number of analysed stars $N = 200$, 1000 and 5000 (top, middle and bottom sequences of rows respectively). From left to right: input ellipticity ($e_i = 1 - b/a$), coverage (in $r_e$ units), input contamination density ($\sigma_{c,\,i}$) and fitted parameters: scale factor ($k$, equal to the central density in the case of the exponential profile), exponential radius ($r_e$), galactic centre ($\alpha_0$, $\delta_0$), position angle ($\theta$), ellipticity ($e$) and contamination density ($\sigma_c$).

not Poisson ones, the bin size is chosen to guarantee a minimum of 5 stars per annulus, such that all Poisson distributions can be approximated by normal ones (Central limit theorem). The reduced chi-squared $\chi^2_{red}$ is then:

$$\chi^2_{red} = \frac{\chi^2}{n-p-1} = \sum_{i=1}^{n} \frac{(O_i - E_i)^2}{E_i\,(n-p-1)}\,, \tag{A.2}$$

with $n$ the number of elliptical annuli, $p$ the number of free parameters, and $O_i$ and $E_i$ the observed and expected star counts, respectively. In practice, this means that the sample variances are calculated with respect to the model and the population ones are the Poisson variances from the fitted model ($\sigma^2 = E_i$).

Although the $\chi^2_{red}$ gives a rough description of how good a fitting is, it is not always a reliable discriminant to prove which model better fits the data: it is required to be in a regime in which the Poisson distribution can be approximated by a normal distribution and the value is quite dependent on the choice of the bin size. For the same reasons, structural parameters derived via conventional $\chi^2_{red}$ fitting are not as reliable as when they are derived following more appropriated techniques. As one can check in Table 2.3, according to their $\chi^2_{red}$ all the functional forms of the profiles fitted in this work perform approximately equally well, even when accounting for the profiles fitted by IH95. As we will see later, the order given by $\chi^2_{red}$ does not coincide with the ones given by more reliable indicators. In this respect the ratio of maximum likelihoods tell us how many times the data is more likely to follow one profile than the other, without making assumptions or loosing information due to the spatial binning.

Nonetheless, neither the $\chi^2$ or the classical likelihood ratio take into account the probability of having structural parameters different from the most probable ones. Here is where Bayesian statistics makes the difference. Bayes' theorem states:

$$P(M|D) = \frac{P(D|M)\,P(M)}{P(D)}\,, \tag{A.3}$$

where the events $M$ and $D$ are, in the case that concerns us, the model being evaluated (i.e. the surface density profile) and our dataset respectively. $P(M|D)$, known as the posterior, is the probability of the analysed profile to reproduce our dataset. $P(D|M)$, known as the likelihood, is the probability of our dataset to reproduce the profile. $P(M)$, known as the prior, is the probability of the profile regardless of our specific dataset. Finally, the normalizing constant $P(D)$, known as the marginal likelihood, is the global probability of our dataset summing the probabilities of all the considered profiles. In the

same way, we can use Bayes' theorem to calculate the posteriors of the structural parameters from a given profile, assuming that the considered profile is the true one:

$$P(\theta|M,D) = \frac{P(D|M,\theta)\,P(\theta|M)}{P(D|M)}\,, \tag{A.4}$$

with $\theta$ being the structural parameters and the marginal likelihood being:

$$P(D|M) = \int_\theta P(D|M,\theta)\,P(\theta|M)\,\mathrm{d}\theta\,, \tag{A.5}$$

integrated over all the structural parameters' domain. Integrating Eq. A.4 along its different dimensions $\theta_i$ we can then obtain the variety of projections previously shown in Fig. 2.7.

Through Eq. A.5, that is marginalizing the likelihood over all its parameters, one considers all the possible shapes that each profile can take, depending on the probability distribution functions of the model parameters. This can potentially result in the fact that a model much more likely than others when considering the most probable values of its parameters, is less likely when considering the full distribution of possible values. This is the Occam's razor intrinsic to Bayesian statistics, which automatically penalizes overfitted profiles due to an excess of variables.

The ratio between the posteriors of two different models tells us how many times one model is more likely to follow the data than the other. If we do not have a prior idea of which model is more likely, both priors in the expression of the posteriors vanish when dividing, which results in the ratio of the marginal likelihoods of both models. This ratio between the marginal likelihoods of two different models is called the Bayes factor:

$$\frac{P(M_1|D)}{P(M_2|D)} = \frac{P(D|M_1)}{P(D|M_2)} = K_{12} \quad \text{if } P(M_1) = P(M_2)\,. \tag{A.6}$$

However, it is not straightforward to evaluate these marginal likelihoods over the high dimensional spaces of the fitted profiles. In computational terms it is not feasible to calculate the numerical integral of Eq. A.5 over their corresponding N-dimensional grids; they need to be evaluated through Monte Carlo integration (Robert & Casella 2004). Here is where the MCMC becomes important: given two functions, $f(\theta)$ and $g(\theta)$, with the last one being normalized, the integral $\int_\theta f(\theta)\,g(\theta)\,\mathrm{d}\theta$ is equal to the mean value of $f(\theta)$ evaluated at the points sampled with the MCMC from $g(\theta)$. Thus, in principle, we could obtain the Bayes' factors between the different profiles by calculating Eq. A.5 for each profile through the MCMC Hammer and the expressions of the likelihood $P(D|M,\theta) = f(\theta)$ and prior $P(\theta|M) = g(\theta)$.

| $2\ln K_{12}$ | $K_{12}$ | Evidence against $M_2$ |
|---|---|---|
| 0 to 2 | 1 to 3 | Not worth more than a bare mention |
| 2 to 6 | 3 to 20 | Positive |
| 6 to 10 | 20 to 150 | Strong |
| $> 10$ | $> 150$ | Very strong |

Table A.2: Evidence classification of the Bayes factors according to Kass & Raftery (1995)

However, if there is any improper function in the definition of some prior there is no possibility of sampling it with a MCMC. As this is our case, we decided to use the alternative of the posterior Bayes factor (PBF), defined by Aitkin (1991), which has the equivalent definition of the Bayes factor but replacing the prior $P(\theta|M)$ in Eq. A.5 by the posterior $P(\theta|M, D)$. As we run the MCMC Hammer to calculate the posterior distribution of the model parameters, the PBFs are just the ratios between the means of the likelihoods evaluated at the points sampled with the MCMC for each profile (Fig. 2.7). The PBF will be the most reliable discriminant when deciding how good the different profiles fit the data, as it does not require any assumptions, spatial binning or unique possible values for the structural parameters.

Aitkin (1991) associated the values of the PBF greater than 20, 100 or 1000 with strong, very strong and overwhelming sample evidence against the less probable model. However, we prefer to use the later widely cited logarithmic scale defined by Kass & Raftery (1995) (Table A.2) to list the PBFs and classical likelihood ratios in Table 2.3.

This logarithmic scale allows us to infer the PBFs between pairs of profiles that were not matched in Table 2.3, by adding the values corresponding to the pairs that are in between. For example, while the King profile has $2\ln(\mathrm{PBF}) = 1.6$ against the exponential one, it has $1.6 + 0.8 = 2.4$ against the Sérsic profile and $1.6+0.8+1.8 = 4.2$ against the Plummer one. Thus, whereas the evidence is not worth more than a bare mention respect to the exponential profile, there is a positive evidence against the Sérsic and Plummer profiles. Likewise there is a positive evidence in favour of the exponential profile against the Plummer one. Thereby one can check that the order following the goodness-of-fit of the different profiles according to the PBFs is different than that given by the $\chi^2_{red}$ (or even by the likelihood ratio, see e.g. Table A.3 in Sect. A.4). Regarding the rest of the matches between the profiles fitted by us their evidence is not worth more than a bare mention, while all the PBFs for the profiles of IH95 and R16 give a very strong (overwhelming in the scale of Aitkin 1991) evidence in favour of any of the profiles fitted in this work, with both the $\chi^2_{red}$ and classical likelihood ratio strongly disfavouring their structural parameters too.

## A.4 Structural parameters from S/N=5 catalogue

Here we show the results of applying the analysis from Sect. 2.3 over the photometric catalogue cut at S/N=5 of the shallowest pointing, that is $(g, r) = (24.9, 24.9)$, with $\sim$ 440,000 objects instead of the $\sim$ previous 75,000 but affected by spatially variable star/galaxy classification and completeness. Since the parameters giving the direction of the spatial gradient in the density of contaminants turned out to be sensitive to the differences in depth between pointings and possibly the presence of the artificial over-densities in the out-of-focus regions, we adopted the parameters $a$ and $b$ from our baseline bright catalogue.

Table A.3 shows the obtained structural parameters, Fig. A.3 the Bayesian posterior distributions of the structural parameters from the King profile and Fig. A.4 the best-fitting King model and the observed surface number density profile as a function of major axis radius.

The most striking difference between the structural parameters here derived and those in Table 2.3 is found in the King tidal radius and ellipticity, respectively 120 arcmin and 0.27 before and 62 arcmin and $\sim$ 0.13 in this analysis. This change in the tidal radius would sweep away one of the most remarkable features of this dSph. For comparison, using the heliocentric distance from McConnachie (2012), the corresponding physical tidal radius for dSphs similar in luminosity are $\sim$ 1.9 kpc (Sculptor), $\sim$ 0.6 kpc (Draco), $\sim$ 1.1 kpc (Ursa Minor) and $\sim$ 0.6 kpc (Leo II), while for Sextans it would change from $\sim$ 4.0 kpc (IH95) to $\sim$ 1.6 kpc. On the other hand, this deeper catalogue also yields an overall more compact galaxy, whose half-light radius changes from $\sim$ 22 arcmin in Table 2.3 to $\sim$ 18 arcmin here. Regarding the goodness of the fits, according to the PBF the King profile is still the model which better reproduces our dataset, with a very strong evidence in the scale of Kass & Raftery (1995) (overwhelming in the one of Aitkin 1991) against any of the other profiles.

We have not presented or used these results in the main body of Chapter 2 since the corresponding two-dimensional map of residuals shows differences in depth between some pointings; that is spatially coherent features. However, these differences are rather small ($\lesssim$ 1 stars/arcmin$^2$) compared to the stellar densities at this depth (see Fig. A.4, even when being contamination subtracted) and only appear between some pointings which besides, do not include the central ones, which encompass almost the whole stellar body of Sextans, and we could not pinpoint how the observed differences in depth could result into these specific changes in the obtained structural parameters.

In addition, as one can check in Fig. A.3, due to the larger statistics the distributions are more Gaussian than the ones from Fig. 2.7. Likewise, the higher number of analysed stars for Table A.3 yields considerably smaller error bars

| Parameter | Exponential | Sérsic | Plummer | King | IH95 | R16 |
|---|---|---|---|---|---|---|
| $\alpha_{2000}$ (º) | $153.256^{+0.002}_{-0.003}$ | $153.255^{+0.003}_{-0.003}$ | $153.256^{+0.003}_{-0.003}$ | $153.256^{+0.003}_{-0.003}$ | $153.2625^{+0.0005}_{-0.0005}$ | $153.277^{+0.003}_{-0.003}$ |
| $\delta_{2000}$ (º) | $-1.623^{+0.002}_{-0.003}$ | $-1.623^{+0.002}_{-0.002}$ | $-1.623^{+0.003}_{-0.002}$ | $-1.623^{+0.003}_{-0.002}$ | $-1.6147^{+0.0003}_{-0.0003}$ | $-1.617^{+0.008}_{-0.008}$ |
| Ellipticity | $0.11^{+0.02}_{-0.02}$ | $0.13^{+0.02}_{-0.02}$ | $0.13^{+0.02}_{-0.02}$ | $0.15^{+0.02}_{-0.02}$ | $0.35^{+0.05}_{-0.05}$ | $0.29^{+0.03}_{-0.03}$ |
| Position angle (º) | $50^{+3}_{-3}$ | $53^{+3}_{-3}$ | $50^{+3}_{-3}$ | $53^{+3}_{-3}$ | $56^{+5}_{-5}$ | $58^{+6}_{-6}$ |
| Sérsic index n | - | $0.71^{+0.02}_{-0.02}$ | - | - | - | - |
| Sérsic factor b(n) | - | $0.9^{+0.5}_{-0.4}$ | - | - | - | - |
| Exponential $r_e$ (′) | $10.6^{+0.2}_{-0.2}$ | - | - | - | $15.5^{+0.1}_{-0.1}$ | - |
| Plummer $r_p$ (′) | - | - | $19.3^{+0.3}_{-0.3}$ | - | - | $35.7^{+0.7}_{-0.7}$ |
| Sérsic $r_s$ | - | $15^{+5}_{-5}$ | - | - | - | - |
| King $r_c$ (′) | - | - | - | $16.7^{+0.5}_{-0.5}$ | $17^{+2}_{-2}$ | $27^{+2}_{-2}$ |
| King $r_t$ (′) | - | - | - | $62^{+2}_{-2}$ | $160^{+50}_{-50}$ | $83^{+8}_{-8}$ |
| 2D half-light $r_h$ (′) | $17.8^{+0.2}_{-0.2}$ | $15^{+5}_{-5}$ | $19.3^{+0.3}_{-0.3}$ | $17^{+1}_{-1}$ | $26^{+0.2}_{-0.2}$ (Exp.) | $35.7^{+0.7}_{-0.7}$ (Plummer) |
| | | | | | $28^{+5}_{-5}$ (King) | $24^{+2}_{-2}$ (King) |
| $\chi^2_{red}$ | 1.67 | 1.37 | 1.53 | 1.31 | 3.95 $\left(\frac{\text{Exp. IH95}}{\text{Exp.}}\right)$ | 15.55 $\left(\frac{\text{Plummer R16}}{\text{Exp.}}\right)$ |
| | | | | | 4.59 $\left(\frac{\text{King IH95}}{\text{Exp.}}\right)$ | 7.48 $\left(\frac{\text{King R16}}{\text{Exp.}}\right)$ |
| $2\ln\left(\frac{\text{likelihood}_1}{\text{likelihood}_2}\right)$ | - | 102.2 $\left(\frac{\text{Sérsic}}{\text{King}}\right)$ | 10.5 $\left(\frac{\text{Plummer}}{\text{Exp.}}\right)$ | 94.2 $\left(\frac{\text{King}}{\text{Plummer}}\right)$ | -1225.1 $\left(\frac{\text{Exp. IH95}}{\text{Exp.}}\right)$ | -3452.1 $\left(\frac{\text{Plummer R16}}{\text{Exp.}}\right)$ |
| | | | | | -1355.7 $\left(\frac{\text{King IH95}}{\text{Exp.}}\right)$ | -1468.8 $\left(\frac{\text{King R16}}{\text{Exp.}}\right)$ |
| $2\ln$ (PBF) | - | 195.4 $\left(\frac{\text{Sérsic}}{\text{Plummer}}\right)$ | 10.2 $\left(\frac{\text{Plummer}}{\text{Exp.}}\right)$ | 22.7 $\left(\frac{\text{King}}{\text{Sérsic}}\right)$ | -1220.4 $\left(\frac{\text{Exp. IH95}}{\text{Exp.}}\right)$ | -3447.4 $\left(\frac{\text{Plummer R16}}{\text{Exp.}}\right)$ |
| | | | | | -1352.6 $\left(\frac{\text{King IH95}}{\text{Exp.}}\right)$ | -1466.0 $\left(\frac{\text{King R16}}{\text{Exp.}}\right)$ |

Table A.3: Sextans structural parameters (median values of the marginalized posterior distributions) derived with the MCMC Hammer applied to the photometric catalogue cut at S/N=5 from the shallowest DECam pointing, plus $\chi^2_{red}$, classical likelihood ratios and posterior Bayes factors of the different surface density profiles. Classical likelihood ratios and PFBs are colour-coded as in Table 2.3.

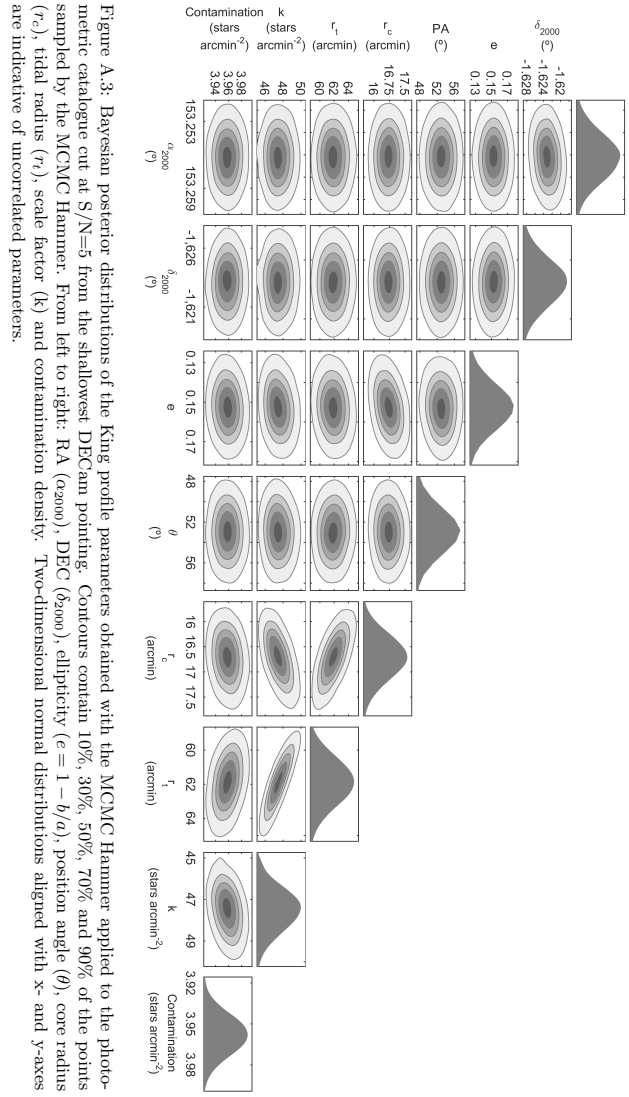


Figure A.3: Bayesian posterior distributions of the King profile parameters obtained with the MCMC Hammer applied to the photometric catalogue cut at S/N=5 from the shallowest DECam pointing. Contours contain 10%, 30%, 50%, 70% and 90% of the points sampled by the MCMC Hammer. From left to right: RA ($\alpha_{2000}$), DEC ($\delta_{2000}$), ellipticity ($e = 1 - b/a$), position angle ($\theta$), core radius ($r_c$), tidal radius ($r_t$), scale factor (k) and contamination density. Two-dimensional normal distributions aligned with x- and y-axes are indicative of uncorrelated parameters.

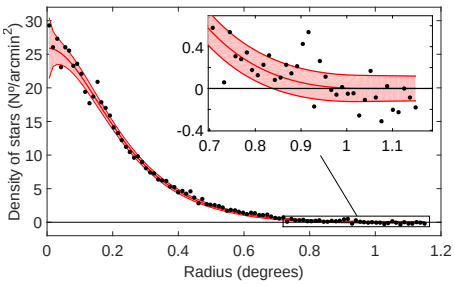


Figure A.4: Contamination subtracted surface number density profile of Sextans stars as a function of the major axis radius from the photometric catalogue cut at S/N=5 from the shallowest DECam pointing, overlaid onto the $1\sigma$ confidence interval (red band) of the best-fitting King profile fitted with the MCMC Hammer. The $1\sigma$ confidence interval is computed from the best-fitting model assuming Poisson variances in each elliptical annulus. We do not use logarithmic scale to be able to show the density fluctuations below the estimated background (negative values); otherwise plots mimic the presence of extra-tidal stars.

than those from Table 2.3, as expected from the tests with mock galaxies in Sect. A.2; at the same time that the values of those structural parameters common to the different fitted profiles still remain acceptably compatible between them. Further, Fig. A.4 shows a good agreement between the best-fitting King model and the observed density profile at this depth.

Finally, the large change in the tidal radius agrees quite well with the limits of the decontaminated surface density map (first panel of Fig. 2.9) too, which could be a consistency check since the tidal radius and the map are inferred by two completely independent methods. Another consistency check is given by the right panel of Fig. 2.13, which shows that the decontaminated CDF of the whole population of Sextans reaches 1 at a major axis radius of 62 arcmin, not increasing for larger distances, exactly agreeing with the nominal tidal radius derived from the deep catalogue. As before, this CDF was derived through another method completely independent from the previous two. Further, this tidal radius would also agree with the extension of the spectroscopic samples (left panel of Fig. 2.14), not detecting any star with high probability of membership beyond it. It would even coincide with the maximum radius reached by $p(a)$ estimated via monotonic regression in W09 ($\sim$ 65 arcmin), even though the W09 spectroscopic set does not extend much beyond that point.

We decided to also show these results because we could not ensure that the observed differences in depth in the affected pointings were the cause of changing the values of some of the structural parameters to such an extent, at the same time that many indicators in favour of these new values made us consider the possibility of them being real. We defer to Chapter 3 an in-depth analysis of this dependence of the structural parameters on the adopted magnitude cut.

# B

# Appendix of Chapter 3

## B.1 Decontamination of 2D maps

The method we developed to decontaminate the 2D spatial distribution of individual sources in the red and blue red giant branch selection boxes without spatially binning the data, was inspired by the one developed in Sect. 2.5 to decontaminate the radial cumulative distribution functions (CDFs) of the different Sextans' evolutionary phases.

We first calculate the ratio between the number of stars falling in the CMD selection box of interest but located well away from the galaxy centre, for example outside the King tidal radius, therefore at a spatial location expected to be occupied only by contaminants, and the number of objects in this same spatial region but in a part of CMD known not to contain stars from the target galaxy; in this case we used the colour cut $g - r > 1$, as in Sect. 2.5. This ratio reflects the expected proportion of contaminants in the CMD selection box of interest with respect to the red ones ($g - r > 1$).

The algorithm next randomly resamples all the red contaminants according to this ratio and decontaminates the two-dimensional spatial distribution as we did with the one-dimensional radial CDFs in Sect. 2.5, that is by removing those stars spatially closest to the resampled contaminants. We implemented two other features in this decontamination method. On one hand, in order to prevent removing some stars with too large separation from their closest red contaminant, we compute the probability distribution function of the separations between the stars from the sample and their closest resampled red contaminants and limit the maximum allowed separation to be the percentile 99% of this probability distribution. On the other hand, inspired by the pro-

cedure developed in Piatti (2018) to calculate stellar membership probabilities in a globular cluster, instead of making a unique decontamination from just one resample of the red contaminants, our algorithm generates numerous decontaminated maps (i.e. 1000) from many different random resamplings of the red contaminants. Then, the probability that a star belongs to the galaxy is the ratio between the number of times that it is not removed and the number of decontaminations performed. We found that the contaminants start being negligible when plotting the spatial locations of those stars with a membership probability larger than $\sim$ 60-70%.

# List of Figures

# List of Tables